University of Alberta

Petrogenesis of the Cretaceous Cassiar Batholith, Yukon-B.C., Canada: Implications for Magmatism in the North American Cordilleran Interior

by

Leslie Ann Driver

A thesis submitted to the Faculty of Graduates Studies and Research
in partial fulfillment of the requirements for the degree of Master of Science

Department of Earth and Atmospheric Sciences

Edmonton, Alberta

Fall 1998

View northward of the Cassiar batholith and surrounding area,
from northcentral British Columbia, Canada

If we want to be pedantic,
all granitoids are 'M'-types;
some just have longer
evolutionary paths than others!

--D.B. Clarke
in Granitoid Rocks, 1992, p.185.

Abstract

The ~100 Ma Cassiar batholith (CB) was emplaced into the Omineca Crystalline Belt along the western edge of cratonic North America (cNA). Dominant rock types in this calc-alkaline batholith are biotite ± muscovite ± hornblende granite and granodiorite. The CB has a wide range of strontium, neodymium and oxygen isotope compositions (Sr_i= 0.706 to 0.734; ε_{Nd}= -3.5 to -17.9; (T_{DM})= 2000 to 980 Ma; $\delta^{18}O$= +7.6‰ to +11.6‰), but a limited range of lead isotope compositions ($^{206}Pb/^{204}Pb$= 19.14 to 19.24; $^{207}Pb/^{204}Pb$= 15.70 to 15.72; $^{208}Pb/^{204}Pb$= 39.14 to 39.26). These data suggest that the CB was derived by partial melting of two crustal sources: (1) ancient cNA basement rocks or sediments, and (2) basement rocks with mantle-like Sm/Nd and Rb/Sr (e.g., amphibolite). We interpret the CB to have formed from melting in response to crustal thickening that occurred during accretion of allochthonous terranes in Jurassic through Cretaceous time.

Dedication

The difference between perserverance and obstinancy is, that one comes from a strong will, and the other from a strong won't.
--Henry Ward Beecher

To *Jill*, *Jon Paul*, and *Jessica*:
because of all you can

&

especially to *Noma*:
because of all you did

Acknowledgements

I wish to acknowledge my advisor, Tom Chacko, for all of his encouragement, guidance, patience, wisdom, inspiriation, and for his complete support of this project, both mentally and financially. I wish also to thank him for all that "work" time spent yabbering. I am also indebted my co-advisor, Rob Creaser, for financial support, field work assistance, guidance through the world of granite studies, and especially for training me in the art of isotope geochemistry. Philippe Erdmer is acknowledged for introducing me to and guiding me through the geology of the Canadian Cordillera. His assistance with my field work and continued interest in this project were invaluable. I am grateful for the questions and comments of Tom Forest, who helped me improve this work by making me see it from a different angle. I wish to thank George Morris for his field work assistance, and for the use of his vast personal library of important granite and Cordilleran literature. In addition, our discussions about this science have been invaluable, and his support and encouragement were instrumental in the completion of this project. Hugh Gabrielse was instrumental in getting this project off the ground. I am especially appreciative of the three days we spent in the depths of the GSC-Vancouver rock storage facility, where he gave me Cassiar batholith samples, and more information than I could have ever hoped to remember. I am also indebted to Peter Larson, for sparking my interest in geology, starting me down the path of Cordilleran granite research, and encouraging me to follow it up.

I would like to thank Karlis Muehlenbachs for the use of his stable isotope lab, and Bjarni Gautason and for running my silicate samples. Olga Levner provided valuable lab assistance throughout my radiogenic isotope work, and Stacey Hagen ran

some of my samples without even knowing it. Don Resultay is acknowledged for the many thin sections and polished billets he made for me.

I would also like to thank my fellow graduate students Suman Kumar De, Matt Perks, and Rajeev Kumar Nair for many stimulating talks about magmatism, geology, world politics, and life in general (from the mother hen of the group). I am grateful Karen Fallas for her friendship and her willingness to discuss the Canadian Cordillera whenever I wanted to. Kim Jardine, Asuka Tsuru, Betsy Willson, Cathy Skilliter, Andrea Noyes, Dave Selby, Pedro Jugo, Astrid Arts, Darlene Atkinson, Devon Rowe, Mark Skidmore, Julie Esdale, Ted Little, and Elaine Cheyney are great friends and drinking buddies.

Diane Johnson and Charles Knaack from WSU GeoAnalytical Laboratory are acknowledged for my XRF and ICP-MS data. Stephen Soubliere of TransNorth Helicopters is mostly responsible for the massive amount of samples I had to analyse.

Funding for this project was provided by the Canadian Circumpolar Institute at the University of Alberta, an NSERC Lithoprobe Research Grant awarded to Tom Chacko, and the J. Gordin Kaplan Graduate Student Travel Award at the University of Alberta.

Finally I would like to thank my mother, Noma Campbell, for her lifelong support of me and my wishes, my sister, Jill Driver for always being there, no matter what, my father, Gary Driver, for believing in me, and George Morris for being here, and for being there. And a big, lazy meow to my own Cassiar.

Table of Contents

List of Tables

List of Figures

Abbreviations

AFC	assimilation and fractional crystallization
AfGr	alkali-feldspar granite
AFM	alkalis (Na_2O+K_2O), Fe, and Mg
AfQs	alkali-feldspar quartz syenite
Amph	amphibolite
ANOR Parameter	[An/(An+Or)]*100
ASI	alumina-saturation index
BB	Bugaboo batholith
bt	biotite
CA	Cassiar Terrane
CB	Cassiar Batholith
CC	Cache Creek Terrane
CIPW	Cross, Iddings, Pirsson, and Washington
CIZ	Cratonic Intrusion Zone
cNA	cratonic North America
CPC	Coast Plutonic Complex
CRB	Coast Ranges batholith
CVZ	Central Volcanic Zone, Andes
D	diorite
DM	depleted Mantle
DY	Dorsey Terrane
FCB	Fry Creek batholith
G	gabbro
Ga	giga anos (billion years)
Gd	granodiorite
Gr	granite
Grt	granitoid
hbl	hornblende
HCR	Horsethief Creek batholith
Hfl	hornfels
HFS	High field strength

HREE	heavy rare earth elements
IB	Idaho batholith
ICP-MS	inductively coupled plasma mass spectrometry
KO	Kootenay Terrane
LIL	Large ion lithophile
IUGS	International Union of Geological Sciences
LREE	light rare earth elements
Ma	mega anos (million years)
Mg	monzogranite
MORB	mid-ocean ridge basalt
ms	muscovite
NBS	National Bureau of Standards
ORG	ocean ridge granites
ppm	parts per million
PRB	Peninsular Ranges batholith
Q parameter	[Q/(Q+Ab+Or+An)]*100
Qd	quartz diorite
QFG	quartzo-feldspathic gneiss
Qg	quartz gabbro
Qm	quartz monzonite
Qmd	quartz monzodiorite
QN	Quesnellia
Qs	quartz syenite
qtz	quartz
REE	rare earth elements
Sch	schist
SEBCB	southeastern British Columbia batholiths
SM	Slide Mountain Terrane
SNB	Sierra Nevada batholith
SP	Spirit Pluton
ST	Stikinia Terrane
syn-COLG	syn-collisional granite
THB	Transhimalayan Batholith
Ton	tonalite

VAG	Volcanic arc granite
WCB	White Creek batholith
WPG	within plate granite
wr	whole rock
WSD	Wallowa-Seven Devils Terrane
wt. %	weight percent
XRD	X-ray diffraction
XRF	X-ray fluorescence

INTRODUCTION

The North American Cordillera experienced widespread magmatism during Mesozoic time extending from Alaska to northern Mexico, and from the western coast of North America to 800 km inland. This magmatism can be divided into two chronological and spatial groups, a coastal group and an inland group. The coastal magmatism is represented by the Coast Plutonic Complex in Alaska, Yukon, and British Columbia, the Sierra Nevada batholith in California, and the Peninsular Ranges batholith in southern California and Mexico (Figure 1). These granitoids have low K contents (dominantly tonalite and granodiorite compositions), and contain a significant mantle component, as shown by their primitive mantle isotope signatures (Brandon and Lambert, 1994). In general, magmatism in these batholiths began in the Middle to Late Jurassic (180 to 140 Ma). These magmas, along with the Peruvian Coastal batholith, are considered to be typical Andean-type subduction magmas located at continental margins (cf. Pitcher, 1982; Pitcher *et al.*, 1985; Gromet & Silver, 1987).

In contrast, the more easterly magmatism of batholiths such as the Idaho batholith, the Bugaboo, White Creek, and Horsethief Creek batholiths of British Columbia, and smaller batholiths in British Columbia, Washington, Utah, eastern Nevada, southeastern California, Arizona, New Mexico, Montana, and Colorado (Miller and Barton, 1990) occur well inland from the western edge of cratonic North America. These plutons are distinct in composition and possibly origin from coastal magmatism. For the purpose of this paper, this easterly region overlying cratonic North America will be called the Cratonic Intrusion Zone (CIZ). The CIZ is bounded to the west by the Sr_i 0.704/0.706 line (Kistler and Peterman, 1973; 1978; Armstrong *et al.*, 1977). This line has been interpreted to represent the boundary between cratonic north America and accreted crust (Figure 1) (Monger and Price, 1979; Monger *et al.*, 1982; Fleck and Criss, 1985). The magmas are mid-Cretaceous to Eocene in age, generally younger than

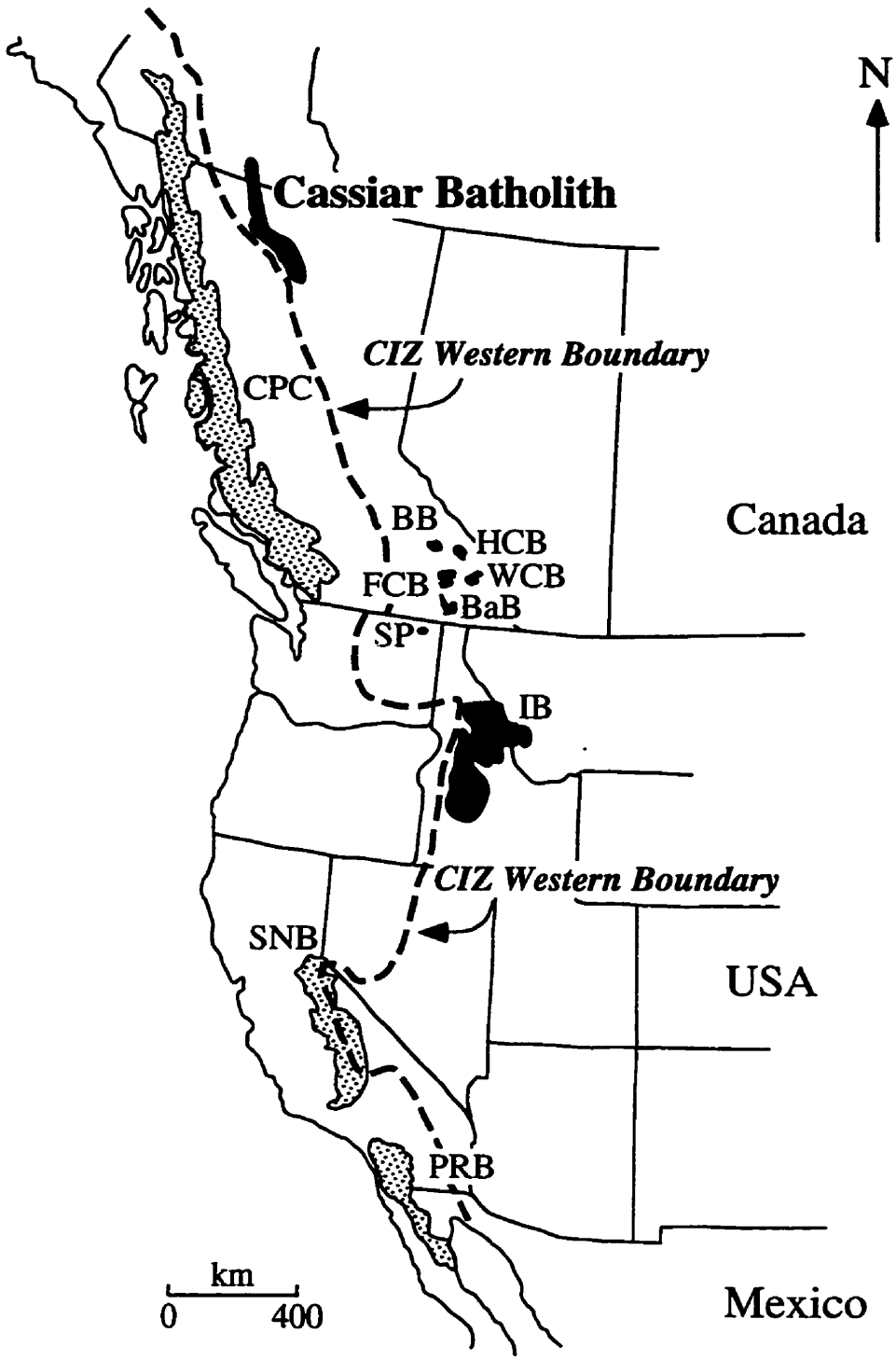

Figure 1. Major Mesozoic batholiths of the North American Cordillera, and western boundary of the cratonic intrusion zone (CIZ). CPC= Coast Plutonic Complex, BB= Bugaboo batholith, HC= Horsethief Creek batholith, WC= White Creek batholith, FC= Fry Creek batholith, BaB= Bayonne batholith, SP= Spirit pluton, IB= Idaho batholith, SNB= Sierra Nevada batholith, PRB= Peninsular Ranges batholith.

their coastal counterparts. Magma compositions become notably more felsic and peraluminous with time (Miller and Barton, 1990). The dominant rock types are biotite or muscovite-biotite granite and granodiorite.

The origin of the inland magmas is equivocal. Miller and Barton (1990) state that:

> "Although CI [Cordilleran Interior] magmatism extended remarkably far inland and evidence for a major subcrustal component is in many cases absent, it almost certainly was directly related to a subduction-induced thermal regime."

Hyndman and Foster (1988) also attribute the generation of one of the major CIZ intrusions, the Idaho batholith, to a subduction setting. Other workers minimize the role of subduction in the generation of these magmas and invoke a process involving melting of crustal rocks (e.g. Brandon and Lambert, 1993; 1994; Brandon and Smith 1994; Patiño Douce *et al.*, 1990). Crustal melting may have been triggered by intrusion of mafic magmas into the crust (Lipman *et al.*, 1972; Keith, 1978; Hyndman and Foster, 1988), influx of water-rich fluids (Hamilton, 1988), or tectonic burial of high heat producing metasedimentary rocks (Patiño Douce *et al.*, 1990). Brandon and Lambert (1993; 1994) and Brandon and Smith (1994) suggested that four batholiths in southeastern British Columbia were generated by anatexis of overthickened crust that formed during Mesozoic accretion of microcontinents along the western North American plate margin.

The Cassiar Batholith is part of the CIZ suite, and is the largest plutonic body in the hinterland of the Canadian Cordillera. The batholith is mid-Cretaceous in age (~109 Ma) (Armstrong, 1988; Woodsworth *et al.*, 1991), and extends continuously for 350 km along strike from northern British Columbia into southern Yukon with east-west dimensions of 5-40 km (Figure 2) (Gabrielse, 1962a; 1962b; 1963; 1969). Lithologically similar granitoids outcrop sporadically along strike for another 300 km into northern Yukon. In addition to the large areal extent, the Cassiar Batholith also

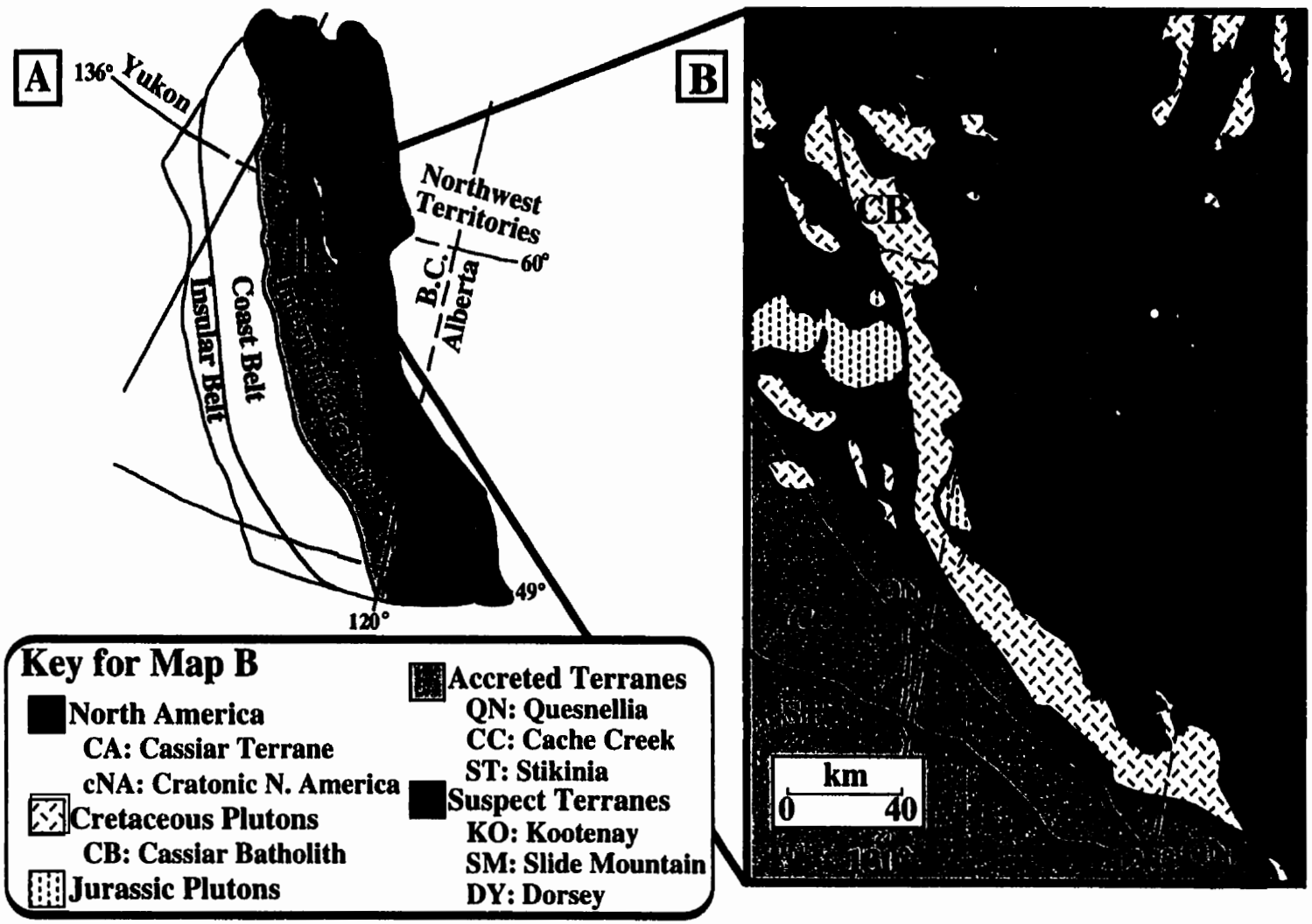

Figure 2. (A) Physiographic-geologic belts of the Canadian Cordillera and (B) Terrane map of the northern Canadian Cordillera. Both maps after Wheeler and McFeely, 1991.

occupies a key position in the overall tectonic framework of the North American Cordillera. It is located within the Omineca Crystalline Belt, with rocks to the east representing cratonic North America, and rocks to the west believed to be accreted terranes of the Cordilleran margin (Monger and Price, 1979; Monger *et al.*, 1982). The presence of such an enormous volume of magmatic rock near this major geologic boundary, as well as its dimensions and orientation, strongly suggests that the generation and emplacement of the batholith played a fundamental role in the evolution of this part of the North American Cordillera.

Despite its importance, only limited work has been carried out on the Cassiar Batholith. This thesis reports new rock and field descriptions, as well as major-, trace-element and isotopic (O, Sr, Nd, and Pb) data for the Cassiar Batholith. These data provide important constraints on the origin of compositional variations within the batholith and on possible source materials for the Cassiar magmas. The data are also used to gain insight on the tectonic setting in which the Cassiar magmas were generated. In particular, I evaluate subduction-related versus collision-related tectonic settings for the generation of the Cassiar and other CIZ magmas.

GEOLOGY

Geologic Setting

The Omineca Crystalline Belt is mainly composed of uplifted igneous and metamorphic rocks. It straddles the boundary between cratonic North America to the east (the Foreland Fold and Thrust Belt), and allochthonous terranes to the west (the Intermontane Belt) (Monger and Price, 1979; Monger *et al.*, 1982). The Omineca Crystalline Belt rocks have a distinct North America affinity, with the exception of klippen of accreted oceanic and island arc assemblages that locally overlie the belt. The rocks of the Omineca Crystalline Belt consist mainly of miogeoclinal and clastic wedge

(meta)sedimentary assemblages. In some cases, these are easily correlated to rocks in the Foreland Fold and Thrust Belt, whereas in other places extensive deformation and metamorphism preclude definitive correlation.

During Mesozoic time, the Omineca Crystalline Belt experienced folding and faulting associated with eastward thrusting, driven by the accretion of the allochthonous terranes to the west (Monger and Price, 1979; Monger *et al.*, 1982). In addition, at this time (and into the Eocene), a series of dextral strike-slip faults (including the Tintina-Northern Rocky Mountain Trench fault) disrupted the Omineca Crystalline Belt (Monger and Price, 1979; Monger *et al.*, 1982). Further south, the Omineca Crystalline Belt experienced widespread extension during Tertiary time, but none has been recognized near the Cassiar Batholith (Coney, 1989). The Omineca Crystalline Belt also contains many suites of plutonic rocks, emplaced throughout time. Distinct among these are the widespread, mid-Cretaceous, felsic granitoids recognized throughout the Omineca Crystalline Belt.

The Cassiar Batholith, which is part of this mid-Cretaceous plutonism, intruded rocks of the Cassiar Terrane. The Cassiar Terrane contains miogeoclinal strata, including platform carbonates and clastic wedges, and is considered part of the continental margin of ancient North America (Coney, 1989). It was translated northward along the then dextral Tintina fault in the Late Cretaceous and Early Tertiary. The translation distance of the Cassiar Terrane is yet undetermined, although estimates of 400-500 km are commonly accepted (Gabrielse And Yorath, 1991).

Previous work on the Cassiar Batholith includes regional geological maps of the Cassiar Batholith area prepared by the Geological Survey of Canada (Gabrielse, 1962a; 1962b; 1963; 1969; Poole *et al.*, 1960; summarized by Gabrielse and Reesor, 1974), a number of K-Ar determinations yielding a mid-Cretaceous (89-109 Ma) ages (Baadsgaard *et al.*, 1961; Wanless *et al.*, 1978; Panteleyev, 1985), and a petrologic

study of regional metamorphic rocks from the vicinity of the batholith (Mansy, 1986). The remaining work has concentrated on the economic mineralization associated with and peripheral to the batholith itself (e.g., Mato *et al.*, 1983).

Field Work and Sample Acquisition

Field observations and systematic sampling of the Cassiar Batholith was conducted in July 1996, during which 76 samples were acquired from 36 different locations. Sampling was carried out by helicopter in order to a collect representative suite of samples from across the entire length of the batholith. More detailed east-west traverses were conducted along the Alaska and Cassiar Highways. Samples collected include batholithic granitoids, as well as cross-cutting dykes, xenoliths, and marginal contacts. Four country rock samples were also collected along three traverses in contact with the Cassiar Batholith. An additional fifteen samples of Cassiar Batholith granitoids were obtained from Dr. H. Gabrielse of the GSC-Vancouver in April, 1996. Sample numbers and locations are given in Appendices A and B.

Field and Petrographic Descriptions

The Cassiar Batholith shows a general compositional variation from north to south, and a textural variation from east to west. It is not known whether the contacts between different rock units within the batholith are sharp or gradational as no contacts were observed directly during the course of the field work. According to the CIPW normative equivalent to the IUGS classification diagram (Streckeisen and LeMaitre, 1979), the Cassiar Batholith consists of granite, granodiorite, quartz monzodiorite, quartz monzonite, and quartz syenite in decreasing abundance (Figure 3). This normative classification of the rock types is consistent with estimated modal compositions. In general, the southern part of the batholith contains a higher proportion of biotite and

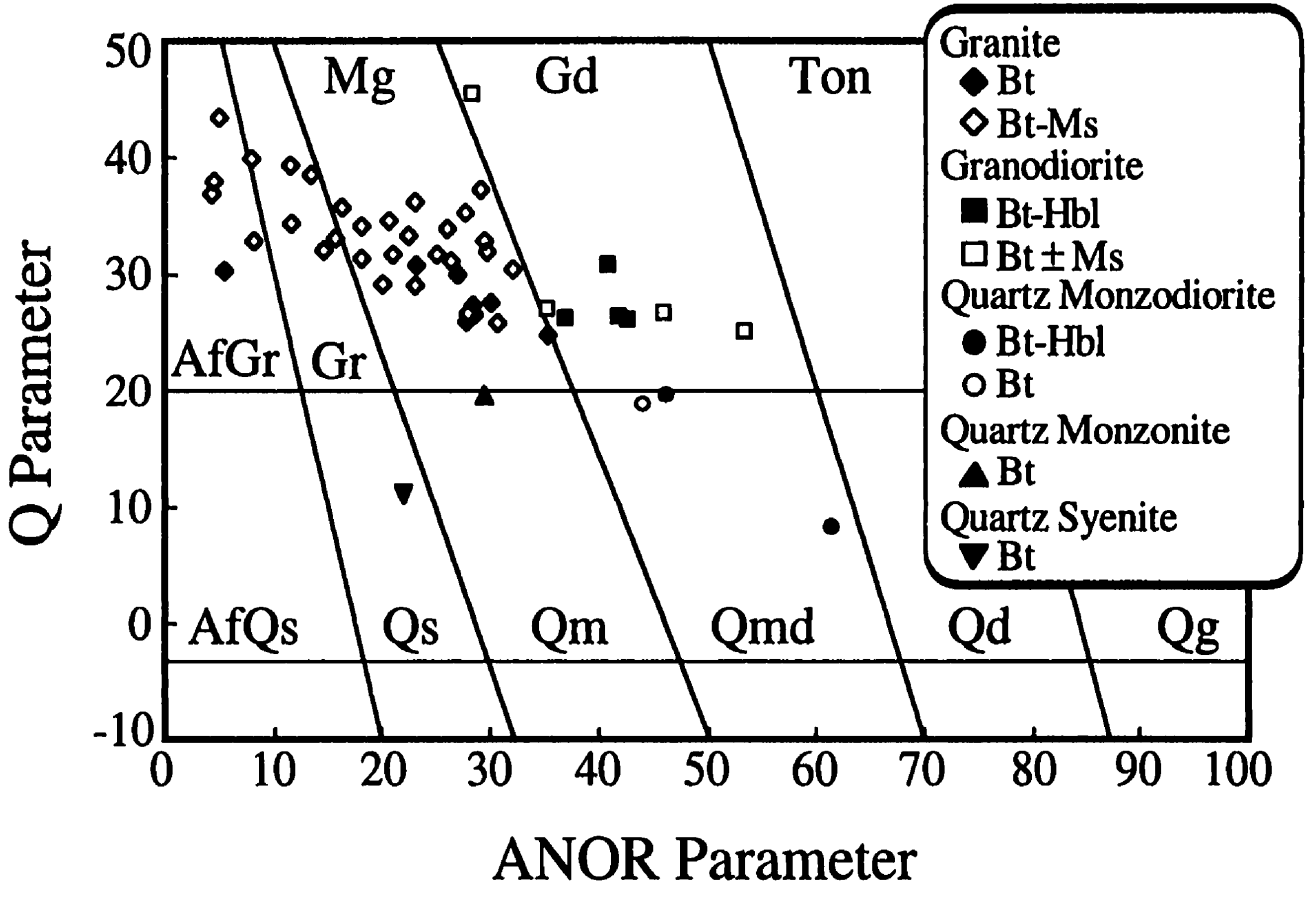

Figure 3. IUGS granitoid classification diagram (Streckeisen & LeMaitre, 1979) showing plotted CIPW norms calculated for the Cassiar Batholith from XRF oxide values. ANOR Parameter= [An/(An+Or)]*100, Q parameter= [Q/(Q+Ab+Or+An)]*100, AfGr= alkali-feldspar granite, Gr= granite, Mg= monzogranite, Gd= granodiorite, Ton= tonalite, AfQs= alkali-feldspar quartz syenite, Qs= quartz syenite, Qm= quartz monzonite, Qmd= quartz monzodiorite, Qd= quartz diorite, Qg= quartz gabbro, Bt=biotite, Ms=muscovite, Hbl=hornblende.

hornblende-biotite granodiorite and quartz monzodiorite whereas the northern part comprises mainly muscovite-biotite granite (Figure 4). It should be noted, however, that all three rock types are present throughout the batholith.

Most Cassiar Batholith samples are massive, medium-grained, and leucocratic (color index of 3 to 10%), although some samples contain K-feldspar phenocrysts up to 5 cm in length. Feldspars, are weakly to moderately altered, the plagioclase is normally zoned, and K-feldspar has tartan twinning. Some samples contain smaller, equant grains of highly altered feldspars, incorporated into some of the larger feldspar grains.

Biotite is the major varietal mineral (up to 15%) and shows minor alteration to chlorite. Primary muscovite is found in many samples, and constitutes 1-5% of the modal mineralogy. In a few samples, muscovite (<1%) is secondary. Hornblende (<2%) is present as a varietal mineral in 8 of the samples (<5% in LAD96-2A). Accessory minerals include apatite, zircon, sphene, and epidote. Allanite is present in five samples.

Distinct among the Cassiar Batholith granitoids are samples located along the western boundary of the batholith near a major strike-slip fault system. Rocks along this boundary are much finer-grained and display varying degrees of foliation and shearing. The mineralogy is comparable to the more easterly granitoids. Thin sections show that the samples are fine-grained, and contain altered feldspars, and a few (1%) large plagioclase grains that contain normal zoning. Biotite defines a foliation when present in a rock, and quartz has been recrystallized and deformed in some locations. Muscovite is present in minor (<1%) amounts. Apatite is the major accessory mineral, although small zircons are also present.

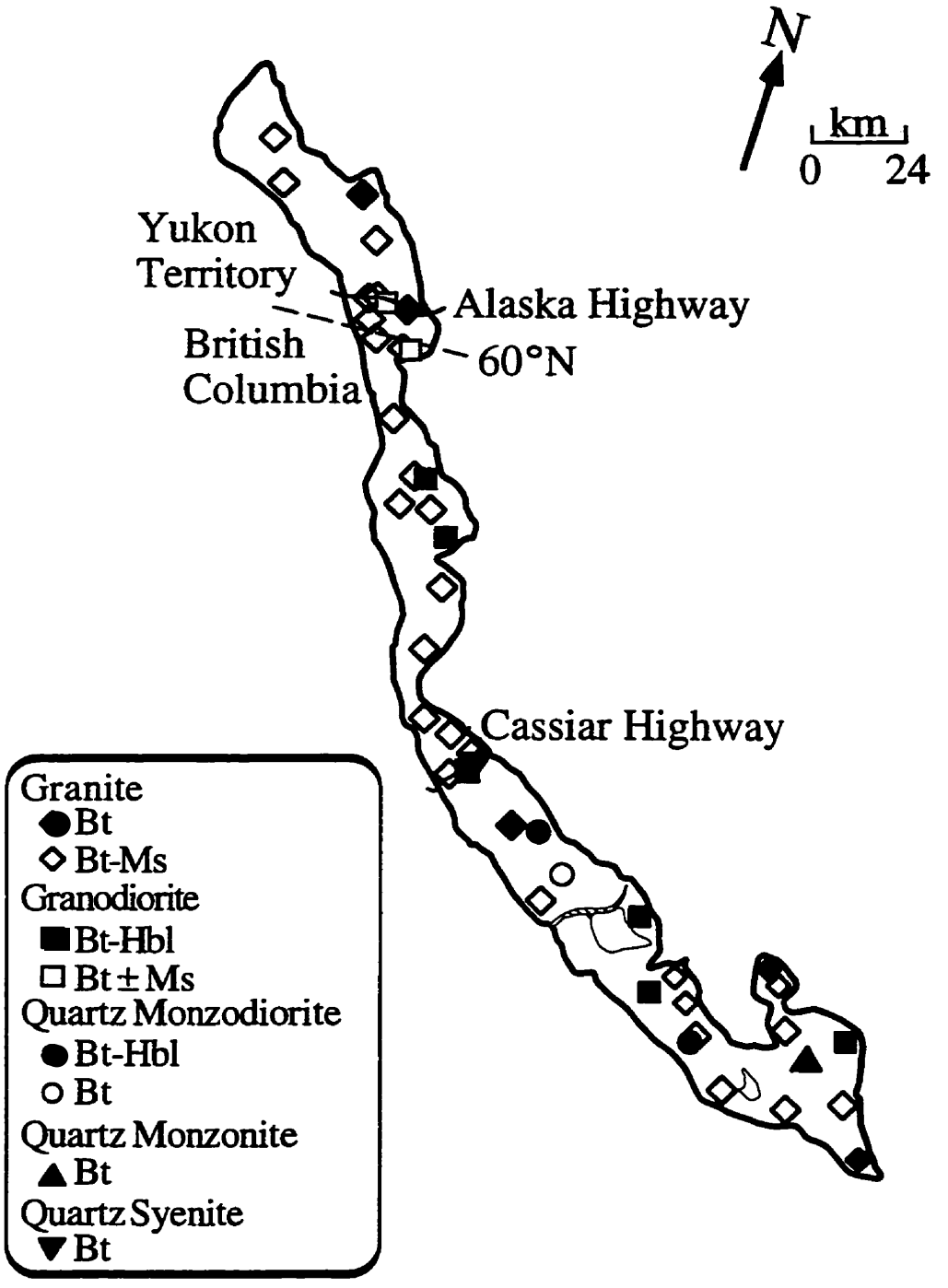

Figure 4. Distribution of rock types within the Cassiar Batholith.

East-West Traverses

East-west traverses within the Cassiar Batholith reveal that the batholith is generally massive, but becomes foliated, sheared, and mylonitized towards the western boundary, a boundary largely composed of strike-slips faults (Cassiar fault, Kutcho fault and other unnamed faults). Along the Alaska Highway, a faint foliation is found at outcrops approximately 18 km from the western boundary. However, a more pronounced foliation is not recognized until 8.2 km from the western boundary. Continuing westward, foliation becomes more pronounced and is accompanied by significant grain size reduction. In the vicinity of the western margin severely dismembered limestone blocks are present in the mylonitized granite. Along the Cassiar Highway outcrop is more scarce, but the same general trends are present.

Dykes

Cross-cutting dykes within the Cassiar Batholith can be divided into three distinct groups. The first group consists of two fine- to medium-grained, mafic dykes that cross-cut much more felsic granitoid host rock. These dykes, located in the middle of the batholith, have visible hornblende and show faint foliations with chilled margins.

The second type of dyke intruding the Cassiar Batholith was observed only along the western boundary on the Cassiar Highway, and constitutes a basaltic dyke swarm. The orientation of these dykes are 256°/74N (middle and northeast) and 244°/68N. A foliation within the granitoid at this location was measured to be 270°/70N. These dykes have chilled margins, and the granite steps through the dyke.

Finally, multiple generations of pegmatitic and aplitic dykes are seen along the Cassiar and Alaska Highway sections. Figure 5 shows typical features seen in outcrop near the western margin of the Cassiar Batholith. In this example, a leucocratic

Figure 5: A typical leucocratic pegmatite dyke cutting strongly foliated granitoid, near the western margin of the Cassiar Batholith. The pegmatite dyke cuts strongly foliated Cassiar Batholith granitoid. The pegmatite dyke has also been deformed. If these and other pegmatites are associated with Cassiar magmatism, then these observations suggest that deformation along the western margin was approximately synchronous with the emplacement of the batholith. These faults are inferred to be strike-slip and to have contributed to the Cassiar Batholith's elongate shape. Outcrop located west of Rancheria on the Alaska Highway (130°50'16").

pegmatite dyke cuts strongly foliated Cassiar Batholith granitoid. The pegmatite dyke has also been deformed. If these and other pegmatites are associated with Cassiar magmatism, then these observations suggest that deformation along the western margin was approximately synchronous with the emplacement of the batholith. These faults are inferred to be strike-slip and to have contributed to the Cassiar Batholith's elongate shape. Further studies to determine the age and association of this and other dykes within the Cassiar Batholith are needed to confirm this observation.

Xenoliths

Xenoliths within the Cassiar Batholith range from mafic to felsic in composition, and are found throughout the intrusion. Mafic xenoliths were found at outcrops LAD96-9, LAD96-34, LAD96-35, and LAD96-36. Location LAD96-9A contain two types of mafic xenoliths; a very-fine-grained and a fine-grained population. Similar looking very-fine-grained xenoliths were collected at LAD96-34B, LAD96-35C, LAD96-35D, LAD96-36C. Slightly coarser-grained mafic xenoliths were also present in an aplitic dyke at LAD96-35F, and at LAD96-36J.

Pelitic xenoliths (phyllite, schist, paragneiss) are abundant in outcrops throughout the batholith as well. Pelitic xenoliths were collected at LAD96-34, LAD96-35, LAD96-36, and LAD96-37.

Contact aureole and roof pendant rocks, some of which may be representative of source rocks of the Cassiar magmas, were collected along three traverses adjacent to the southern Cassiar Batholith. Samples collected include quartzite, and andalusite-bearing schists and hornfels. The latter constrain emplacement pressures in this area to less than 4 kilobars (approximately 13 km) (Holdaway, 1971).

MAJOR- TRACE- AND RARE-EARTH-ELEMENT GEOCHEMISTRY

Analytical Procedures

Fifty samples of the Cassiar Batholith were analyzed for their major-, trace- and rare-earth- element compositions at Washington State University's GeoAnalytical Laboratory (Appendix C). Major elements and selected trace element concentrations were determined by X-ray fluorescence spectrometery (XRF) using procedures outlined by Johnson *et al.* (1998). Inductively coupled plasma mass spectrometery (ICP-MS) was used to determine the concentration of other trace elements including the rare earth elements in 35 of these samples (Appendix D). See Knaack *et al.* (1994) for sample preparation and analytical precision. Information acquired through these techniques was used to characterize the Cassiar Batholith geochemically, and is presented below.

Major-Elements

The alkali-lime index (Peacock, 1931) was calculated for the Cassiar Batholith from major-element data (Figure 6). The intersection of the Na_2O+K_2O and CaO trends occurs at 56.5%, classifying the Cassiar Batholith as calc-alkaline. Similarly, an AFM ternary diagram (Figure 7) indicates a calc-alkaline trend for the Cassiar Batholith.

Harker diagrams (Harker, 1909) were plotted for all major and minor oxides in the 50 samples of the Cassiar Batholith (Figure 8). Most samples (48 out of 50) have greater than 65% SiO_2. With increasing silica contents, Al_2O_3, FeO, CaO, TiO_2, MgO, MnO, Na_2O, and P_2O_5 decrease, whereas K_2O increases. Such trends are typical for granitoid rocks. Except for the quartz monzonite and quartz syenite samples, the data define continuous linear trends with no distinct geochemical grouping of samples. The anomalously high K_2O and low CaO, FeO and MgO contents of the quartz monzonite and quartz syenite samples likely reflect accumulation of K-feldspar.

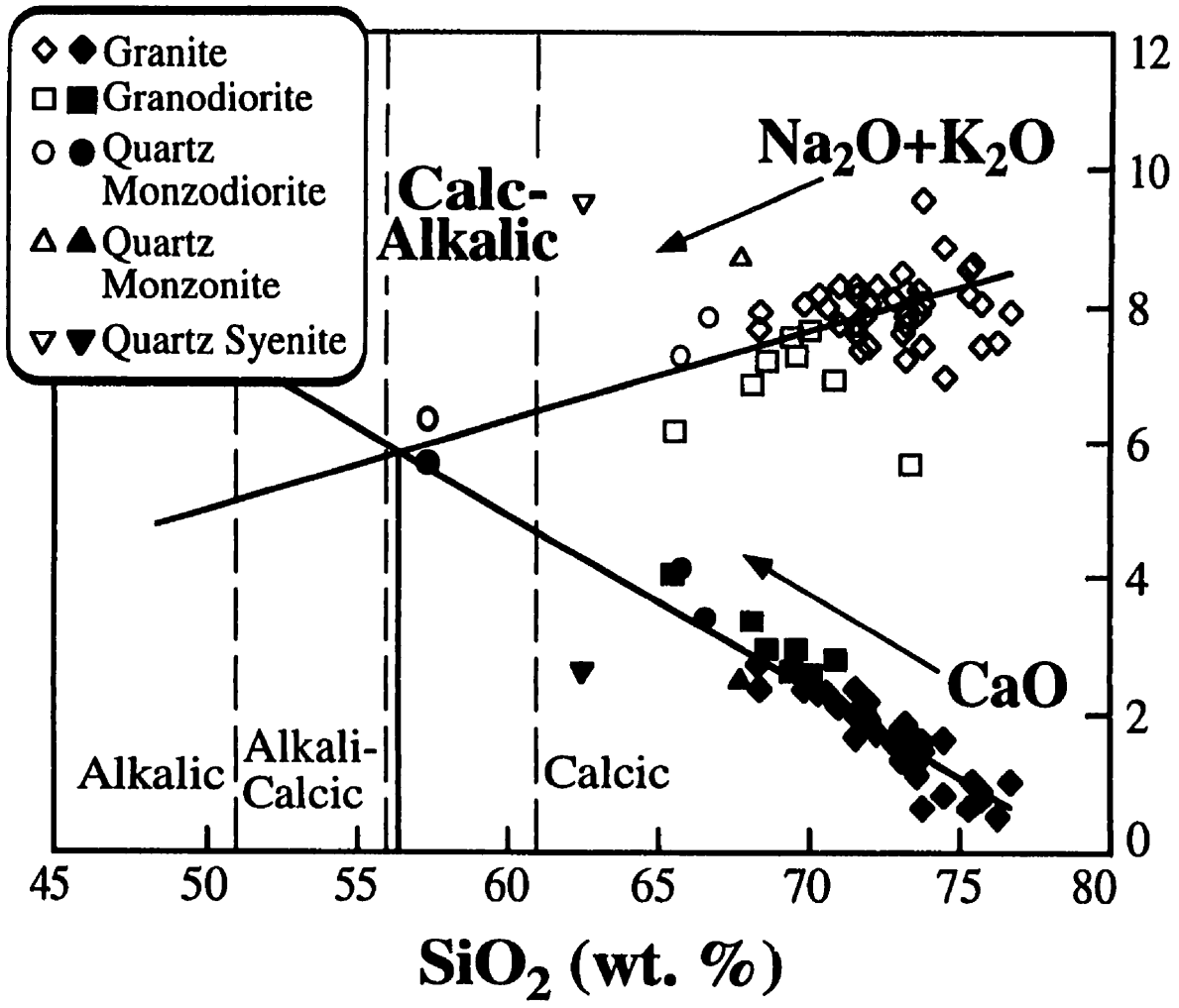

Figure 6. Alkali-lime index (Peacock, 1931) showing the calc-alkaline classification of the Cassiar Batholith.

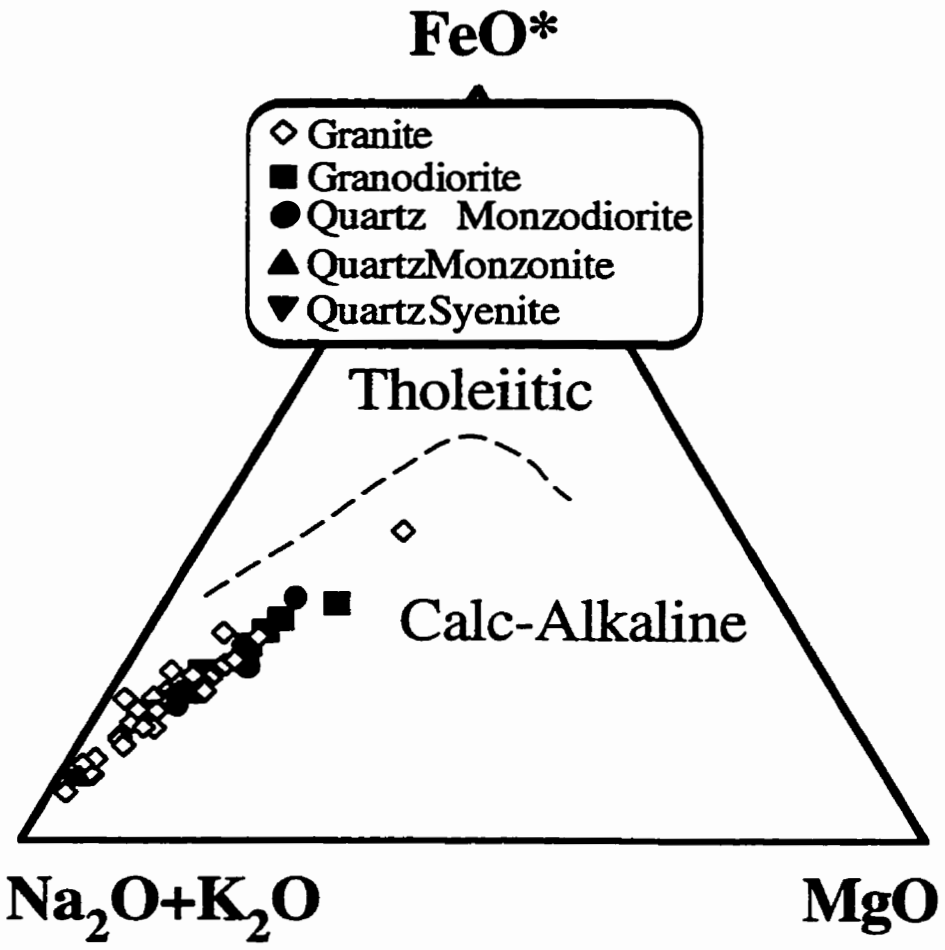

Figure 7. AFM Ternary for the Cassiar Batholith showing the calc-alkaline classification. Total Fe reported as FeO*.

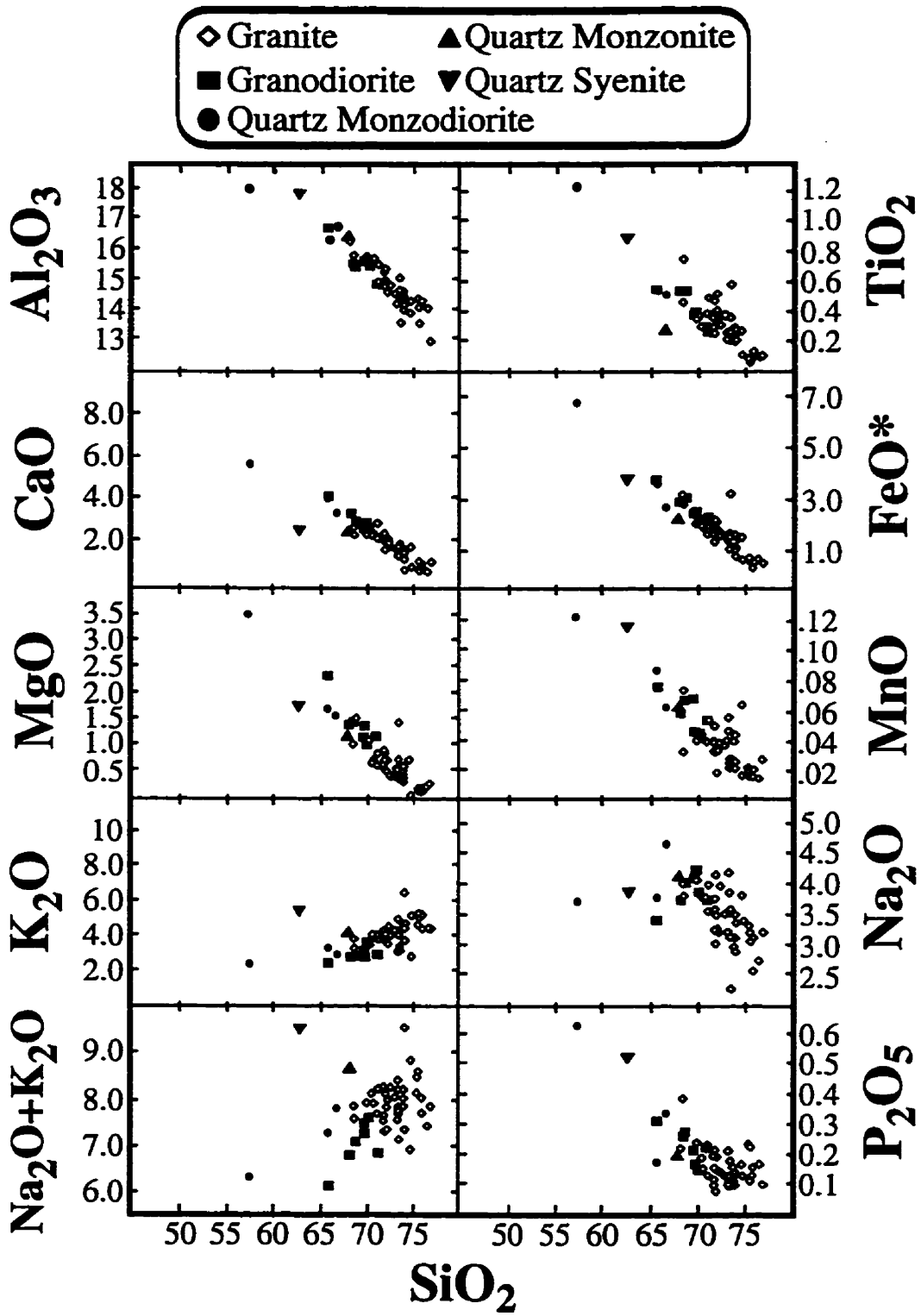

Figure 8. Major element oxide (in wt. %) Harker diagrams for the Cassiar Batholith.

Calculation of the alumina saturation index (molar ratio: $Al_2O_3/[CaO+Na_2O+K_2O]$) for the 50 samples show dominantly weakly to moderately peraluminous values (1.0 to 1.1) for the Cassiar Batholith (Figure 9), with fewer strongly peraluminous values (>1.1), and only four metaluminous samples (<1.0). In general, peraluminosity increases with increasing SiO_2.

Trace-Elements

Pearce-element tectonic discrimination diagrams are shown in Figure 10 (Pearce *et al.*, 1984). The Cassiar Batholith samples plot dominantly within the volcanic arc granite (VAG) and syn-collisional granite (syn-COLG) fields in all diagrams. Discrimination between these two fields is not possible on these diagrams as the Cassiar Batholith rocks have higher Ta contents then typical volcanic-arc granitoids but lower Rb contents than typical syn-collisional granitoids.

Rare-earth-element (REE) diagrams were plotted for each of the rock groups in the Cassiar Batholith (Figure 11) from chondrite-normalized ICP-MS data (Boynton, 1984). The Cassiar Batholith shows moderate to steep REE patterns with La_n/Yb_n higher (7 to 83) than for typical granitoid rocks (5 to 15). Eu anomalies are generally small, but become larger in the more felsic rocks.

"Spider diagrams" for incompatible elements were plotted (Figure 12) from ICP-MS data using normalization values from Pearce (1983). The diagrams show typical granitoid characteristics, with minor depletion in some HFS elements (TiO_2, Zr, P_2O_5), and minor enrichment in other HFS elements (Ta, Nb, Zr, P_2O_5) relative to MORB. LIL elements (K, Ba, Th, Rb), Sr, and LREEs are enrichment relative to MORB (Pearce, 1983). Minimal Ba depletion is noted.

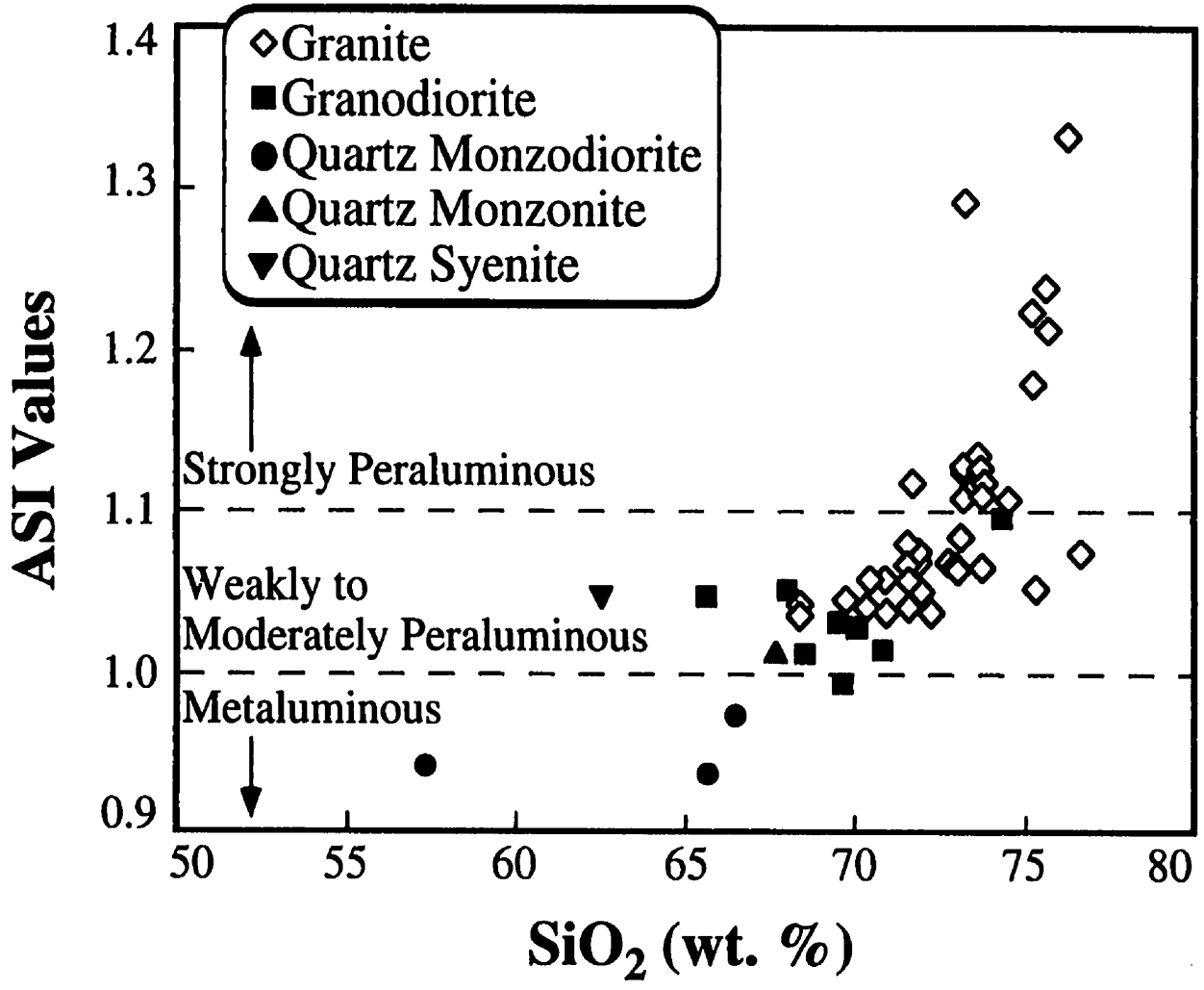

Figure 9. Alumina-saturation index [ASI--molar $Al_2O_3/(CaO+K_2O+Na_2O)$] values versus SiO_2 (wt. %) for the Cassiar Batholith.

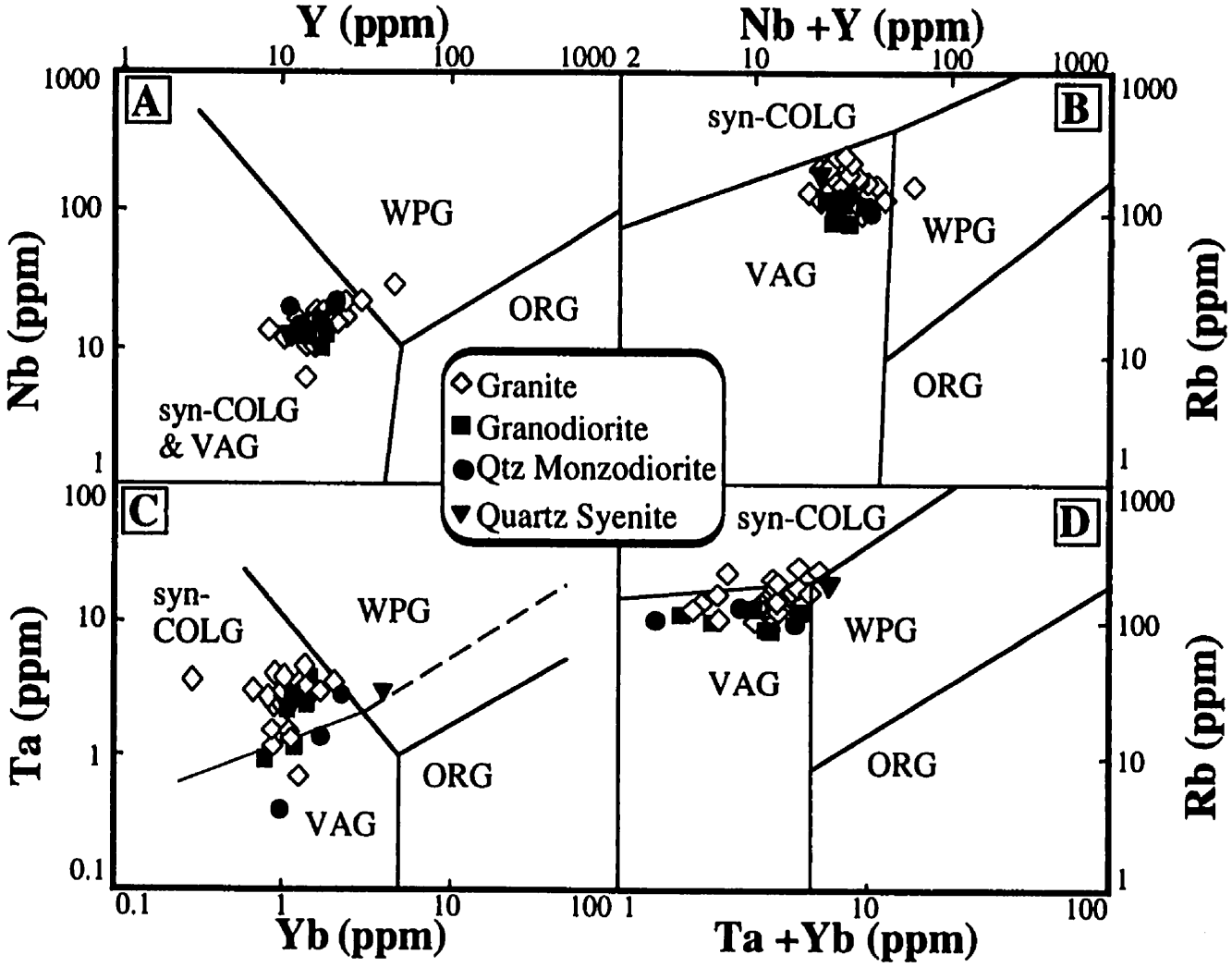

Figure 10. Pearce plots (Pearce *et al.*, 1984) for the Cassiar Batholith. WPG= within plate granite, VAG= volcanic arc granite, ORG= ocean ridge granite, syn-COLG= syn-collisional granite.

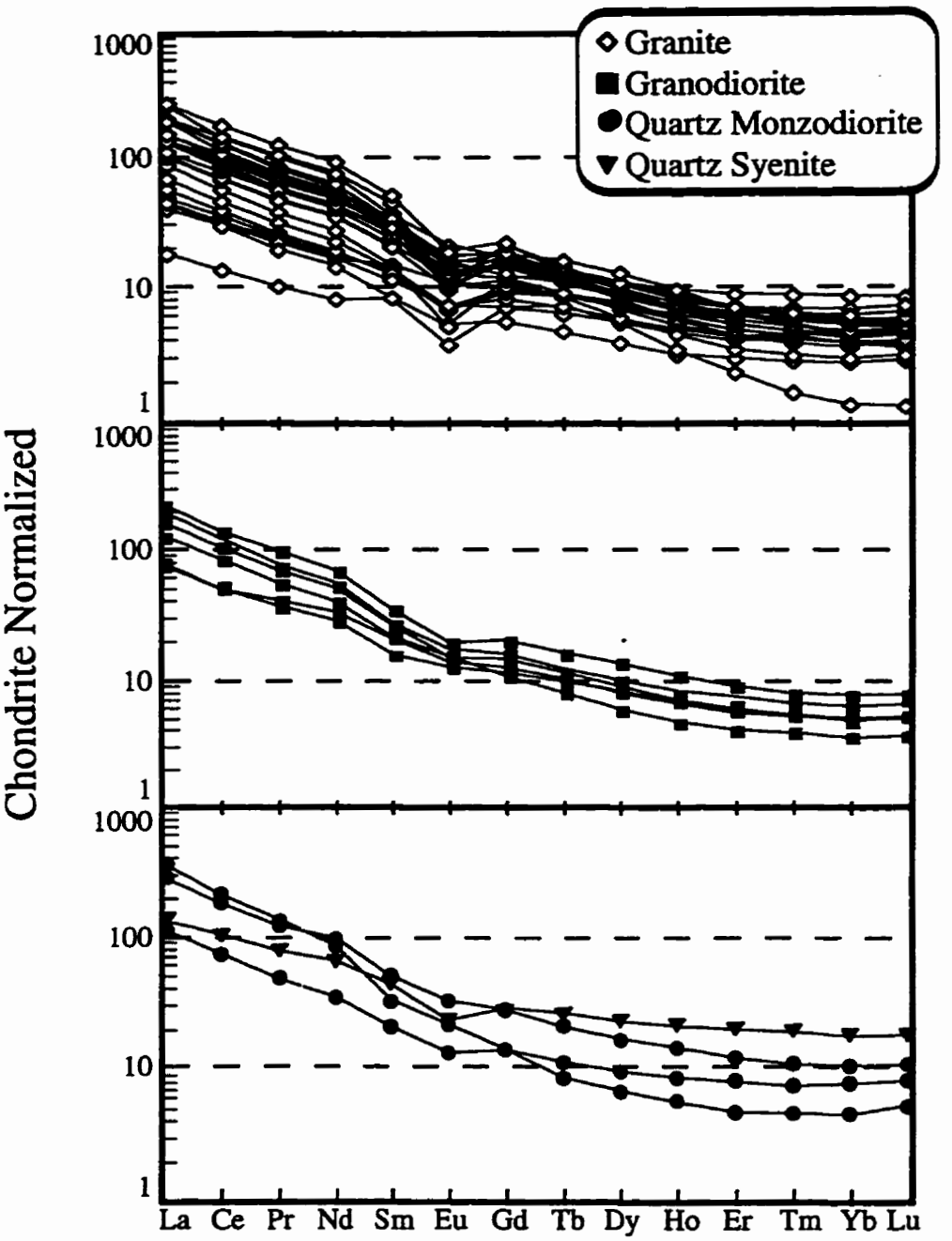

Figure 11. Chondrite normalized REE diagrams for the Cassiar Batholith.

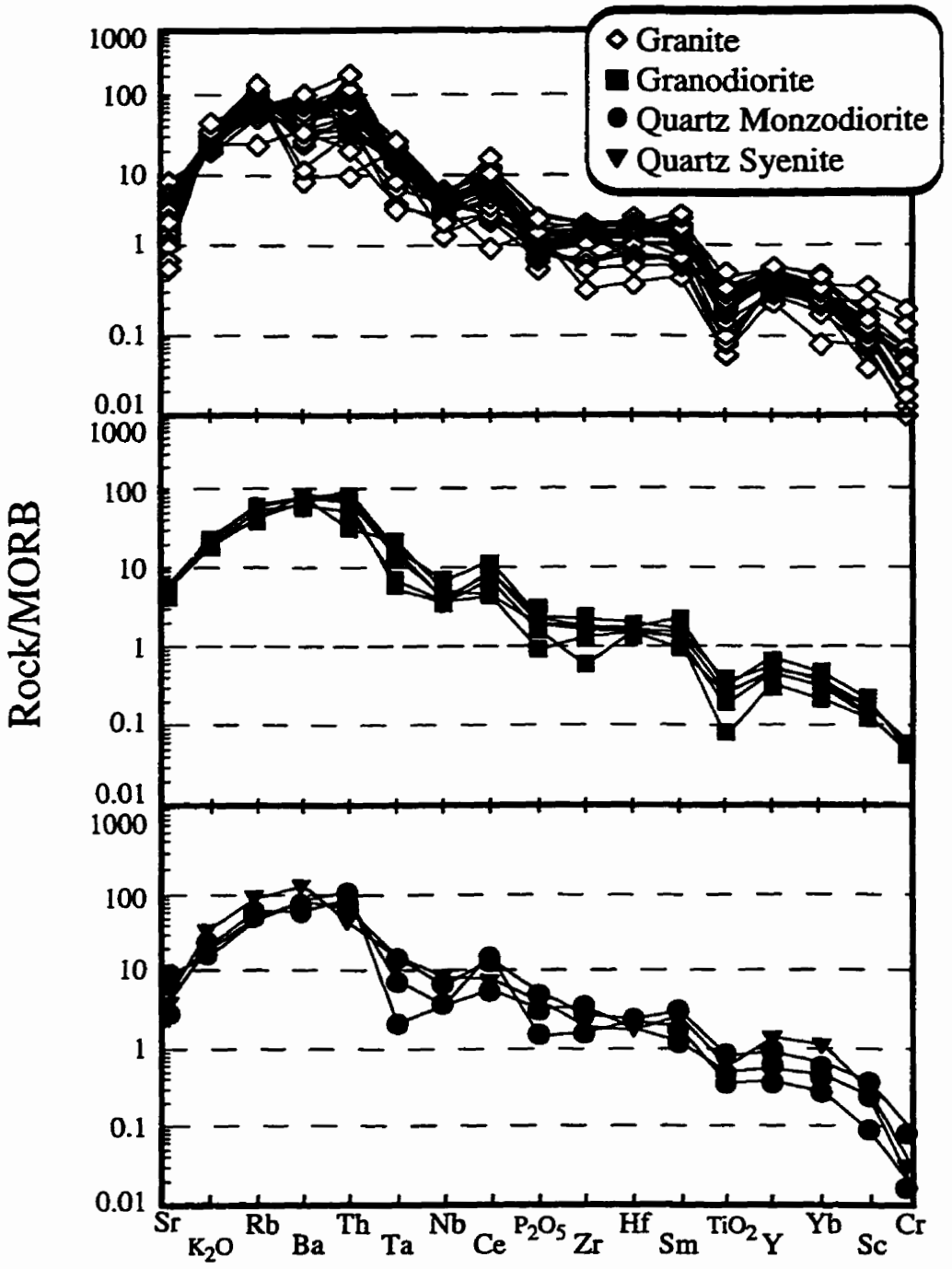

Figure 12. Rock/MORB normalized spider diagrams for the Cassiar Batholith.

Discussion of Major-, Trace- and Rare-Earth-Element Geochemistry

Major-, trace-, and rare-earth-element geochemistry proved useful in classifying the rocks of the Cassiar Batholith, as shown in both this and the previous section. However, interpretations based solely on the geochemistry are equivocal. The trends seen in the major element Harker diagrams and the ASI versus SiO_2 diagram showed that no distinct phases or groups within the Cassiar Batholith could be distinguished, and the patterns could reflect fractional crystallization of a single magma or mixing of magmas derived from multiple sources.

Tectonic interpretations based on the geochemistry alone are also equivocal. Calc-alkaline signatures in the alkali-lime index classification are commonly interpreted to result from subduction tectonics. Pearce plots, however, suggest that the Cassiar Batholith formed in either a continental-arc setting, as similar to by the Andes, or in a continent-continent collisional setting, as in the Himalayas or the European Alps. Therefore, major- and trace-element geochemistry is useful for classification, but provide no clear indication about the source material or tectonic setting of Cassiar magmatism.

ISOTOPE GEOCHEMISTRY

Introduction

In order to develop more comprehensive petrogenetic and tectonic models for the Cassiar granitoids, O, Sr, Nd, and Pb isotope analyses were carried out on representative samples from the full north-south strike length of the batholith. This multiple isotope approach provides information on both the petrological character and the crustal residence time of the granitoid source materials.

Analytical Procedures

Fourteen samples from various locations, representing the entire range of observed rock types, were selected for whole-rock $\delta^{18}O$ analysis, and five of these were analyzed for quartz–K-feldspar mineral separate pairs. 10-20 mg aliquots of powdered whole rock samples, and 10 mg aliquots of powdered mineral separates were analyzed. Samples were loaded into Ni tubes, and O was liberated using BrF_5. The O was then converted to CO_2, and run on a Finnigan MAT 252 mass spectrometer (technique adapted from Clayton and Mayeda, 1963). All $\delta^{18}O$ values are reported relative to SMOW and are normalized to yield a value of 9.6‰ for the NBS-28 quartz standard.

Using isotope dilution procedures at the University of Alberta, Sr and Nd isotope analyses were conducted on the same fifteen whole-rock granitoid samples and eight potential source rocks. Powdered samples were weighed and totally spiked with tracer solutions of ^{84}Sr and ^{87}Rb, and ^{150}Nd and ^{149}Sm and Sr spikes. The samples, contained in teflon vials, were then dissolved in 10 ml concentrated HF and 1 ml concentrated HNO_3 at 150°C for 7 days. After evaporation to dryness, fluorides were dissolved and converted to chlorides by the addition of 10 ml of 6N HCl and heating at 150° for 24 hours. These were again evaporated to dryness, and 6 ml of 0.75N HCl was added. Samples were then heated at 100° for 12 hours, then evaporated to dryness. The powder was then taken up in 3 ml of oxalic acid:HCl mixture, and centrifuged at 5000 rpm for 10 minutes. The supernate was then loaded into 10 cm cation columns containing 200 to 400 mesh Bio-Rad AG50W-X8 resin. Standard cation chromatography procedures were followed for Rb-Sr and REE separation. Rb and Sr were passed through the column a second time to further purify the samples. Nd was further separated from Sm using Di(2-ethylhexyl phosphate) chromatography (HDEHP). The purified Sr and Nd fractions were analyzed for isotopic composition using a VG354 mass-spectrometer. The purified Rb and Sm fractions were analyzed for

isotopic composition using a VG-Micromass-30 mass-spectrometer. Total procedural blanks for Nd and Sm are 0.5 ng. (Sm-Nd procedure after Creaser *et al.*, 1997; Rb-Sr procedure after Holmden *et al.*, 1996).

Using isotope dilution procedures at the University of Alberta, common Pb isotope analyses were conducted on six K-feldspar mineral separates from the Cassiar Batholith. K-feldspars were separated from crushed whole-rock samples using a Frantz isodymanic separator and heavy liquid techniques (TRE-acetone mixture). Mineral separates were then sieved to collect grains that were less than 70 microns. Optical tests and X-ray diffraction (XRD) confirmed the purity of the separates. The samples were ultrasonically cleaned in distilled acetone for approximately ten minutes and rinsed with millipore water before leaching. Approximately 300 mg of K-feldspar grains were leached over successive nights in 2N HCl, 6N HCl, 16N HNO_3, and 16N HNO_3 + one drop of 48% HF. The final residue was dissolved in 4:1 HF:HNO_3 mixture (Cumming and Krstic, 1991). Residues were dried under laminar flow of HEPA-filtered air, redissolved in 3N HBr, and dried before the final dissolution in 0.5N HBr. Pb was extracted using combined HBr and HBr-HNO_3 column chemistry modified after Lugmair and Galer (1992). Total blank for the entire chemical procedure was <278 pg, thus no blank corrections were applied. The samples were loaded with silica gel and H_3PO_4 on a Re filament and isotopic measurements were performed on a VG-Micromass-30 thermal ionization mass spectrometer in single collector mode, at 1250°C. Measured isotopic ratios were corrected against the recommended value for NBS-981 by Todt *et al.*, (1996) for mass fractionation (~0.14%/amu).

Results

Oxygen Isotope Compositions

With the exception of one sample with a lower value, $\delta^{18}O$ values for the Cassiar Batholith range from +9.0‰ to +11.6‰ (Table 1), which is toward the high end of the range for granitoids in general. Quartz monzodiorites and granodiorites show very little variation in $\delta^{18}O$ (0.4‰) from +9.0‰ to +9.4‰. The granites show the most variation, ranging from +7.6‰ to +11.6‰. These high $\delta^{18}O$ values are typical of granitoids derived from crustal sources.

Oxygen isotope fractionation factors between quartz--K-feldspar mineral pairs are 0.9‰ to 2.4‰, which is within the normal range for igneous rocks. This result suggests that there has not been extensive modification of primary igneous $\delta^{18}O$ values by subsequent hydrothermal activity for most of the Cassiar Batholith samples.

Strontium Isotope Compositions

Initial $^{87}Sr/^{86}Sr$ values (at 100 Ma) for the Cassiar Batholith range from 0.706 to 0.734 (Table 1). Again, these data are consistent with derivation of the granites from source rocks with a relatively long crustal residence time. There is minor overlap in values within the rock types; the quartz monzodiorites and the granodiorites represent the most juvenile material, ranging from 0.706 to 0.709 and 0.706 to 0.708, respectively. One granite sample has a value of 0.707, whereas the rest of the granite samples range from 0.709 to 0.734. Corresponding ε_{Sr} values were calculated, and are presented in Table 1.

Neodymium Isotope Compositions

Initial $^{143}Nd/^{144}Nd$ values (at 100 Ma) for the Cassiar Batholith are given in Table 1, and were converted to ε_{Nd} values for convenience. These entirely crustal values range from -3.5 to -17.9. The quartz monzodiorites and the granodiorites again represent the most

Table 1. Stable and radiogenic isotope data for selected samples of the Cassiar Batholith and contact aureole potential source rocks. BtMsGr= biotite hornblende granite; BtGr= biotite granite; BtHblGd= biotite hornblende granodiorite; BtGd= biotite granodiorite; BtHblQmd= biotite hornblende quartz monzodiorite; Sch= schist; Amph= amphibolite; Hfl= hornfels; QFG= quartzo-feldspathic gneiss. wr= whole rock. qtz= quartz. i= 100 Ma.

Sample	Rock Type	$\delta^{18}O$ wr (‰)	$\delta^{18}O$ K-spar (‰)	$\delta^{18}O$ qtz (‰)	Rb (ppm)	Sr (ppm)	$^{87}Rb/^{86}Sr$ meas.	$^{87}Sr/^{86}Sr$ meas.	$^{87}Sr/^{86}Sr_i$	εSr_i
CB Granitoids										
LAD96-2B	BtMsGr	11.6			119	245	1.377	0.711837(37)	0.70988	217
LAD96-13	BtMsGr	9.6	9.4	10.9	186	277	1.903	0.714355(25)	0.71165	70
LAD96-16	BtMsGr	7.6			162	256	1.796	0.713223(29)	0.71067	204
LAD96-22	BtMsGr	10.3			136	383	1.009	0.710710(34)	0.70928	69
BU 65-67	BtMsGr	9.8			252	175	4.084	0.723567(30)	0.71776	78
GAE 79-31	BtMsGr	10.2			172	195	1.370	0.721606(13)	0.71966	103
TO 66-78A	BtMsGr	9.8	9.1	11.4	252	155	4.619	0.725346(20)	0.71878	190
GA 88-43	BtMsGr				127	175	1.848	0.722795(13)	0.72017	224
GAC 67-18	BtMsGr	10.3	9.8	12.3	205	69.2	8.390	0.745523(20)	0.73360	415
GAH 77-82c	BtGr	10.2			127	461	0.7824	0.708277(60)	0.70717	33
LAD96-6	BtGr	9.4	8.7	10.8	118	589	0.5697	0.707488(19)	0.70668	40
GA 28/8/60-8	BtGr	9.5			103	428	0.6808	0.707132(14)	0.70616	89
LAD96-12	BtHblGd	9.2	9.0		84.3	605	0.3957	0.708629(21)	0.70807	52
LAD96-2A	BtHblQmd	9.4			95.0	1081	0.2494	0.706335(38)	0.70598	23
GA 88-45	BtHblQmd	9.0			128	356	2.076	0.712184(19)	0.70923	25
Potential Source Rocks										
MDS	Sch				160	209	2.178	0.759688(34)	0.75659	747
3VGS	Sch				185	207	2.532	0.770085(19)	0.76649	875
PE 2B	Sch				75.8	37.2	5.774	0.777622(20)	0.76942	917
MDA	Amph				17.7	130	0.3882	0.734670(17)	0.73412	420
3VGA	Amph				459	146	8.869	0.737867(18)	0.72526	293
PE 3A	Hfl				127	88.5	4.086	0.722645(18)	0.71684	179
GMC1C	Hfl				6.89	64.0	0.3054	0.715629(19)	0.71520	151
RC 3A	QFG				57.5	106	1.543	0.753318(19)	0.75113	664

Table 1 (continued)

Sample	Sm (ppm)	Nd (ppm)	$^{147}Sm/^{144}Nd$ meas.	$^{143}Nd/^{144}Nd$ meas.	$^{143}Nd/^{144}Nd_i$	εNd_i	T_{DM} Ga	$^{206}Pb/^{204}Pb$ K-spar	$^{207}Pb/^{204}Pb$ K-spar	$^{208}Pb/^{204}Pb$ K-spar
CB Granitoids										
LAD96-2B	2.67	12.6	0.1284	0.512050(8)	0.511660	-10.6	1.98			
LAD96-13	5.96	34.2	0.1054	0.512007(8)	0.511938	-11.1	1.62			
LAD96-16	5.55	31.2	0.1076	0.512072(6)	0.512002	-9.9	1.56			
LAD96-22	6.27	38.5	0.0986	0.512213(7)	0.512140	-7.0	1.26	19.158	15.703	39.14
BU 65-67	6.80	39.7	0.1035	0.511919(6)	0.511851	-12.8	1.72			
GAE 79-31	6.56	37.3	0.1064	0.511847(9)	0.511777	-14.3	1.86			
TO 66-78A	7.11	39.5	0.1089	0.511784(9)	0.511713	-15.5	2.00	19.219	15.710	39.26
GA 88-43	2.47	10.7	0.1392	0.511926(14)	0.511835	-13.2		19.144	15.705	39.14
GAC 67-18	3.11	12.0	0.1572	0.511694(7)	0.511591	-17.9		19.207	15.713	39.21
GAH 77-82c	6.36	42.0	0.0916	0.512283(10)	0.512223	-5.6	1.10			
LAD96-6	10.1	46.9	0.1304	0.512374(8)	0.512289	-4.3	1.44	19.222	15.718	39.22
GA 28/8/60-8	3.33	19.2	0.1048	0.512382(13)	0.512313	-3.8	1.09			
LAD96-12	5.58	34.4	0.0982	0.512310(8)	0.512246	-5.1	1.12	19.242	15.715	39.2
LAD96-2A	9.69	62.3	0.0941	0.512392(7)	0.512330	-3.5	0.98			
GA 88-45	4.21	23.1	0.1102	0.512234(9)	0.512162	-6.8	1.37			
Potential Source Rocks										
MDS	5.73	30.5	0.1135	0.511869(6)	0.511795	-13.9	1.96			
3VGS	9.61	50.7	0.1146	0.511890(6)	0.511814	-13.5	1.95			
PE 2B	6.74	36.1	0.1130	0.511546(7)	0.511468	-20.2	2.44			
MDA	5.36	23.7	0.1369	0.511972(8)	0.511882	-12.2	2.35			
3VGA	3.35	15.2	0.1335	0.512016(10)	0.511926	-11.3	2.17			
PE 3A	7.84	43.6	0.1087	0.512122(8)	0.512047	-8.9	1.51			
GMC1C	1.48	4.52	0.1979	0.511910(11)	0.511775	-14.2	11.7			
RC 3A	2.92	15.9	0.1107	0.511323(8)	0.511245	-24.5	2.71			

juvenile material, ranging from -3.8 to -6.8, and -3.8 to -5.1, respectively. The granites range from -5.6 to -17.9. Nd model ages (T_{DM}) (after Goldstein, 1984) for this suite of rocks range from 0.98 Ga to 1.98 Ga (Table 1).

Common Lead Isotope Compositions

Unlike the wide range in Sr and Nd isotope compositions, Pb isotope ratios for six K-feldspar separates are remarkably similar, irrespective of rock type (Table 1). $^{206}Pb/^{204}Pb$ values range from 19.144 to 19.242; $^{207}Pb/^{204}Pb$ values range from 15.703 to 15.718; $^{208}Pb/^{204}Pb$ values range from 39.14 to 39.26. The granodiorites have the two highest $^{206}Pb/^{204}Pb$ values, yet overlap with the granites in $^{207}Pb/^{204}Pb$ and $^{208}Pb/^{204}Pb$ values.

Potential Source Material Compositions

Eight samples of potential source material were analyzed for major- and trace- elements, and Sr and Nd isotopes. XRF and ICP-MS data are given in Appendices C and D, and radiogenic isotopes are given in Table 1. These samples of pelitic schists and hornfels, and amphibolites have very high crustal values, ranging from 0.715 to 0.769 in $^{87}Sr/^{86}Sr$, and from -8.9 to -24.5 in ε_{Nd}.

Discussion of Isotope Geochemistry

The wide range in Sr and Nd isotopic compositions indicate that a single, homogeneous source rock could not have produced the full range of Cassiar magmas. Rather, the data demand multiple magma sources. This hypothesis is supported by the linear array of data on the Sr (ppm) versus ε_{Sr} diagram (Figure 13) and the curved data array on the ε_{Nd} versus ε_{Sr} diagram (Figure 14). Such data arrays are characteristic of magma suites that have formed either by the mixing of magmas generated from two compositionally and

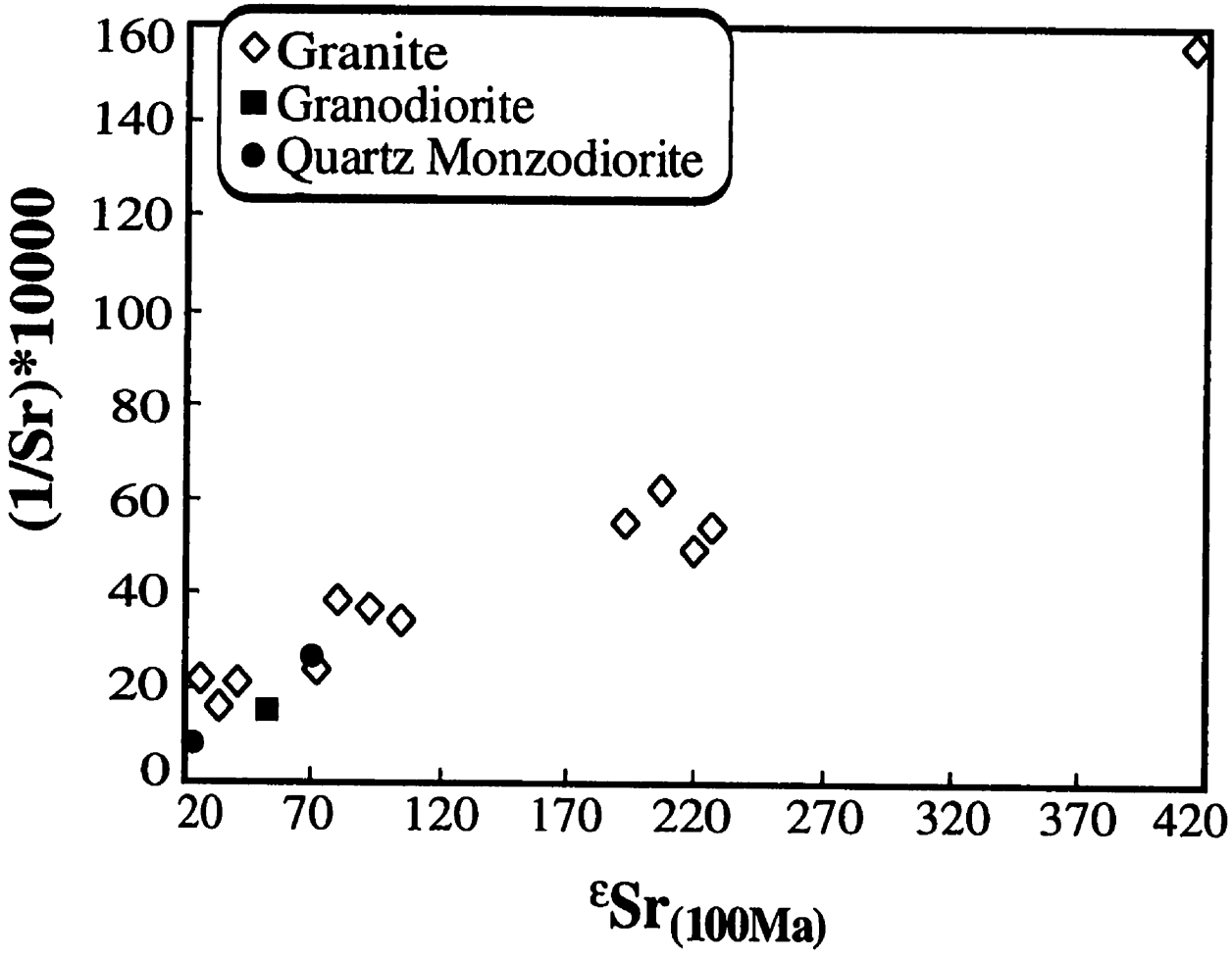

Figure 13. (1/Sr (ppm))*10000 vs. ε_{Sr} showing the linear array of data for the Cassiar Batholith.

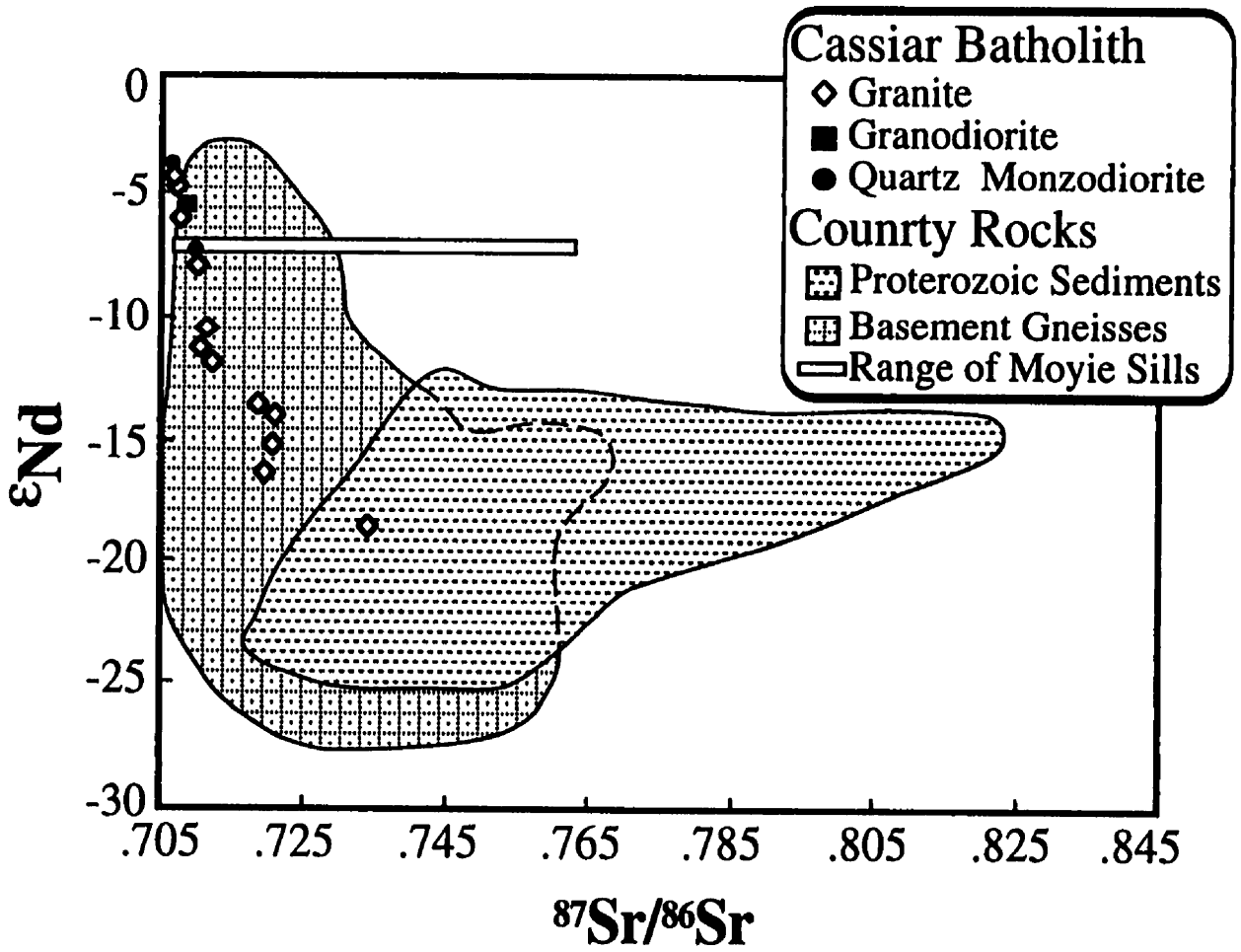

Figure 14. ε_{Nd} vs. initial $^{87}Sr/^{86}Sr$ for Cassiar Batholith granitoids, Proterozoic sediments, (Ghosh & Lambert, 1989; present study), Precambrian basement gneisses (Lambert & Chamberlain, 1990), and Moyie Sills (Burwash & Wagner, 1988; Burwash pers. com.).

isotopically distinct source rocks, or by assimilation of ancient crustal rocks by mafic, mantle-derived magma (Taylor and Sheppard, 1986; DePaolo *et al.*, 1992). In either case, the Cassiar magmas bear the imprint of both mafic and felsic sources.

Pb isotope compositions for the Cassiar Batholith were plotted against evolution models by Stacey and Kramers (1975) and Zartman and Doe (1981). Relative to the simple Stacey and Kramers evolution model (Figure 15a), Cassiar Batholith samples plot in the future, and comparison of the data is not valid. However, in the more complex evolution models of Zartman and Doe (1981), a relationship can be established between the Cassiar Batholith samples and various crustal and mantle reservoirs. Figure 15b also plots $^{208}Pb/^{204}Pb$ against $^{206}Pb/^{204}Pb$, with the Cassiar Batholith data plotting slightly above the Upper Crustal evolution, near 100 Ma. This relationship is shown even more strongly in Figure 15c, where $^{207}Pb/^{204}Pb$ is plotted against $^{206}Pb/^{204}Pb$, and the values for the Cassiar Batholith plot directly on the Upper Crust evolution trend near 100 Ma. These comparisons suggest that the Pb in the Cassiar Batholith is derived from entirely crustal sources with high time-integrated U/Pb and Th/Pb.

Source Materials

The isotopic data indicate that the source material for the Cassiar Batholith includes a more evolved end-member and a more juvenile end-member. The more evolved source, which was the primary contributor to the granites (*sensu stricto*) of the Cassiar Batholith, was peraluminous, had high initial $^{87}Sr/^{86}Sr$ ratios and $\delta^{18}O$ values, and strongly negative ε_{Nd} values. These geochemical and isotopic features are characteristic of Meso- to Neoproterozoic metasedimentary rocks and some basement gneisses that are present in many parts of the Omineca Crystalline Belt (Garzione *et al.*, 1997; Ghosh and Lambert, 1989; Boghossian *et al.*, 1996) (Figure 14). The 0.98 Ga to 1.98 Ga Nd

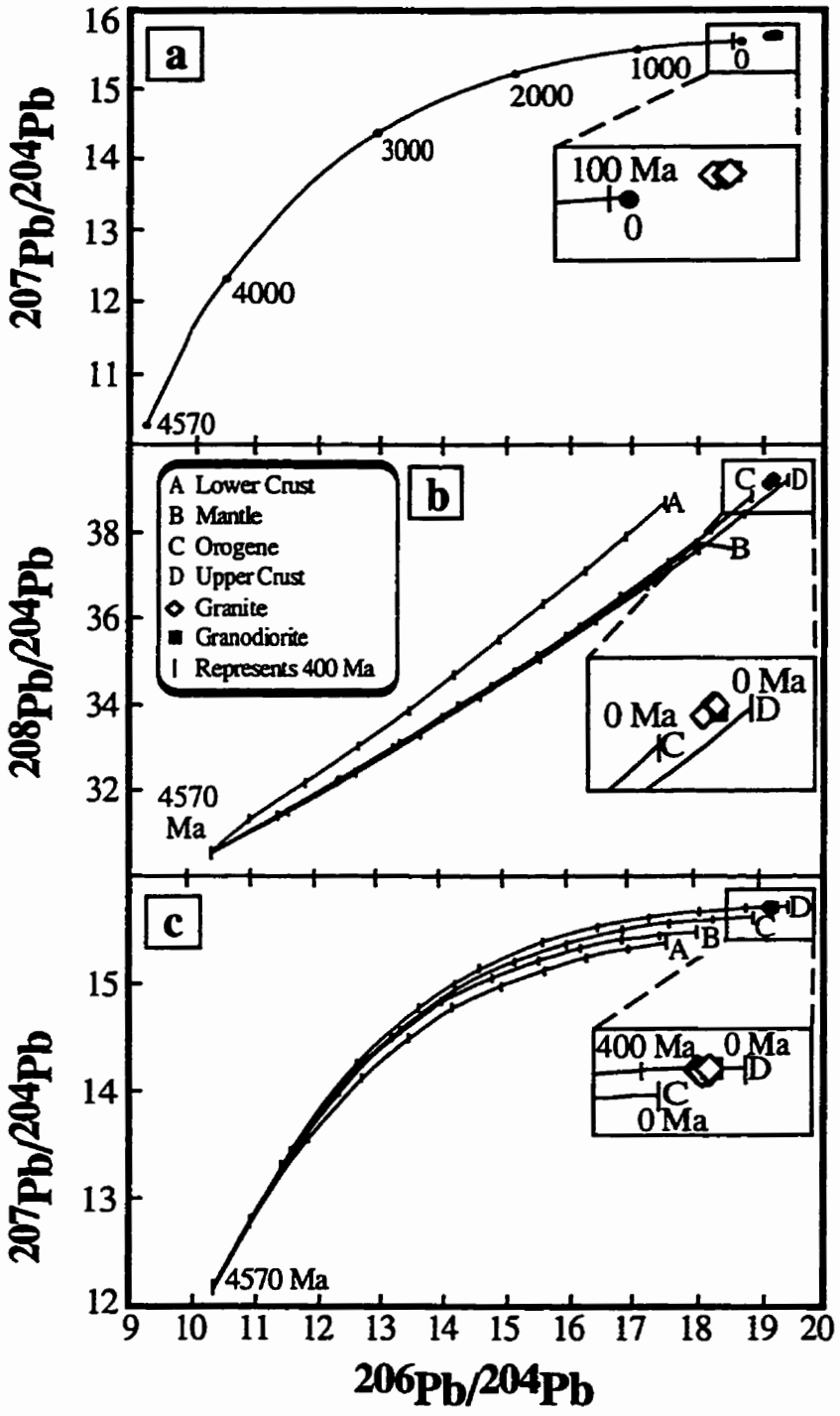

Figure 15. Pb data for the Cassiar Batholith plotted with the Pb evolution models of (a) Stacey & Kramers (1975), and (b) and (c) Zartman & Doe (1981).

model ages of the Cassiar granitoids also overlap those of most of the metasedimentary rocks.

The nature of the mafic source is more problematic. This source was metaluminous rather than peraluminous, had less evolved isotopic signatures than the felsic source, but still possessed distinctly crustal isotopic ratios. One possibility is that this source was a basaltic magma, generated in the mantle at ~100 Ma, that interacted and mixed extensively with melts derived from Proterozoic-age continental crust.

Arguing against this possibility is the general absence of reported mid-Cretaceous age basaltic magmatism, either in the vicinity of the Cassiar Batholith or throughout the Omineca Crystalline Belt. Thus, if a mafic magma did exist, it must have thoroughly mixed with a felsic magma to form an intermediate magma composition. Although such hybridization of magmas is chemically viable, it is inhibited physically because of large differences in the viscosity, density, and solidus temperatures of mafic and felsic magmas (Kay *et al.*, 1992). To homogenize, the mafic magma must make up greater than half of the total mass of magma, or the two magmas must have a compositional difference of <10 wt. % SiO_2 (Kay *et al.*, 1992). As a result of these physical barriers to mixing, vestiges of a partially completed mixing process are commonly preserved in the form of syn-plutonic mafic dykes and enclaves within larger granitoid bodies (e.g., Roddick and Armstrong, 1959; Hyndman and Foster, 1988). No such features were observed in the Cassiar Batholith nor have they been reported from lithologically similar mid-Cretaceous plutons from southeastern British Columbia (Brandon and Lambert, 1993; 1994). These observations suggest that the less evolved magmas of the Cassiar Batholith were not formed by direct mixing of felsic and mafic magmas.

Another mechanism for producing magmas with a range of isotopic compositions is the process of assimilation and fractional crystallization (AFC). That is,

a basaltic magma assimilates varying amounts of crustal material. The heat necessary for assimilation is supplied by crystallization of minerals in the basalt magma. Figure 16 shows the AFC evolution of a typical calc-alkaline basalt end-member (Sr (ppm)= 500; $^{87}Sr/^{86}Sr_i$= 0.7035; Nd (ppm)= 15, ε_{Nd}= +5) versus an average value of Proterozoic sediments from the Omineca Crystalline Belt (Sr (ppm)= 133.3; $^{87}Sr/^{86}Sr_i$= 0.7654; Nd (ppm)= 35.3, ε_{Nd}= -15.25) (Ghosh and Lambert, 1989; present study). The AFC curves were calculated using the equations of Taylor (1986). For modeling, I used distribution coefficients of 0.2 and 2.0 for Nd and Sr, respectively, which are reasonable values for much of the crystallization history of basaltic magmas (Nielsen, 1989). Another important input parameter is the so-called r values, the ratio of assimilated material to fractionally crystallized cumulates. The value of the parameter depends primarily on the temperature of the crust before incorporation into the basalt magma. A low value of r (e.g. 0.3) corresponds to assimilation of cool crust; a high r value (e.g., 0.9) corresponds to a very hot crust. In fact, an r value of 0.9 corresponds to crust that has been pre-heated to a temperature of approximately 900°C before incorporation into the basaltic magma. At those very high temperatures, crust will melt extensively even without mafic magma heat input (e.g., Patiño Douce and Johnston, 1991). Thus, I believe that 0.9 provides an absolute upper bound of r values for the calculations. As can be seen in Figure 16, neither the r= 0.3 of r= 0.9 curves pass through the entire array of Cassiar Batholith data points. This indicates that assimilation of a single metasedimentary source rock by basaltic magma cannot account for the isotopic variation present in the batholith. More elaborate AFC models remain possible. For example, assimilation of an isotopically more juvenile crustal source rock by a basaltic magma, could, in principle, produce the granodiorites and quartz monzodiorites of the Cassiar Batholith. Mixing between these more mafic Cassiar magmas and felsic magmas derived from partial melting of a metasedimentary source rocks could generate

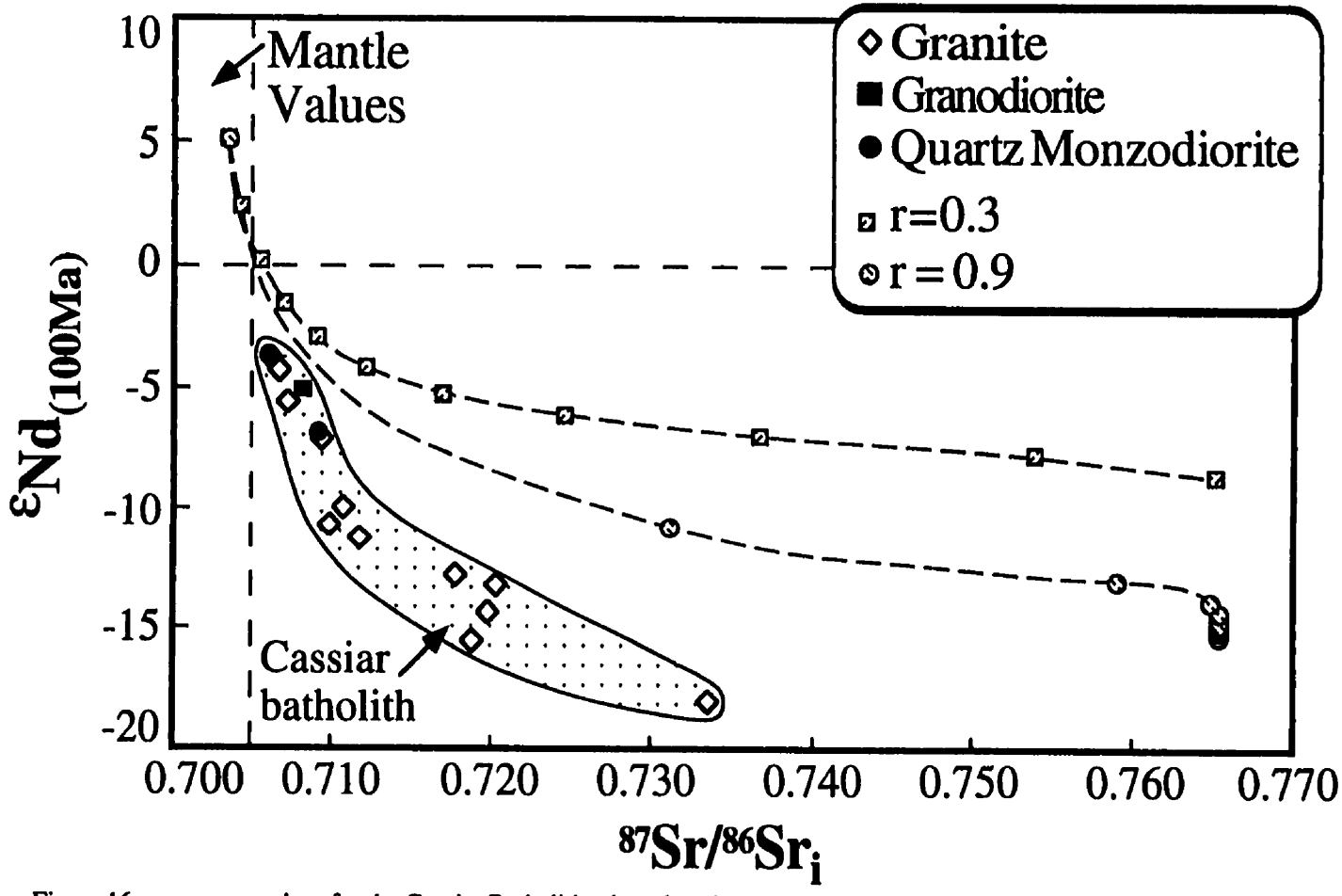

Figure 16. ε_{Nd} vs. ε_{Sr} values for the Cassiar Batholith, plotted against two AFC models. Parameters for the AFC model: Typical calc-alkaline basalt end-member: Sr (ppm)= 500, $^{87}Sr/^{86}Sr_i$= 0.7035, Nd (ppm)= 15, ε_{Nd}= +5. Typical meta-sedimentary value: Sr (ppm)= 133.3, $^{87}Sr/^{86}Sr_i$= 0.7654, Nd (ppm)= 35.3, ε_{Nd}= -15.259. Distribution coefficient values: D_{Nd}= 0.2 and D_{Sr}= 2.0. r values: stippled circles, r= 0.3 (T= 100°C) and stippled squares r= 0.9 (T= 900°C). Points along AFC curves represent liquid remaining in 10% incriments.

the remainder of the Cassiar data array. There is, however, no geological evidence with which to evaluate this possibility.

Another mechanism for generating the range of isotopic compositions present in the Cassiar Batholith is by mixing magmas derived from two compositionally and isotopically distinct crustal source rocks. One source rock end-member could be the Proterozoic-age metasedimentary rocks of the Omineca Crystalline Belt. The second crustal end-member would be ancient mafic material; that is, Proterozoic-age basaltic to dioritic composition rocks that were tectonically buried and then partially melted at ~100 Ma to give rise to the more mafic magmas in the Cassiar Batholith (granodiorites and quartz monzodiorites). The lower Rb/Sr and higher Sm/Nd ratios of ancient, basaltic composition source rock would give rise to less evolved, though still distinctly crustal isotopic ratios with time. It is interesting to note that basaltic lavas and sills are widespread in both the Meso- and Neoproterozoic supracrustal sequences in the Omineca Crystalline Belt (Devlin, *et al.*, 1988; Narbonne and Aitken, 1995; Høy, 1989; Burwash and Wagner, 1988). Similarly, mafic rocks are present in the underlying basement complex (Lambert and Chamberlain, 1990). Figure 14 presents the fields of available data for Proterozoic metasediments (Ghosh and Lambert, 1989; present study), mafic basement material (Lambert and Chamberlain, 1990), and the Moyie Sills (Burwash and Wagner, 1988; Burwash pers. comm.), and shows the Cassiar Batholith samples in relation to these values. A calculated mixing line between the most mafic and most felsic end-members of the Cassiar granitoids passes through the data set (Figure 17). The important point to note is that the isotopic composition of the entire range of Cassiar samples overlap those of available crustal source rocks, which is consistent with the idea that the Cassiar magmas were derived from such sources.

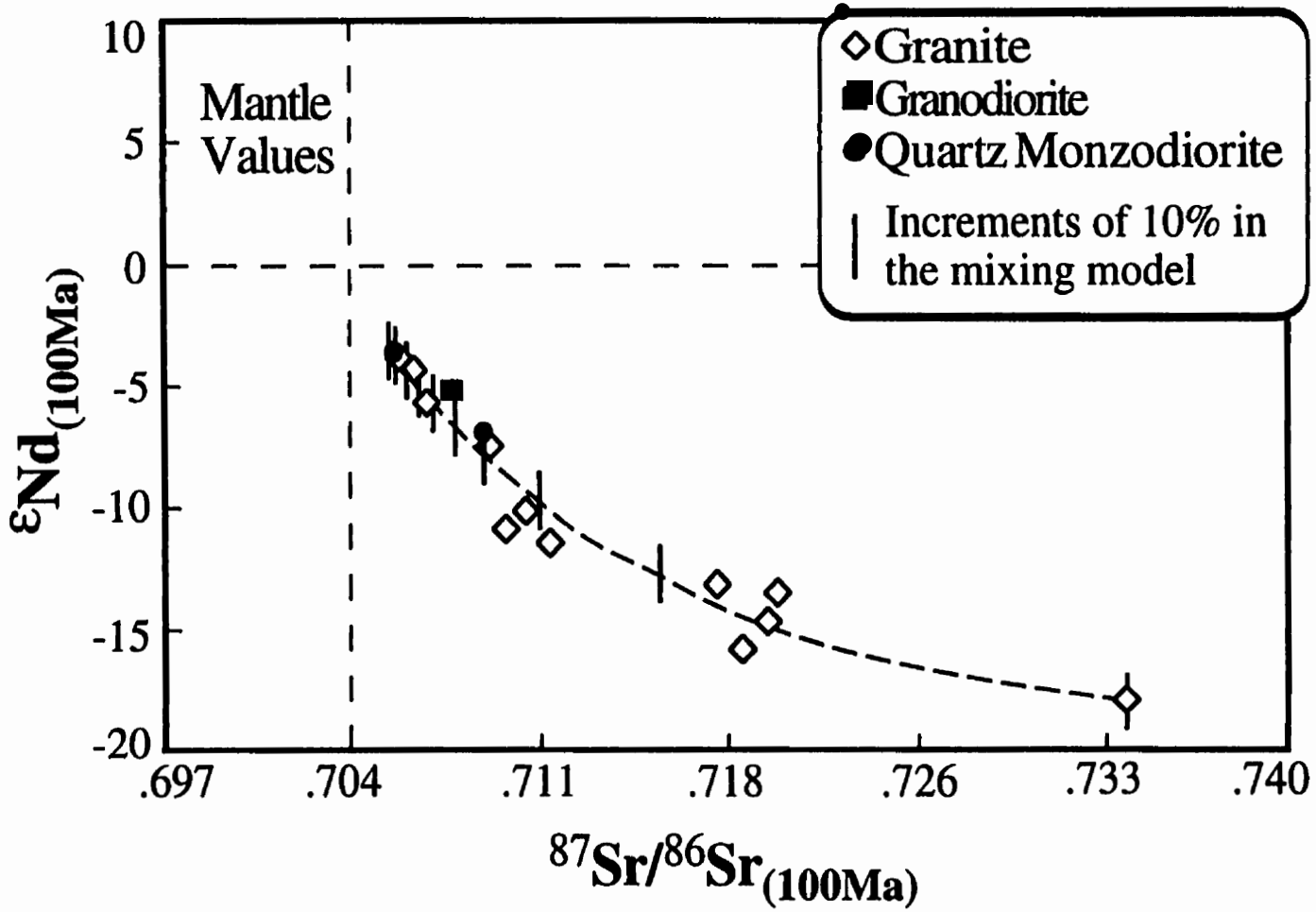

Figure 17. ε_{Nd} vs. ε_{Sr} for the Cassiar Batholith, in comparison to a mixing model using the most mafic (LAD96-2A) and the most felsic sample (GAC 67-18). Cassiar mafic sample parameters: $^{87}Sr/^{86}Sr$= 0.706, Sr (ppm)= 1083. Cassiar felsic granitoid parameters: $^{87}Sr/^{86}Sr$= 0.734, Sr (ppm)= 69.2.

Comparison of the Cassiar Batholith with other CIZ batholiths

In this section, the chemical and isotopic composition of Cassiar Batholith is compared to several CIZ intrusions, including the southeast British Columbia batholiths (SEBCB), the Spirit pluton in northeastern Washington, and the Idaho batholith.

The Cassiar Batholith, as stated earlier in this paper, consists dominantly of biotite ± muscovite granites (37), followed by granodiorites (8), quartz monzodiorites (3), quartz diorite (1) and quartz syenite (1). Hornblende occurs in only six of the 50 samples examined in this study. SiO_2 weight percentages range from 57% to 77%, averaging 70%, with only two of the fifty samples having SiO_2 contents below 65%. $\delta^{18}O$ values range from +7.6‰ to +11.6‰, averaging 9.7‰, with 93% of samples greater than 8‰. Initial Sr ratios range from 0.706 to 0.734, and average 0.713, with all samples greater than 0.706. ε_{Nd} values range from -3.5 to -17.9, and average -9.4.

The SEBCB comprise the White Creek, Bugaboo, Fry Creek, and the Horsethief Creek batholiths, all of which were studied by Brandon and Lambert (1993; 1994). The dominant rock type within the SEBCB is granite (22), followed by granodiorite (12), and quartz monzodiorite (2). Biotite ± muscovite are abundant in these samples, and hornblende is a minor varietal mineral, occurring in only three of the 27 samples. SiO_2 weight percentages ranges from 61% to 78%, averaging 71%. $\delta^{18}O$ (for the White Creek Batholith only) range from 6.8‰ to 10.3‰, averaging 8.5‰. Initial Sr ratios range from 0.707 to 0.737, and average 0.713. Initial ε_{Nd} range from -4.8 to -20.8, averaging -9.4.

The Spirit pluton in northeastern Washington was studied in detail by Driver (1995) and Driver *et al.* (in prep). It is composed of granites (4), granodiorites (2), and quartz monzodiorite (2). Biotite ± minor muscovite ± minor hornblende are the varietal minerals. SiO_2 weight percentages range from 65% to 72%, averaging 69%. $\delta^{18}O$ ranges from +8.4‰ to +10.2‰, with an average of 8.9‰. Initial Sr ratios range from

0.708 to 0.709, and average 0.709. Initial ε_{Nd} values range from -5.3 to -6, and average -5.6.

The Idaho batholith is the largest of the CIZ batholiths, and comprises two main phases, the Atlanta lobe, to the south, and the Bitterroot lobe to the north. Studies on Idaho batholith petrology, geochemistry, isotope geochemistry, and tectonic evolution include works by Hyndman (1983; 1984), Fleck and Criss (1985), Criss and Fleck (1987), Lewis *et al.* (1987), Toth (1987), Hyndman and Foster (1988), Fleck (1990), and Manduca (1993). The Idaho batholith is dominantly composed of granite and granodiorite, with quartz monzonite, quartz diorite, and tonalite abundant only in some marginal phases to the batholith in restricted localities (Lewis *et al.*, 1987; Toth, 1987). Biotite ± muscovite are the dominant varietal minerals within the main phase granites and granodiorites, with hornblende reported in the more mafic rock types (tonalites, quartz diorites, some granodiorites) (Lewis *et al.*, 1987; Toth, 1987). Sampling of the Atlanta lobe by Lewis *et al.* (1987) shows SiO_2 contents ranging from 61 wt. % to 78 wt. %, averaging 70 wt. %. Similarly, the main phase of the Bitterroot lobe comprises mainly granodiorites and granites with minor quartz monzodiorite and quartz monzonites (Hyndman, 1984). The chemical composition of this lobe is very homogeneous, averaging 71 wt. % SiO_2. Criss and Fleck (1987) report $\delta^{18}O$ values for the Bitterroot lobe ranging from +6‰ to +10.8‰, averaging 9.0‰. Initial Sr values from that study range from 0.706 to 0.719, with an average of 0.711. Fleck (1990) reports data from the main phase of the Atlanta lobe. $\delta^{18}O$ values range from +8.5‰ to +12.1‰, averaging 10.2‰. Initial Sr values from that study range from 0.704 to 0.732, with an average of 0.711, and 80% of the samples have values greater than 0.706. ε_{Nd} values range from +6.3 to -15.3, and average -8.

Despite being spread out over a strike-length of more than 1800 km, there are remarkable lithological, geochemical and isotopic similarities between the Cassiar

Batholith and the other CIZ intrusions. Common features include the dominance of granitic and granodiorite lithologies, over tonalites and quartz diorites, the general restriction of samples to high SiO_2 contents (>65 wt. %) and high $\delta^{18}O$ values (mainly >8.5‰), a wide range but overall high initial Sr ratios (>0.706), and low initial ε_{Nd} values (<-5). These similarities suggest a commonality in source materials and possibly also tectonic setting for the various CIZ batholiths. In this regard, it is important to note that all of these batholiths intruded through Paleoproterozoic basement rocks and Meso- to Neo-Proterozoic supracrustal rocks of the western North American miogeocline. As discussed above, such rocks represent viable sources for the Cassiar magmas. Brandon and Lambert (1993; 1994) reached a similar conclusion for the SEBC batholiths and proposed that magmatism occurred in response to crustal thickening in the Cordilleran interior. The origin of the Idaho batholith is more problematic. Unlike the Cassiar or SEBC batholiths, the Bitterroot lobe of the Idaho batholith has an associated mafic component which occurs in the form of numerous syn-plutonic dykes (Hyndman and Foster, 1988). Although this mafic magmatism likely provided a heat source for crustal melting, most workers agree that the Precambrian basement and metasedimentary cover rocks were the main contributor to the Idaho batholith magmas (Hyndman, 1984; Lewis *et al.*, 1987; Toth, 1987; Fleck, 1990). Thus, the common theme in CIZ magmatism is intra-crustal melting; a significant mantle contribution to magmatism, although present in cases such as the Idaho batholith, does not appear to be required.

Comparison of CIZ and Subduction-Related Batholiths

In order to establish the tectonic setting of the Cassiar Batholith, and the CIZ intrusions in general, it is instructive to compare these batholiths with known subduction-related magmatism in the Andes, the Himalayas, and the North American Cordillera. The comparison encompasses the Central Volcanic Zone (CVZ) of the Andes in Peru,

Bolivia, Argentina, and Chile, the pre-collisional Transhimalayan batholith (THB) of the Himalayas in Tibet, India, and Pakistan, the Coast Plutonic Complex (CPC) of Alaska and British Columbia, the Coast Ranges batholith (CRB) and the Sierra Nevada batholith (SNB) of California, and the Peninsular Ranges batholith (PRB) of California and Mexico.

Petrological and isotopic data on igneous rocks from the Andes serve as a template for interpreting continental margin magmatism through geologic time. Magmatism in the Andes is thought to have originated in the upper mantle, and, through a process of combined fractional crystallization and crustal assimilation, evolved to generate a range of magma compositions from basalt to rhyolite (James, 1982). Magmatism in the CVZ differs from other parts of the Andes in that subduction has occurred under unusually thick continental crust (60 to 70 km), providing the greatest possible opportunity for contamination of mantle-derived magmas by crustal material (Harmon, *et al.*, 1984). The 2500 km long Transhimalayan batholith formed in a broadly similar environment. It is the product of northward subduction of oceanic crust beneath the continental margin of Asia, which preceded the India-Asia collision (Debon *et al.*, 1986; Crawford and Searle, 1992). The intrusions of the North American coast also formed in subductional tectonic regimes.

There are major lithological differences between the CIZ granitoids and those produced in known subduction-related tectonic settings. Granitoids associated with subduction have a wide range of lithological compositions, from quartz diorite to granite; tonalites and granodiorites are typically the most abundant. In contrast, the CIZ intrusions dominantly comprise granite and granodiorite compositions, with rare tonalite and quartz diorite components (Figure 18). Subduction-related granitoids have SiO_2 contents spanning a larger range (47 wt. % to 75 wt. %), and much lower SiO_2 averages (61 wt. % to 65 wt. %) than those of CIZ granitoids (average ~70 wt. %). Additionally,

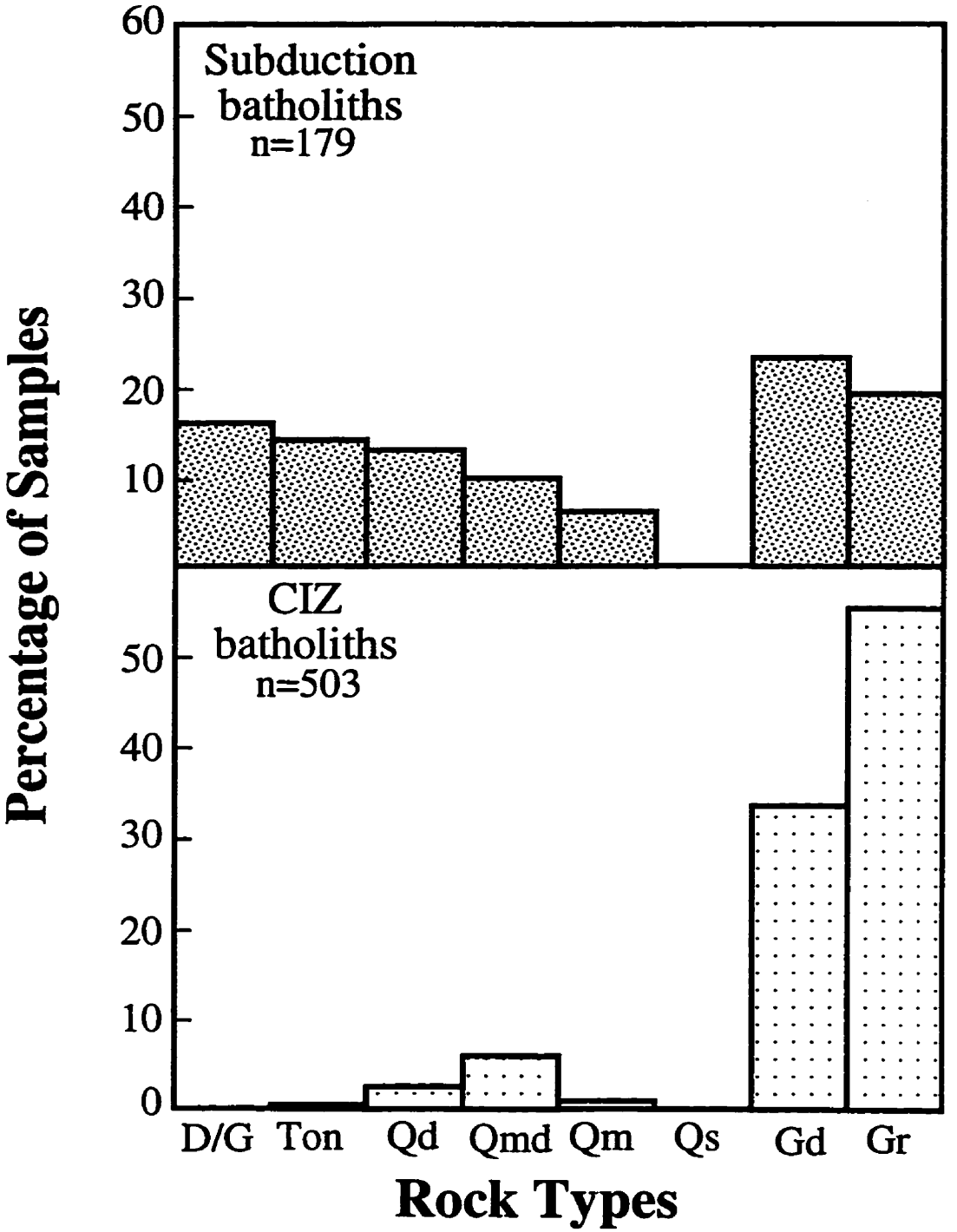

Figure 18. Comparison of rock types for the subduction and CIZ batholiths. Subduction= CVZ (Longstaffe *et al.*, 1983); THB (Debon *et al.*, 1985; Crawford & Searle, 1992); CPC (Cui & Russell, 1995a); SNB (Sawka *et al.*, 1990; Pickett & Saleeby, 1994; Coleman *et al.*, 1992; Friedman *et al.*, 1995). CIZ= CB (this study); SP (Driver *et al.*, in prep); SEBCB (Brandon & Lambert, 1993; 1994); IB (Toth, 1987).

rocks with less than 65 wt. % are common in subduction-related settings but are rare in the CIZ. Finally, there are mineralogical distinctions between the two suites of granitoids. Subduction-related rocks are typically rich in both hornblende and biotite, whereas primary muscovite is uncommon (Debon *et al.*, 1985; Crawford and Searle, 1992; Harmon *et al.*, 1984; Cui and Russell, 1995a; Barker *et al.*, 1986; Sawka *et al.*, 1990; Coleman *et al.*, 1992). In contrast, hornblende is normally minimal or absent, whereas biotite and muscovite are the common varietal minerals in the CIZ intrusions.

Stable and radiogenic isotope compositions also provide distinction between typical subduction-related magmatism and the CIZ intrusions. $\delta^{18}O$ values of the two suites are displayed graphically in Figure 19. 64% of the subduction-related samples have $\delta^{18}O$ values less than 8.5‰, whereas 70% of the CIZ samples have values greater than 8.5‰. Distinct populations are also seen in initial Sr ratios (Figure 20). 56% of subduction samples have initial Sr ratios below 0.706, whereas 93% of CIZ samples above 0.706. Similarly, most subduction granitoids have $\varepsilon_{Nd(T)}$ values greater than -5, in contrast to values below -5 for most CIZ samples (Figure 21).

Figures 22 and 23 present graphical comparisons of the ε_{Nd} values and initial Sr ratios, and $\delta^{18}O$ values and initial Sr ratios, respectively. Although there is overlap in the data sets, the overall distribution of data in the two suites are clearly distinct. The range in initial Sr ratios for the CIZ granitoids is far greater than for the subduction-related batholiths, and both initial Sr ratios and ε_{Nd} values are distinctly more evolved than their subduction counterparts.

The evidence presented above shows that the CIZ granitoids are distinct from granitoids formed in subduction settings. More specifically, a large mantle contribution to subduction-zone magmatism is easily recognized even in cases such as the CVZ where subduction takes place beneath thick continental crust. In contrast, the data for the

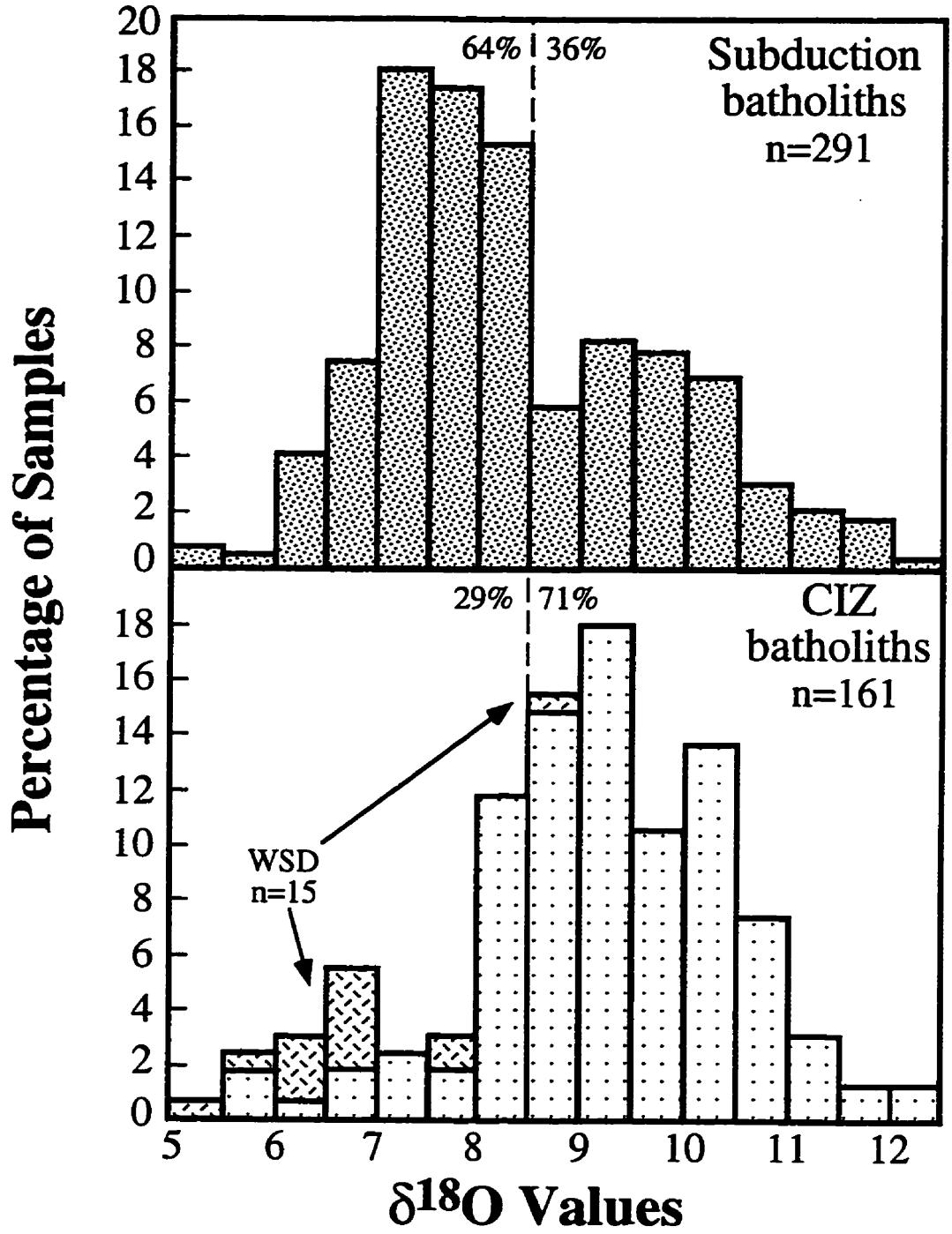

Figure 19. Comparison of $\delta^{18}O$ values for subduction and CIZ batholiths, with percentages above and below 8.5‰ (excluding WSD). Subduction= SNB (Masi *et al.*, 1981; Pickett & Saleeby, 1994); PRB (Taylor & Silver, 1978); CPC (Magaritz & Taylor, 1976); CRB (Masi *et al.*, 1981); CVZ (James, 1982; Longstaffe *et al.*, 1983; Harmon *et al.*, 1984); THB (Debon *et al.*, 1985). CIZ= CB (this study); SP (Driver *et al.*, in prep); SEBCB (Brandon & Lambert, 1993; 1994); IB (Criss & Fleck, 1987; (including WSD) Fleck, 1990).

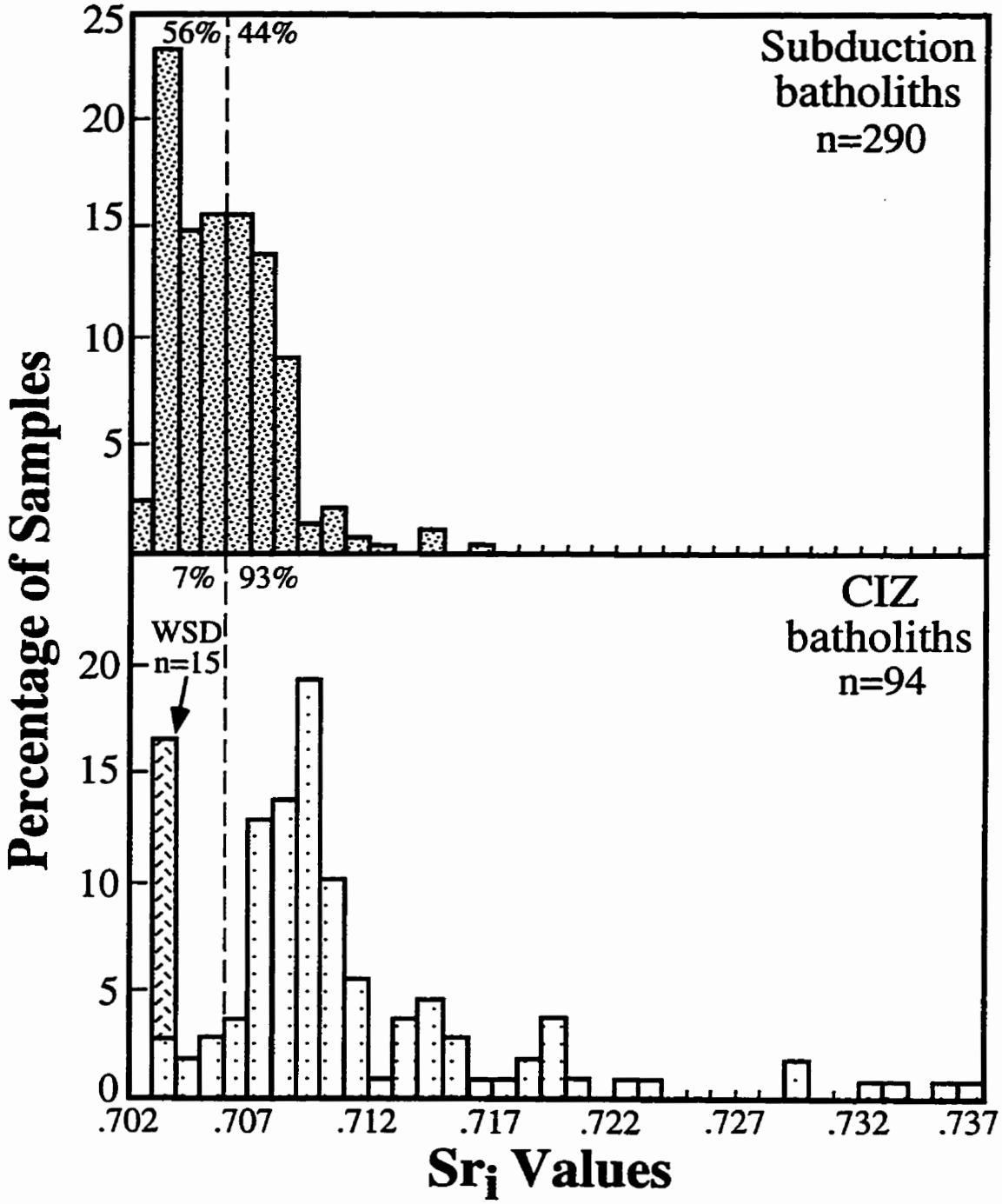

Figure 20. Comparison of Sr_i values for subduction and CIZ batholiths, with percentages above and below 0.706 (excluding WSD). Subduction= CPC (Cui & Russell, 1995b; Friedman *et al.*, 1995: Barker *et al.*, 1986; Magaritz & Taylor, 1976); SNB (Sawka *et al.*, 1990; Pickett & Saleeby, 1994; Chen & Tilton, 1991; Masi *et al.*, 1981); PRB (Taylor & Silver, 1978); CRB (Masi *et al.*, 1981); CVZ (James, 1982; Longstaffe *et al.*, 1983; Harmon *et al.*, 1984); THB (Crawford & Searle, 1992; Debon *et al.*, 1985). CIZ= CB (this study); SEBCB (Brandon & Lambert, 1993; 1994); SP (Driver, *et al.*, in prep); IB (including WSD) (Criss & Fleck, 1987; (including WSD) Fleck, 1990).

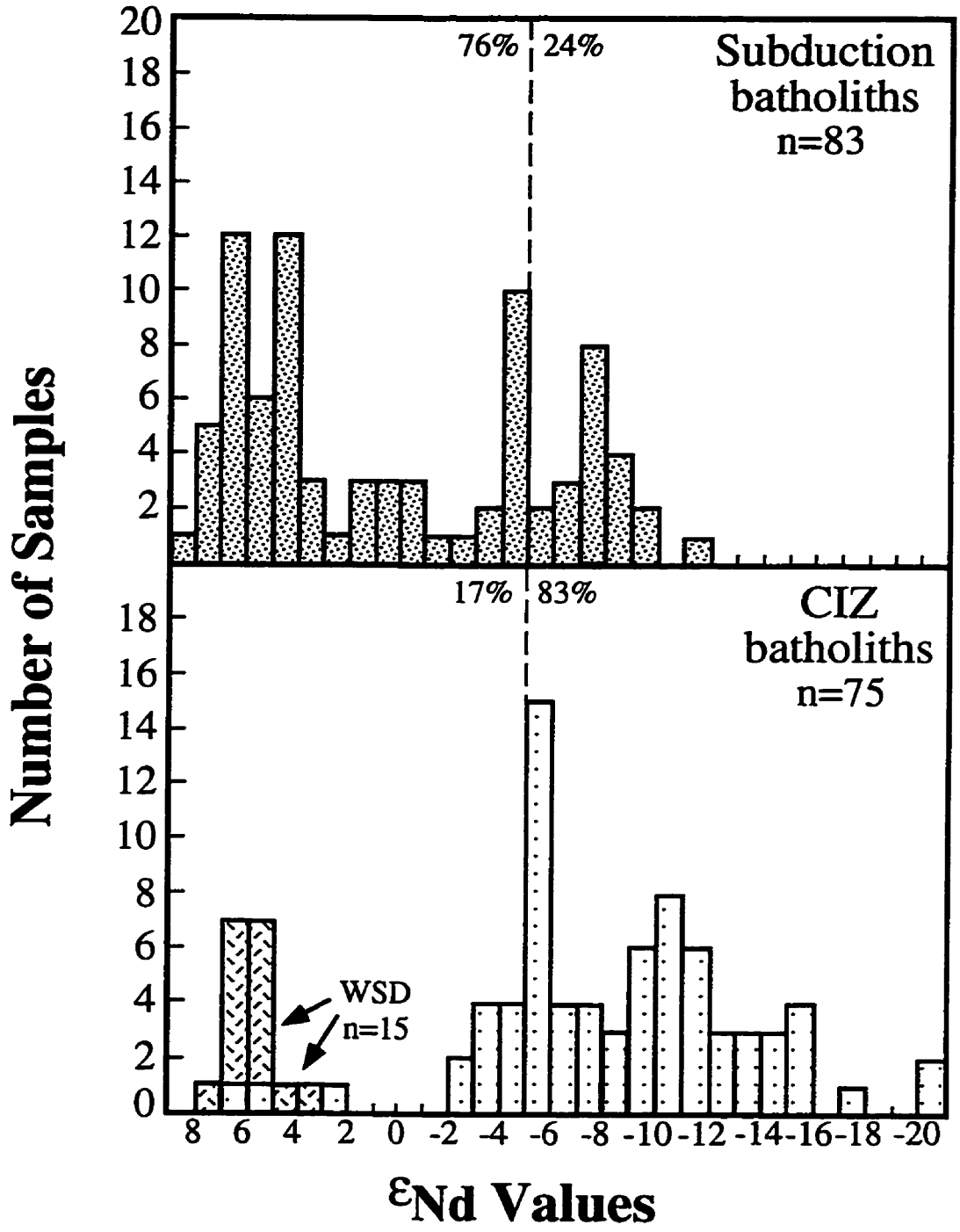

Figure 21. Comparison of ε_{Nd} values for subduction and CIZ batholiths, with percentages above and below -5 (excluding WSD). Subduction= CPC (Cui & Russell, 1995b; Friedman *et al.*, 1995); SNB (Sawka *et al.*, 1990; Pickett & Saleeby, 1994); CVZ (James, 1982); THB (Crawford & Searle, 1992). CIZ= CB (this study); SP (Driver, *et al.*, in prep); SEBCB (Brandon & Lambert, 1993; 1994); IB (including WSD) (Fleck, 1990).

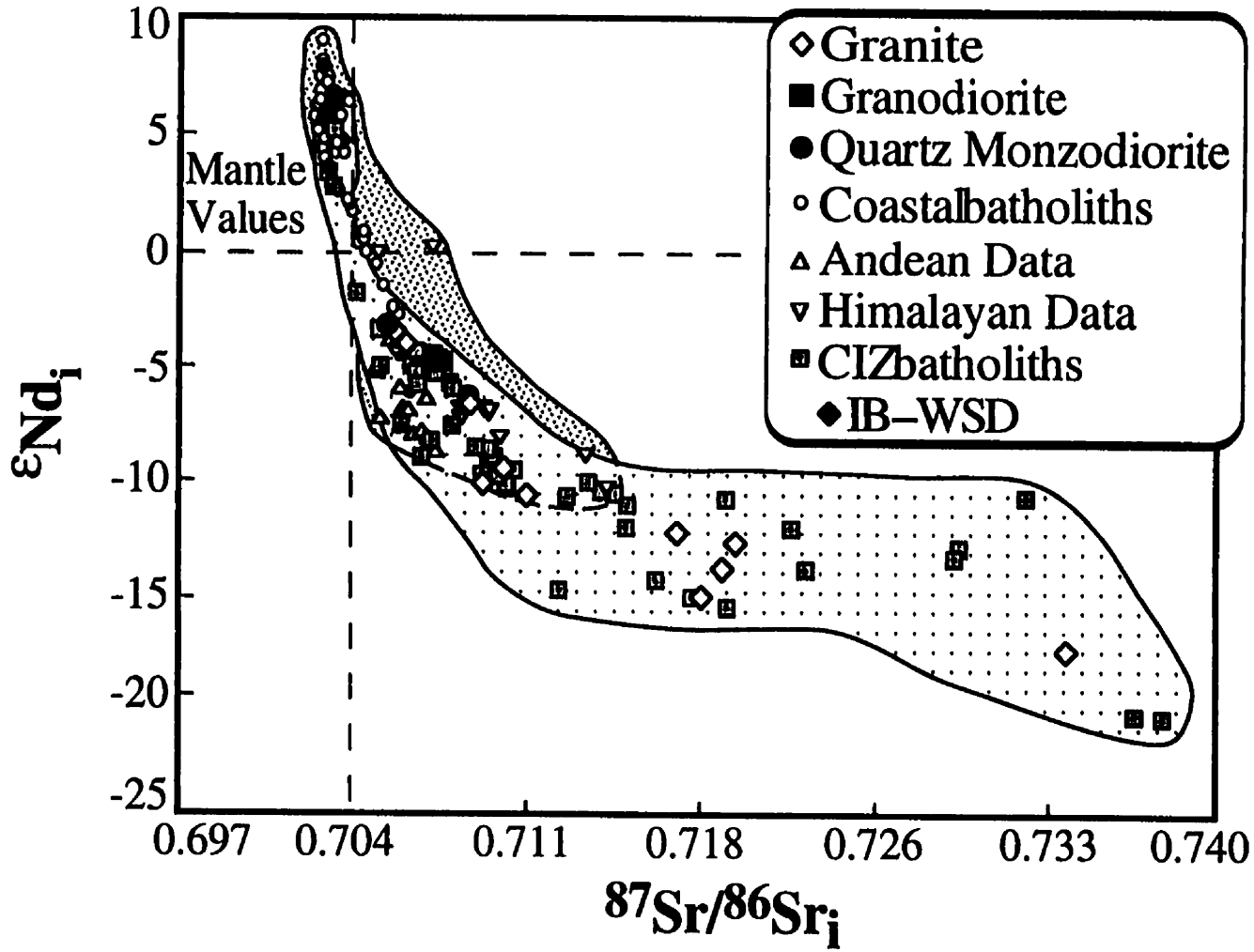

Figure 22. ε_{Nd} vs. inital $^{87}Sr/^{86}Sr$ ratios for subdustion and CIZ batholiths. Subduction= CPC (Cui & Russell, 1995b; Friedman *et al.*, 1995); SNB (Sawka *et al.*, 1990; Pickett & Saleeby, 1994); CVZ (James, 1982; Longstaffe *et al.*, 1983); THB (Crawford & Searle, 1992). CIZ= CB (this study); SP (Driver *et al.*, in prep); SEBCB (Brandon & Lambert, 1993; 1994); IB (Fleck, 1990).

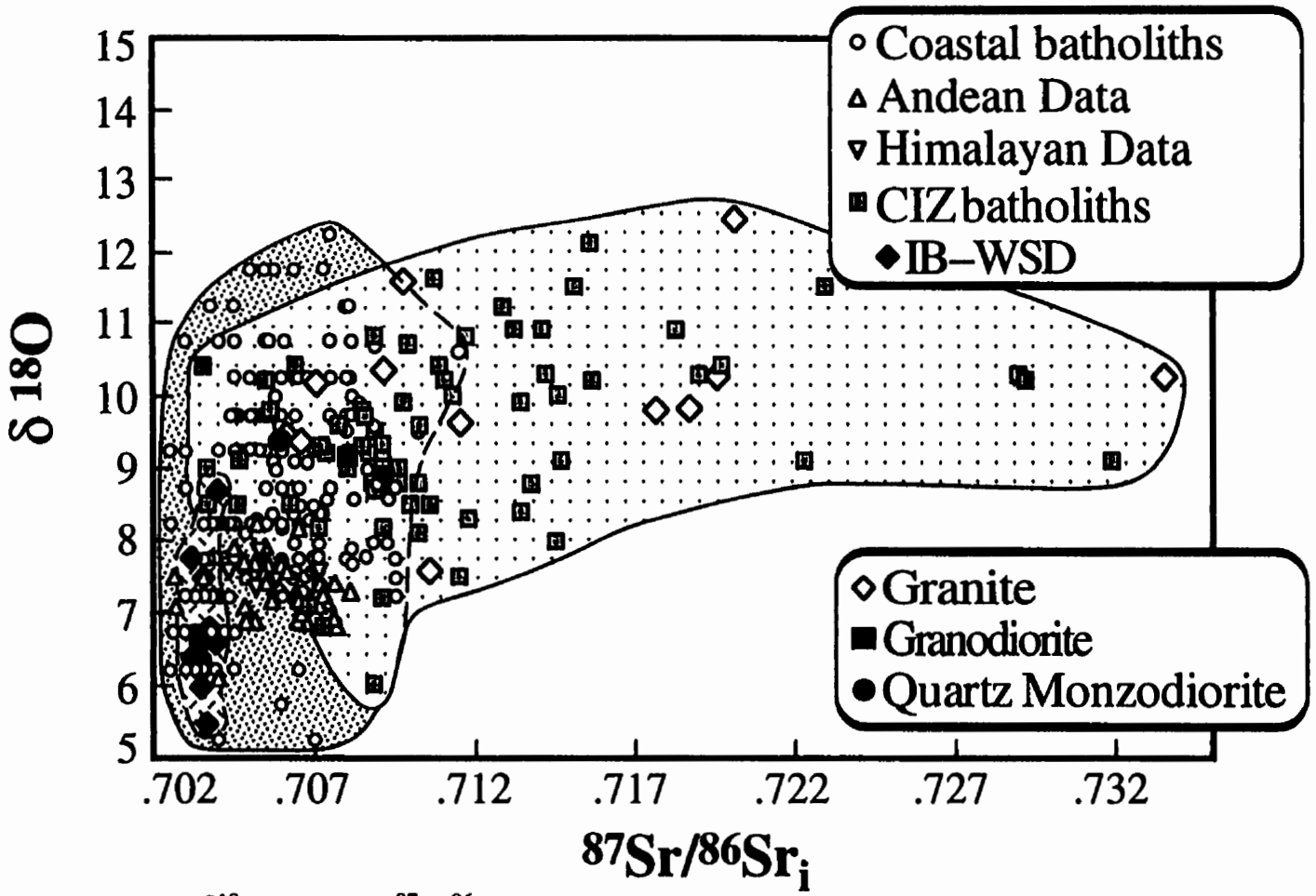

Figure 23. $\delta^{18}O$ vs. initial $^{87}Sr/^{86}Sr$ ratios for subduction and CIZ batholiths. Subduction= SNB (Pickett & Saleeby, 1994; Masi *et al.*, 1981); CRB (Masi *et al.*, 1981) PRB (Taylor & Silver, 1978) CVZ (James, 1982; Longstaffe *et al.*, 1983; Harmon *et al.*, 1984); THB (Debon *et al.*, 1985; Crawford & Searle, 1992). CIZ= CB (this study); SP (Driver *et al.*, in prep); SEBCB (Brandon & Lambert, 1994); IB (Fleck & Criss, 1987; Fleck, 1990).

CIZ granitoids can be explained with little or no mantle contribution. These observations strongly suggest that the CIZ magmas were not generated in a subduction setting.

Proposed Tectonic Model

Figure 24 depicts the tectonic setting of the Canadian Cordillera in mid-Cretaceous time, according to Souther (1991). His model is consistent with our findings for the Cassiar Batholith. Continuing subduction of oceanic crust beneath the western margin of the continent gives rise to magmatism in the Coast Plutonic Complex, and further south, magmatism in the Sierra Nevada and Peninsular Ranges batholiths. Approximately 400 km inland, thrusting of rocks of the Intermontane Belt over cratonic North America has produced a large crustal welt which is the Omineca Crystalline Belt. The timing of thrusting in these belts is constrained by geological and geochronological evidence. The beginning of thrusting is bracketed by the occurrence of Upper Triassic fossils in mylonite clasts, and by Middle to Late Jurassic plutons which cut some of the thrust faults in the Intermontane Belt (Templeman-Kluit, 1979; Gabrielse and Yorath, 1992). Thrusting persisted into the Early Cretaceous as evidenced by the thrusting of syn-orogenic clastic rocks over Lower Cretaceous strata (Templeman-Kluit, 1979). Thus, the documented end of thrusting preceded mid-Cretaceous magmatism of the Cassiar and SEBC batholiths by approximately 25-30 Ma.

The timing of thrusting relative to the age of magmatism is important for understanding the thermal evolution of thickened crust and, in turn, the genesis of the CIZ magmas. Patiño Douce *et al.* (1990) numerically modeled the effect of thrusting and associated crustal thickening on geothermal gradients in the crust. Their models, which were designed specifically for the Cordilleran Interior, assumed normal conductive mantle heat input to the base of the crust, and the presence in the middle crust of a 10 km thick layer rich in heat-producing elements. This high heat-producing layer simulates the

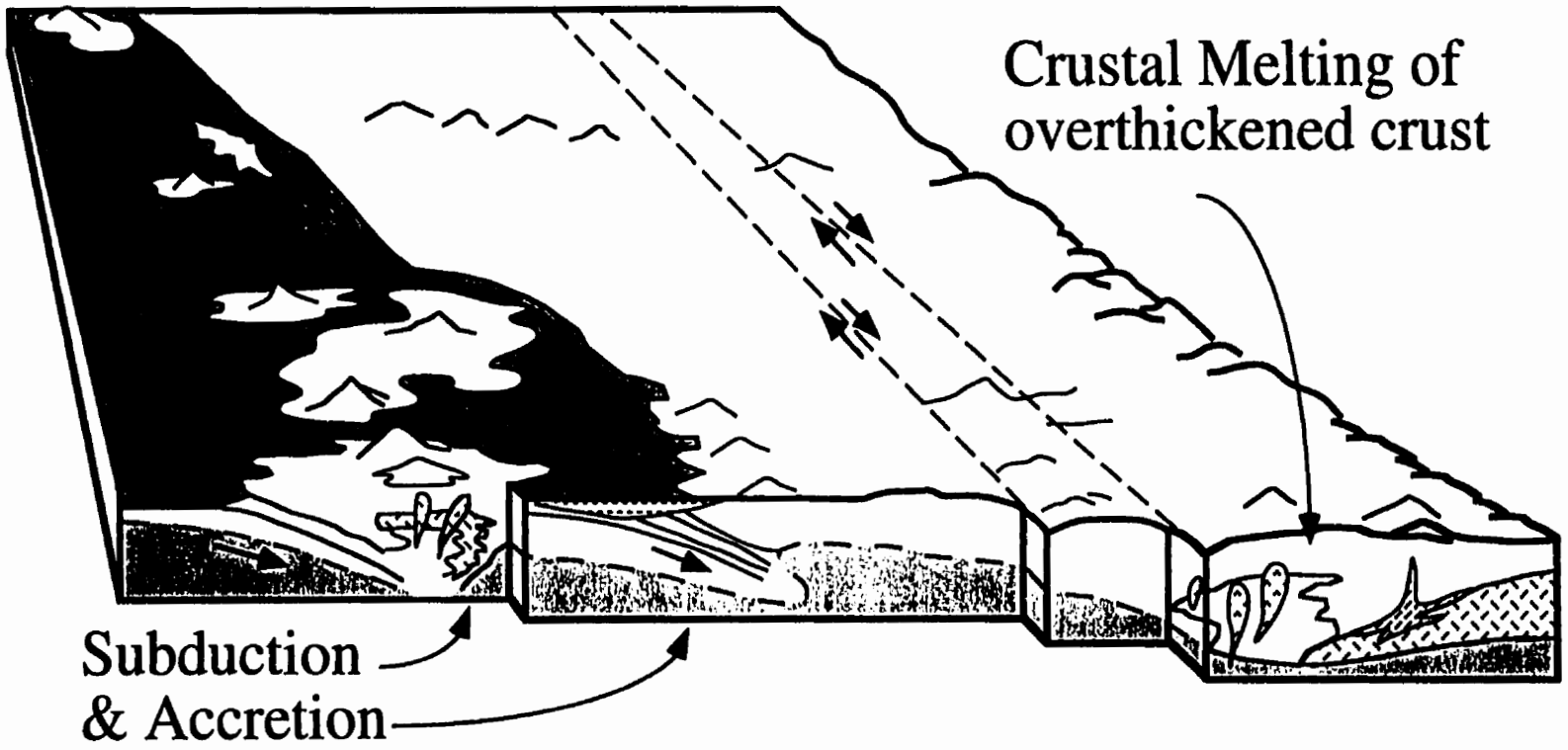

Figure 24. Tectonic model for the North American Cordillera in the mid-Cretaceous (ca. 100 Ma): Subduction is occurring along the coast of North America, generating subduction-style magmatism, such as the Coast Plutonic Complex, the Coast Ranges batholith, the Sierra Nevada batholith, and the Peninsular Ranges batholith. However, the CIZ is experiencing compression and overthickening at this time. Crustal melting is generated within the CIZ, creating intra-crustal magmatism, such as the Cassiar Batholith, the southeast B.C. batholiths (SEBCB), the Spirit pluton, and the Idaho batholith. Diagram modified from Souther (1991).

Proterozoic metasedimentary rocks of the miogeocline. Their modeling shows that, if the crust is thickened by 50% or more, the metasedimentary layer will become hot enough to produce granitic magmas that are capable of rising into the upper crust. The modeling also indicates that temperatures at the base of the thickened crust will be high enough to generate granitic magmas from tonalitic to basaltic composition source rocks (e.g., Rushmer, 1991; Skjerlie and Johnston, 1993). Finally, the modeling predicts that the main phase of magmatism will begin 5 to 25 Ma after the cessation of thrusting. This prediction is broadly consistent with the relative timing of thrusting and magmatism observed in the Canadian segment of the CIZ.

The most important conclusion that can be drawn from the modeling of Patiño Douce *et al.* (1990) is that crustal thickening, by itself, is capable of producing mobile granitoid magmas from metasedimentary and metaigneous source rocks; no additional heat input from the mantle in the form underplated or intraplated mafic magmas is required for this crustal melting. This finding obviates the need to invoke a subduction-induced thermal regime to explain CIZ magmatism (cf. Miller and Barton, 1990). It is also consistent with absence of any mafic magmatism associated with either the Cassiar or SEBC batholiths.

In this context, the Idaho batholith is somewhat distinct from the northern CIZ batholiths, differing in two ways. Firstly, age dates (K-Ar, Rb-Sr, U-Pb) on the Idaho batholith suggest that it is mostly Late Cretaceous to Eocene in age (Bickford *et al.*, 1981; Armstrong, 1975; 1976), 35-65 Ma younger than the Cassiar and SEBC batholiths. Secondly, a mafic component is present within the Idaho batholith, manifesting itself as mafic dykes within the Bitterroot lobe, and as minor tonalite and quartz diorite units found peripheral to the main phases of the batholith (Hyndman and Foster, 1988; Lewis *et al.*, 1987). Hyndman and Foster (1988) suggested that this mafic magmatism may be related to subduction occurring west of the batholith, the proposed

subduction zone being located in areas now occupied by the Miocene Columbia River Basalts. I suggest, however, that these mafic magmas were generated in an extensional setting. Widespread mafic and felsic magmatism associated with Eocene extension has, in fact, been documented in the nearby Ladybird Suite granitoids of southeastern British Columbia, and in the Colville Igneous Complex of northeastern Washington (Carr, 1992; Morris and Hooper, 1997). Thus, the similarity between the Idaho batholith and the northern CIZ intrusions may not be the result of a common tectonic setting, but of common crustal source materials, namely the Proterozoic basement and cover rocks of the North American miogeocline.

SUMMARY AND CONCLUSIONS

A detailed study of the Cretaceous Cassiar Batholith revealed the following:

(1) The rocks of the Cassiar Batholith are high in K, and range from biotite-muscovite granite and biotite ± muscovite granodiorite, to subordinate biotite ± hornblende granodiorite, quartz monzodiorite, quartz monzonite, and quartz syenite.

(2) Major- and trace-element geochemistry is useful for classifying the rocks of the batholith, but petrologic interpretations from these data alone are equivocal.

(3) The combination of stable and radiogenic isotopes provides the best indication of the source material of the Cassiar Batholith. These data indicate the batholith was derived from two crustal sources: (1) an isotopically juvenile, mafic crustal source, and (2) an isotopically evolved, felsic crustal source.

(4) Both mafic and felsic source rocks with the appropriate isotopic compositions are present in the Paleoproterozoic basement and Meso- to Neo-proterozoic supracrustal cover of the western North American miogeocline.

(5) The Cassiar Batholith is lithologically and isotopically similar to the other intrusions in the CIZ, including the southeast British Columbia batholiths, the Spirit pluton in northeastern Washington, and the Idaho batholith.

(6) The CIZ intrusions as a whole are distinct from granitoids formed in subduction settings around the globe. Notable differences include generally higher SiO_2 contents (>65 wt. %) and $\delta^{18}O$ values (>8.5), and a wide range but overall higher initial Sr ratios (>0.706) and lower ε_{Nd} values (<-5).

(7) The similarities seen in the CIZ granitoids can be linked to intra-crustal melting of Proterozoic basement and supracrustal rocks. Crustal thickening, followed by extension, provided the heat needed to generate these intra-crustal melts.

LITERATURE CITED

Armstrong, R.L. 1975. The geochronometery of Idaho (part I). Isochron/West 14, 1-50.

Armstrong, R.L. 1976. The geochronometery of Idaho (part II). Isochron/West 15, 1-33.

Armstrong, R.L. 1988. Mesozoic and early Cenozoic magmatic evolution of the Canadian Cordillera. Geological Society of America Special Paper 218, 55-91.

Armstrong, R.L., Taubeneck, W.H. and Hales, P.O. 1977. Rb-Sr and K-Ar geochronometry of Mesozoic granitic rocks and their Sr isotopic composition, Oregon, Washington, and Idaho. Geological Society of America Bulletin 88, 397-411.

Baadsgaard, H., Folinsbee, R.E., and Lipson, J. 1961. Potassium–argon dates of biotites from Cordilleran granites. Geological Society of America Bulletin, 72, 689-702.

Barker, F., Arth, J.G., and Stern, T.W. 1986. Evolution of the Coast batholith along the Skagway Traverse, Alaska and British Columbia. American Mineralogist, 71, 632-643.

Bickford, M.E., Chase, R.B., Nelson, B.K., Schuster, R.D., and Arruda, E.C. 1981. U-Pb studies of zircon cores and overgrowths, and monazite: implications for age and petrogenesis of the northeastern Idaho batholith. Journal of Geology, 89, 433-457.

Boghossian, N.D., Patchett, P.J., Ross, G.M., and Gehrels, G.E. 1996. Nd isotopes and the source of sediments in the miogeocline of the Canadian Cordillera. The Journal of Geology, 104, 259-277.

Boynton, W.V. 1984. Cosmochemistry of the rare earth elements: Meteorite studies, 67-114, *in:* P. Henderson, (ed.), Rare earth element geochemistry. Elsevier, New York, 510p.

Brandon, A.D. and Lambert, R.StJ. 1993. Geochemical characterization of mid-Cretaceous granitoids of the Kootenay Arc in the southern Canadian Cordillera. Canadian Journal of Earth Sciences, 30, 1076-1090.

Brandon, A.D. and Lambert, R.StJ. 1994. Crustal melting in the Cordilleran Interior: The mid-Cretaceous White Creek batholith in the southern Canadian Cordillera. Journal of Petrology, 35(1), 239-269.

Brandon, A.D. and Smith, A.D. 1994. Mesozoic granitoid magmatism in southeast British Columbia: Implications for the origin of granitoid belts in the North American Cordillera. Journal of Geophysical Research, 99(B6), 11879-11896.

Burwash, R.A. and Wagner, P.A. 1988. Sm/Nd geochronology of the Moyie Intrusions, Moyie Lake Map Area, British Columbia (82G/5). British Columbia Ministry of Energy, Mines and Petroleum Resources, Geological Fieldwork, Paper 1989-1.

Carr, S.D. 1992. Tectonic setting and U-Pb geochronology of the early Tertiary Ladybird leucogranite suite, Thor-Oden Pinnacles area, southern Omineca Belt, British Columbia. Tectonics, 11, 258-278.

Chen, J.H. and Tilton, G.R. 1991. Applications of lead and strontium isotopic relationships to the petrogenesis of granitoid rocks, central Sierra Nevada batholith. Geological Society of America Bulletin, 103, 439-447.

Clarke, D.B. 1992. Granitoid Rocks. Chapman and Hall, London, 283p.

Clayton, R.N. and Mayeda, T.K. 1963. The use of bromine pentafluoride in the extraction of oxygen from oxides and silicates for isotope analysis. Geochimica et Cosmochimica Acta, 27, 43-52.

Coleman, D.S., Frost, T.P., and Glazner, A.F. 1992. Evidence from the Lamarck Granodiorite for rapid late Cretaceous crust formation in California. Science, 258, 1924-1926.

Coney, P.J. 1989. Structural aspects of suspect terranes and accretionary tectonics in western North America. Journal of Structural Geology, 11(1/2), 107-125.

Crawford, M.B. and Searle, M.P. 1992. Field relationships and geochemistry of pre-collisional (India-Asia) granitoid magmatism in the central Karakoram, northern Pakistan. Tectonophysics, 206, 171-192.

Creaser, R.A., Erdmer, P., Stevens, R.A., and Grant, S.L. 1997. Tectonic affinity of Nisutlin and Anvil assemblage strata from the Teslin tectonic zone, northern Canadian Cordillera: Constraints from neodymium isotope and geochemical evidence. Tectonophysics, 16(1) 107-121.

Criss, R.E. and Fleck, R.J. 1987. Petrogenesis, geochronology, and hydrothermal systems in the northern Idaho batholith and adjacent areas based on $^{18}O/^{16}O$, D/H, $^{87}Sr/^{86}Sr$, K-Ar, and $^{40}Ar/^{39}Ar$ studies. U.S. Geological Survey Professional Paper 1436, Chapter 6.

Cross, W., Iddings, J.P., Pirsson, L.V. and Washington, H.S. 1903. Quantitative classification of igneous rocks. University of Chicago Press, 286p.

Cui, Y. and Russell, J.K. 1995a. Magmatic origins of calc-alkaline intrusions from the Coast Plutonic Complex, southwestern British Columbia. Canadian Journal of Earth Sciences, 32, 1643-1667.

Cui, Y. and Russell, J.K. 1995b. Nd-Sr-Pb isotopic studies of the southern Coast Plutonic Complex, southwestern British Columbia. Geological Society of America Bulletin, 107(2), 127-138.

Cumming, G.L. and Krstic, D. 1991. Geochronology at the Namew Lake Cu-Ni deposit, Flin Flon area, Manitoba, Canada: A Pb-Pb study of whole rocks and ore minerals. Canadian Journal of Earth Sciences, 28, 1328-1339.

Debon, F., LeFort, P., Sheppard, S.M.F., and Sonet, J. 1985. Transhimalaya-Himalaya: A chemical, mineralogical, isotopic, and chronological synthesis along a Tibet-Nepal section. Journal of Petrology, 27, 219-250.

DePaolo, D.J., Perry, F.V., and Baldridge, W.S. 1992. Crustal versus mantle sources of granitic magmas: A two-parameter model based on Nd isotopic studies. Transactions of the Royal Society of Edinburgh: Earth Sciences, 83, 4339-446, *in:* P.E. Brown and B.W. Chappell, (eds.), Second Hutton Symposium of the Origin of Granites and Related Rocks. Geological Society of America Special Paper 272, 507p.

Devlin, W.J., Brueckner, H.K., and Bond, G.C. 1988. New isotopic data and a preliminary age for volcanics near the base of the Windermere Supergroup, northeastern Washington, USA. Canadian Journal of Earth Sciences, 25(11), 1906-1911.

Driver, L.A. 1995. Major and trace element geochemistry of the Cretaceous Spirit pluton, northeastern Washington, USA. The Compass, 71(4), 126-146.

Driver, L.A., Larson, P.B., and Hawkesworth, C.J. In prep. O, Sr, and Nd isotope signatures in the mid-Cretaceous Spirit pluton, northeast Washington, USA.

Fleck, R.J. 1990. Neodymium, strontium and trace-element evidence of crustal anatexis and magma mixing in the Idaho batholith, 359-373, *in:* J.L. Anderson, (ed.), The nature and origin of Cordilleran magmatism. Geological Society of America Memoir 174.

Fleck, R.J. and Criss, R.E. 1985. Strontium an oxygen isotopic variations in Mesozoic and Tertiary plutons of Central Idaho. Contributions to Mineralogy and Petrology, 2/3, 291-308.

Friedman, R.M., Mahoney, J.B., and Cui, Y. 1995. Magmatic evolution of the southern Coast Belt: Constraints from Nd-Sr isotopic systematics and geochronology of the southern Coast Plutonic Complex. Canadian Journal of Earth Sciences, 32, 1681-1698.

Gabrielse, H. 1962a. Cry Lake Map No. 29-1962, 1:250,000, sheet 104I. Geological Survey of Canada.

Gabrielse, H. 1962b. Kechika Map No. 42-1962, 1:250,000, sheet 94L. Geological Survey of Canada.

Gabrielse, H. 1963. McDame Map No. 1110A, 1:250,000. Geological Survey of Canada Memoir 319.

Gabrielse, H. 1969. Jennings River Map No. 18-1968, 1:250,000, sheet 104O. Geological Survey of Canada.

Gabrielse, H. and Reesor, J.E. 1974. The nature and setting of granitic plutons in the central and eastern parts of the Canadian Cordillera. Pacific Geology, 8, 109-138.

Gabrielse, H. and Yorath, C.J. (eds.). 1991. Geology of the Cordilleran orogen in Canada. Geological Survey of Canada, Geology of Canada, 4, 844p.

Garzione, C.N., Patchett, P.J., Ross, G.M., and Nelson, J.-A. 1997. Provenance of sedimentary rocks in the Canadian Cordilleran miogeocline: A Nd isotope study. Canadian Journal of Earth Sciences, 34(12), 1603-1618.

Ghosh, D.K. and Lambert, R.St.J. 1989. Nd-Sr isotopic study of Proterozoic to Triassic sediments from southeastern British Columbia. Earth and Planetary Science Letters, 94, 29-44.

Goldstein, S.L., O'Nion, R.K., and Hamilton, P.J. 1984. A Sm-Nd isotope study of atmospheric dusts and particulates from major river systems. Earth and Planetary Science Letters, 70(2), 221-236.

Gromet, L.P. and Silver, L.T. 1987. REE variations across the Peninsular Ranges batholith: Implications for batholithic petrogenesis and crustal growth in magmatic arcs. Journal of Petrology, 28, 75-125.

Hamilton, W. 1988. Mesozoic tectonics of southeastern California and southwestern Arizona. Geological Society of America Abstracts with Programs, 20, 165.

Harker, A. 1909. The Natural History of Igneous Rocks. Macmillan, New York, 384p.

Harmon, R.S., Barreiro, B.A., Moorbath, S., Hoefs, J., Francis, P.W., Thorpe, R.S., Deruelle, B., McHugh, J., and Viglino, J.A. 1984. Regional O-, Sr-, and Pb-isotope relationships in late Cenozoic calc-alkaline lava of the Andean Cordillera. Geological Society of London, 141, 803-822.

Holdaway, M.J. 1971. Stability of andalusite and the aluminium silicate phase diagrams. American Journal of Science, 271, 97-131.

Holmden, C., Creaser, R.A., Muehlenbachs, K., Bergstrom, S.M., and Leslie, S.A. 1996. Isotopic and elemental systematics of Sr and Nd in 454 Ma biogenic apatites: Implications for paleoseawater studies. Earth and Planetary Science Letters, 142, 425-437.

Hyndman, D.W. 1983. The Idaho batholith and associated plutons, Idaho and western Montana, 213-240, *in:* J.A. Roddick (ed.), Circum-Pacific plutonic terranes. Geological Society of America Memoir 159.

Hyndman, D.W. 1984. A petrographic and chemical section through the northern Idaho batholith. Journal of Geology, 92, 83-102.

Hyndman D.W. and Foster, D.A. 1988. The role of tonalites and mafic dikes in the generation of the Idaho batholith. Journal of Geology, 96, 31-46.

Høy, T. 1989. The age, chemistry and tectonic setting of the middle Proterozoic Moyie Sills, Purcell Supergroup, southeastern B.C. Canadian Journal of Earth Sciences, 26(11), 2305-2317.

James, D.E. 1982. A combined O, Sr, Nd, and Pb isotopic and trace element study of crustal contamination in central Andean lavas, I; local geochemical variations. Earth and Planetary Science Letters, 57, 47-62.

Johnson, D.M., Hooper, P.R. and Conrey, R.M. 1998. XRF analysis of rocks and minerals for major and trace elements on a single low dilution Li-tetraborate fused bead. Advances in X-ray Analysis, 41, in press.

Kay, R. W., Mahlburg Kay, S., and Arculus, R.J. 1992. Chapter 11: Magma genesis and crustal processing, 423-445, *in:* D.M. Fountain, R. Arculus, and R.W. Kay (eds.), Continental Lower Crust, Elsevier, Amsterdam, 485p.

Keith, S. B. 1978. Paleosubduction geometries inferred from Cretaceous and Tertiary magmatic patterns in southwestern North America. Geology, 6, 516-521.

Kistler, R.W. and Peterman, Z.E. 1973. Variations in Sr, Rb, K, Na, and initial $^{87}Sr/^{86}Sr$ in Mesozoic granitic rocks and intruded wall rocks in central California. Geological Society of America Bulletin 84, 3489-3512.

Kistler, R.W. and Peterman, Z.E. 1978. Reconstruction of crustal blocks of California on the basis of initial strontium isotopic compositions of Mesozoic granitic rocks. US Geologial Survey Professional Paper 1071, v17.

Knaack C. S., Cornelius, S., and Hooper, P. R. 1994. Trace element analyses of rocks and minerals by ICP-MS. Washington State University, Geology Department, Open File Report 4p.

Lambert, R.StJ. and Chamberlain, V.E. 1990. Isotopic studies on Mesozoic and Tertiary granitoids and their Precambrian basement, B.C., Washington, and Idaho. Proceedings of the 1990 Lithoprobe Cordilleran Workshop, University of Calgary, Alberta, 91-98.

Lewis, R.S., Kiilsgaard, T.H., Bennett, E.H., and Hall, W.E. 1987. Lithologic and chemical characteristics of the central and southeastern part of the southern lobe of the Idaho batholith, 171-196, *in:* T.L. Vallier and H.C. Brooks (eds.), Geology of the Blue Mountains region of Oregon, Idaho and Washington; the Idaho batholith and its border zone. U.S. Geological Survey Professional Paper 1436.

Lipman P.W., Prostka, H.J., and Christiansen, R.I. 1972. Cenozoic volcanism and plate tectonic evolution of the western United States; 1, Early and middle Cenozoic, 217-248, *in:* A discussion on volcanism and the structure of the Earth. Philosophical Transactions of the Royal Society of London, series A, 271.

Longstaffe, F.J., Clark, A.H., McNutt, R.H., and Zentilli, M. 1983. Oxygen isotopic compositions of Central Andean plutonic and volcanic rocks, latitudes 26°-29° south. Earth and Planetary Science Letters, 64, 9-18.

Lugmair, G.W. and Galer, S.J.G. 1992. Age and isotope relationships among the angrites Lewis Cliff 86010 and Angra dos Reis. Geochimica et Cosmochimica Acta, 56, 1673-1694.

Magaritz, M. and Taylor, H.P., Jr. 1976. $^{18}O/^{16}O$ and D/H studies along a 500 km traverse across the Coast Range batholith and its country rocks, central British Columbia. Canadian Journal of Earth Sciences, 13, 1514-1536.

Manduca, C.A., Kuntz, M.A., and Silver, L.T. 1993. Emplacement and deformation history of the western margin of the Idaho batholith near McCall, Idaho: Influence of a major terrane boundary. Geological Society of America Bulletin, 105, 749-765.

Mansy, J.-L. 1986. Geologie de la chaîne d'Omineca de Rocheuses aux plateaux interieurs (Cordillére Canadienne) Evolution depuis le Précambrien. Société Géologique du Nord Publication n° 13, v1, 491p.

Masi, U., O'Neil, J.R., and Kistler, R.W. 1981. Stable isotope systematics in Mesozoic granites of central and northern California and southwestern Oregon. Contributions to Mineralogy and Petrology, 76, 116-126.

Mato, G., Ditson, G., and Godwin, C. 1983. Geology and geochronometry of tin mineralization associated with the Seagull Batholith, south-central Yukon Territory. CIM Bulletin, 76(854), 43-49.

Miller, C.F. and Barton, M.D. 1990. Phanerozoic plutonism in the Cordilleran Interior, U.S.A, 213-231, *in:* S.M. Kay and C.W. Rapela (eds.), Plutonism from Antarctica to Alaska. Geological Society of America Special Paper 241.

Monger, J.W.H. and Price, R.A. 1979. Geodynamic evolution of the Canadian Cordillera--progress and problems. Canadian Journal of Earth Sciences, 16(3), 770-791.

Monger, J.W.H., Price, R.A., and Tempelman-Kluit, D.J. 1982. Tectonic accretion and the origin of two metamorphic and plutonic welts in the Canadian Cordillera. Geology, 10, 70-75.

Morris, G.A. and Hooper, P.R. 1997. Petrogenesis of the Colville Igneous Complex, northeast Washington: Implications for Eocene tectonics in the northern U.S. Cordillera. Geology, 25(9), 831-834.

Narbonne, G.M. and Aitken, J.D. 1995. Neoproterozoic of the Mackenzie Mountains, northeastern Canada. Precambrian Research, 73(1-4), 101-121.

Nielsen, R.L. 1989. Phase equilibria constraints on liquid lines of descent generated by paired assimilation and fractional crystallization: Trace elements and Sr and Nd isotopes. Journal of Geophysical Research, 94, 787-794.

Panteleyev, A. 1985. Cassiar map-area (104 P/4, 5), 189-190, *in:* Geology in British Columbia 1977-1981. British Columbia Ministry of Energy, Mines and Petroleum Resources.

Patiño Douce, A.E. and Johnston, A.D. 1991. Phase equilibria and melt productivity in the pelitic system: implications for the origin of peraluminous granitoids and aluminous granulites. Contributions to Mineralogy and Petrology, 107, 202-218.

Patiño Douce, A.E., Humphreys, E.D., and Johnston, A.D. 1990. Anatexis and metamorphism in tectonically thickened continental crust exemplified by the Sevier hinterland, western North America. Earth and Planetary Science Letters, 97, 290-315.

Peacock, M.A. 1931. Classification of Igneous Rocks. Journal of Geology, 39, 54-67.

Pearce, J.A. 1983. Role of the sub-continental lithosphere in magma genesis at active continental margins, 230-249, *in:* C.J. Hawkesworth, and M.J. Norry, (eds.), Continental Basalts and Mantle Xenoliths. Shiva Publishing Limited, Cheshire UK. 272p.

Pearce, J.A., Harris, N.B.W., and Tindle, A.G. 1984. Trace element discrimination diagrams for the tectonic interpretation of granitic rocks. Journal of Petrology, 25(4), 956-983.

Pickett, D.A. and Saleeby, J.B. 1994. Nd, Sr, and Pb isotopic characteristics of Cretaceous intrusive rocks from deep levels of the Sierra Nevada batholith, Tehachapi Mountains, California. Contributions to Mineralogy and Petrology, 118, 198-215.

Pitcher, W.S. 1982. Granite type and tectonic environment, 19-40, *in:* K.J. Hsü (ed.), Mountain Building Processes. Academic Press, London, 263p.

Pitcher, W.S., Atherton, M.P., Cobbing, E.J., and Beckingsale, R.D. (eds.) 1985. Magmatism at a plate margin. Blackie and Sons, Ltd., Glasgow, Scotland, 435p.

Poole, W.H., Roddick, J.A., and Green, L.H. 1960. Wolf Lake Map No. 10-1960, 1:250,000, sheet 105B. Geological Survey of Canada.

Roddick, J.A. and Armstrong, J.E. 1959. Relict dikes in the Coast Mountains near Vancouver, B.C. Journal of Geology, 67(6), 603-613.

Rushmer, T. 1991. Partial melting of two amphibolites: Contrasting experimental results under fluid absent conditions. Contributions to Mineralogy and Petrology, 107(1), 41-59.

Sawka, W.N., Chappell, B.W., and Kistler, R.W. 1990. Granitoid compositional zoning by side-wall boundary layer differentiation: Evidence from the Palisade Crest Intrusive Suite, Central Sierra Nevada, California. Journal of Petrology, 31(3), 519-553.

Silver, L.T., Taylor, H.P., Jr. and Chappell, B.W. 1979. Some petrological geochemical and geochronological observations of the Peninsular Ranges batholith near the International border of the U.S.A. and Mexico, 83-110, *in:* P.L. Abbott and V.R. Todd (eds.), Mesozoic Crystalline Rocks, Geologic Society of America Annual Meeting Guidebook, 286p.

Skjerlie K.P. and Johnston, A.D. 1993. Vapor-absent melting at 10 kbar of a biotite- and amphibolite-bearing tonalite gneiss: Implications for the generation of A-type granites. Geology, 20, 263-266.

Souther, J.G. 1991. Volcanic Regimes, Chapter 14, 457-490, *in:* H. Gabrielse and C.J. Yorath (eds.), Geology of the Cordilleran Orogen in Canada. Geological Survey of Canada, Geology of Canada, 4, 844p.

Stacey, J.S. and Kramers, J.D. 1975. Approximation of terrestrial lead isotope evolution by a two-stage model. Earth and Planetary Science Letters, 26, 207-221.

Streckeisen, A.L. and LeMaitre, R.W. 1979. Chemical approximation to modal QAPF classification of the igneous rocks. Neues Jahrbuch der Mineralogie, Abhandlungen, 136, 169-206.

Taylor, H.P., Jr. 1986. Igneous Rocks: II. Isotope case studies of Circumpacific magmatism, Chapter 9, 273-317, *in:* Stable Isotopes in High Temperature Geological Processes: Reviews in Mineralogy, 16, Mineralogical Society of America, Washington D.C., 570p.

Taylor, H.P., Jr. and Sheppard, S.M.F. 1986. Igneous Rocks: I. Processes of isotopic fractionation and isotope systematics, Chapter 8, 227-271, *in:* Stable Isotopes in High Temperature Geological Processes: Reviews in Mineralogy, 16, Mineralogical Society of America, Washington D.C., 570p.

Templeman-Kluit, D.J. 1979. Transported cataclasite, ophiolite and granodiorite in Yukon: Evidence or arc-continent collision. Geological Survey of Canada Paper 79-14, 27p.

Todt, W., Cliff, R.A., Hanser, A., and Hofmann, P. 1996. Evaluation of a ^{202}Pb-^{205}Pb double spike for high-precision lead isotope analysis. Earth Processes: Reading the Isotopic Code, Geophysical Monograph 95, AGU, 429-437.

Toth, M. 1987. Petrology and origin of the Bitterroot Lobe of the Idaho batholith, 9-35, *in:* T.L. Vallier and H.C. Brooks (eds.), Geology of the Blue Mountains region of Oregon, Idaho and Washington; the Idaho batholith and its border zone. U.S. Geological Survey Professional Paper 1436.

Wanless R.K., Stevens, R.D., Lachance, G.R., and Delabio, R.N. 1978. Age determinations and geological studies, K-Ar isotopic ages, report 13. Geological Survey of Canada, Paper 78-72, 19p.

Wheeler J.O. and McFeely, P. (comp.). 1991. Tectonic assemblage map of the Canadian Cordillera and adjacent parts of the United States of America. Geological Survey of Canada, Map 1712A, scale 1:2,000,000.

Woodsworth, G.J., Anderson, R.G., and Armstrong, R.L. 1991. Plutonic Regimes, Chapter 15, 491-531, *in:* H. Gabrielse and C.J. Yorath (eds.), Geology of the Cordilleran Orogen in Canada, Geological Survey of Canada, Geology of Canada, 4, 844p.

Zartman, R.E. and Doe, B.R. 1981. Plumbotectonics--the model. Tectonophysics, 75, 135-162.

Appendix A

Sample locations for the Cassiar Batholith.

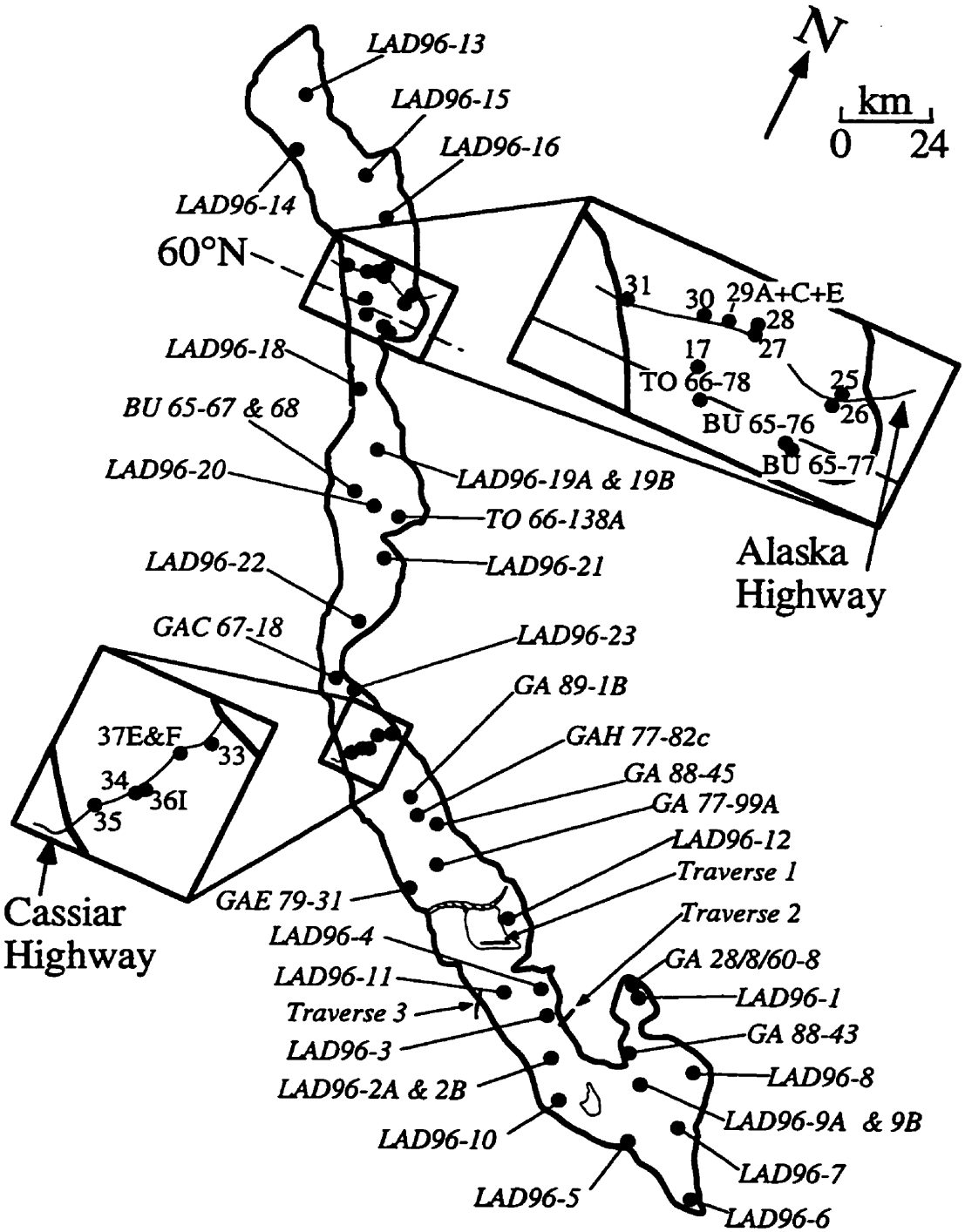

Appendix B

Cassiar Batholith sample locations

Sample	Rock Types	Latitude	Longitude
Cassiar Granitoids			
LAD96-1	BtMsGr	58°42'44"	128°11'15"
LAD96-2A	BtHblQmd	58°28'01"	128°23'56"
LAD96-2B	BtMsGr	58°28'01"	128°23'56"
LAD96-3	BtMsGr	58°32'15"	128°28'17"
LAD96-4	BtMsGr	58°37'12"	128°33'47"
LAD96-5	BtMsGr	58°22'47"	127°56'53"
LAD96-6	BtGr	58°18'25"	127°35'52"
LAD96-7	BtMsGr	58°26'27"	127°40'29"
LAD96-8	BtHblGd	58°34'17"	127°46'55"
LAD96-9B	BtQm	58°35'32"	127°57'13"
LAD96-10	BtGr	58°24'06"	128°18'05"
LAD96-11	BtHblGd	58°33'24"	128°42'46"
LAD96-12	BtHblGd	58°44'33"	128°50'21"
LAD96-13	BtMsGr	60°25'40"	131°20'31"
LAD96-14	BtMsGr	60°19'16"	131°16'22"
LAD96-15	BtGr	60°19'17"	130°55'53"
LAD96-16	BtMsGr	60°12'58"	130°44'46"
LAD96-17	BtMsGr	60°01'36"	130°40'59"
LAD96-18	BtMsGr	59°48'34"	130°32'09"
LAD96-19A	BtMsGr	59°41'24"	130°19'27"
LAD96-19B	BtHblGd	59°41'24"	130°19'27"
LAD96-20	BtMsGr	59°34'12"	130°13'22"
LAD96-21	BtMsGr	59°26'15"	130°05'10"
LAD96-22	BtMsGr	59°16'51"	130°02'42"
LAD96-23	BtMsGr	59°07'12"	129°53'38"
LAD96-25	BtMsGr	60°03'58"	130°29'13"
LAD96-26	BtGr	60°03'13"	130°29'57"
LAD96-27	BtMsGr	60°05'31"	130°40'56"
LAD96-28	BtMsGr	60°06'45"	130°41'00"
LAD96-29	many	60°05'34"	130°41'51"
LAD96-30	many	60°05'22"	130°43'42"
LAD96-31	many	60°04'36"	130°50'16"
LAD96-33	Grt	59°04'07"	129°43'39"
LAD96-34	many	59°00'45"	129°47'16"
LAD96-35	many	58°58'44"	129°50'27"

Appendix B

Cassiar Batholith sample locations

Sample	Rock Types	Latitude	Longitude
LAD96-36	many	59°00'54"	129°47'12"
LAD96-37	many	59°03'31"	129°45'04"
GA 77-99A	BtQmd	5848'	12916'
GA 89-1B	Grt	58°55'	129°31'
GA 88-43	BtMsGr	58°31'	128°05'
GA 88-45	BtHblQmd	58°54'	129°20'
GAE 79-31	BtMsGr	58°42'	129°20'
GAH 77-82C	BtGr	58°54'	129°27'
GAB 9/8/56-4	Grt	58°42'	129°12'
GA 28-8-60-8	BtGr	58°43'	128°14'
TO 66-78A	BtMsGr	59°57'	130°40'
TO 66-138A	BtHblGd	59°33'	130°08'
GAC 67-18	BtMsGr	59°08'	130°04'
BU 65-67	BtMsGr	59°34'	130°22'
BU 65-68	BtMsGr	59°34'	130°22'
BU 65-76	BtMsGr	59°58'	130°33'
BU 65-77	BtGd	59°58'	130°34'
Potential Source Material			
PE96-2B	Sch	58°34'	128°26'
PE96-3A	Hfl	58°34'	128°26'
RC-3A	QFG	58°32'	128°53'
GM96-C1C	Hfl	58°42'	128°53'
MDS	Sch	52°00'	118°30'
MDA	Amp	52°00'	118°30'
3VGS	Sch	50°52'	118°20'
3VGA	Amp	50°52'	118°20'

Appendix C

Major and selected trace element X-Ray Fluorescence Data

Sample	LAD96-1	LAD96-2A	LAD96-2B	LAD96-3	LAD96-4	LAD96-5	LAD96-6	LAD96-7
Rock Type	BtMsGr	BtHblQmd	BtMsGr	BtMsGr	BtMsGr	BtMsGr	BtGr	BtMsGr
Normalized Results (wt. %):								
SiO2	73.11	57.36	75.36	69.80	74.39	73.18	68.40	73.24
Al2O3	14.82	18.21	13.70	15.94	14.00	14.66	15.95	15.18
TiO2	0.24	1.26	0.10	0.37	0.29	0.26	0.48	0.23
FeO*	1.70	6.87	0.86	2.28	1.72	1.88	3.05	1.31
MnO	0.06	0.12	0.02	0.04	0.06	0.02	0.07	0.03
CaO	1.81	5.68	1.00	2.33	1.68	1.86	2.67	1.63
MgO	0.57	3.52	0.21	1.04	0.75	0.76	1.46	0.39
K2O	3.30	2.54	5.35	3.81	3.07	3.53	3.55	4.26
Na2O	4.29	3.79	3.28	4.17	3.89	3.66	4.08	3.61
P2O5	0.11	0.64	0.12	0.25	0.14	0.19	0.28	0.13
Trace Elements (ppm):								
Ni	8	7	7	8	7	7	8	7
Cr	4	20	0	9	6	3	11	0
Sc	7	15	5	8	7	6	11	3
V	19	171	5	34	36	42	62	16
Ba	985	1701	689	1202	802	1174	1535	1002
Rb	111	98	128	160	113	105	120	161
Sr	380	1076	247	480	307	519	593	317
Zr	109	257	72	162	114	124	161	122
Y	14	27	13	17	20	11	22	12
Nb	13.9	23.5	8.1	19.7	17.7	10.8	24.2	13.5
Ga	18	20	17	24	19	18	17	19
Cu	7	0	14	0	2	0	0	2
Zn	50	96	24	55	42	43	54	40
Pb	18	10	29	21	18	21	15	24
La	37	85	22	54	35	39	86	45
Ce	71	169	47	110	66	70	105	60
Th	11	17	9	30	12	6	24	16

Major elements are normalized on a volatile-free basis.

*Total Fe is expressed as FeO

"†" denotes values >120% of our highest standard

Appendix C

Major and selected trace element X-Ray Fluorescence Data

Sample	LAD96-8	LAD96-9B	LAD96-10	LAD96-11	LAD96-12	LAD96-13	LAD96-14
Rock Type	BtHblGd	BtQm	BtGr	BtHblGd	BtHblGd	BtMsGr	BtMsGr
Normalized Results (wt. %):							
SiO2	69.48	67.69	70.31	70.84	68.59	71.56	73.04
Al2O3	15.79	16.62	15.81	15.00	15.59	15.01	14.33
TiO2	0.40	0.42	0.32	0.41	0.56	0.41	0.28
FeO*	2.67	2.51	2.18	2.53	3.29	2.11	1.66
MnO	0.07	0.06	0.04	0.05	0.07	0.04	0.04
CaO	2.64	2.51	2.30	2.84	2.96	2.02	1.35
MgO	1.19	1.23	0.69	1.20	1.54	0.93	0.61
K2O	3.34	4.49	4.27	3.06	3.01	4.38	5.18
Na2O	4.19	4.25	3.88	3.83	4.11	3.33	3.28
P2O5	0.23	0.21	0.20	0.23	0.28	0.20	0.22
Trace Elements (ppm):							
Ni	9	10	8	7	10	8	6
Cr	10	9	3	11	15	12	1
Sc	9	8	3	6	3	2	1
V	43	45	33	54	61	47	22
Ba	1590	3398	1881	1386	1781	952	1339
Rb	121	100	129	84	87	205	178
Sr	599	710	523	612	606	279	393
Zr	148	147	154	159	202	154	150
Y	16	15	15	15	17	16	18
Nb	18.9	14.5	12.5	13.8	14.3	17.8	18.3
Ga	19	18	19	16	20	20	18
Cu	0	6	4	3	8	7	11
Zn	54	55	43	47	62	55	32
Pb	15	16	22	16	19	20	36
La	30	44	29	61	50	38	60
Ce	47	73	63	111	90	103	113
Th	7	10	8	20	16	21	28

Major elements are normalized on a volatile-free basis.

*Total Fe is expressed as FeO

"†" denotes values >120% of our highest standard

Appendix C

Major and selected trace element X-Ray Fluorescence Data

Sample	LAD96-15	LAD96-16	LAD96-17	LAD96-18	LAD96-19A	LAD96-19B	LAD96-20
Rock Type	BtGr	BtMsGr	BtMsGr	BtMsGr	BtMsGr	BtHblGd	BtMsGr
Normalized Results (wt. %):							
SiO2	71.99	73.79	71.72	73.74	75.27	65.62	75.22
Al2O3	14.74	14.30	14.94	14.61	14.25	16.85	14.50
TiO2	0.37	0.30	0.49	0.23	0.09	0.57	0.10
FeO*	2.00	1.82	2.38	1.33	0.82	3.92	0.93
MnO	0.03	0.04	0.03	0.03	0.02	0.08	0.02
CaO	1.91	1.58	2.02	1.45	0.61	4.11	0.59
MgO	0.76	0.64	0.90	0.41	0.17	2.37	0.20
K2O	4.75	3.94	4.25	4.89	5.42	2.68	4.80
Na2O	3.29	3.44	3.10	3.18	3.11	3.48	3.38
P2O5	0.16	0.14	0.17	0.12	0.24	0.32	0.24
Trace Elements (ppm):							
Ni	4	5	8	7	8	17	11
Cr	5	4	11	3	2	35	1
Sc	2	2	7	6	2	12	4
V	32	31	44	19	0	98	6
Ba	1420	781	979	615	159	1994	109
Rb	167	173	196	239	215	128	271
Sr	368	260	263	157	94	915	50
Zr	171	139	228	119	33	183	55
Y	13	23	17	15	11	15	17
Nb	15.9	17.8	14.1	17.3	15.5	11.3	19.4
Ga	17	21	21	21	19	22	22
Cu	4	0	6	2	10	20	7
Zn	34	42	58	42	74	72	55
Pb	20	20	19	24	34	19	20
La	57	39	70	41	7	67	0
Ce	122	83	126	69	31	104	25
Th	26	21	29	16	2	20	4

Major elements are normalized on a volatile-free basis.

*Total Fe is expressed as FeO

"†" denotes values >120% of our highest standard

Appendix C

Major and selected trace element X-Ray Fluorescence Data

Sample	LAD96-21	LAD96-22	LAD96-23	LAD96-25	LAD96-26	LAD96-27	LAD96-28
Rock Type	BtMsGr	BtMsGr	BtMsGr	BtMsGr	BtGr	BtMsGr	BtMsGr
Normalized Results (wt. %):							
SiO2	76.66	70.96	72.77	73.68	70.52	72.25	73.17
Al2O3	13.09	15.10	14.68	14.74	15.85	14.96	14.70
TiO2	0.13	0.51	0.40	0.23	0.32	0.33	0.28
FeO*	0.79	2.40	1.77	1.26	2.08	1.81	1.64
MnO	0.03	0.05	0.04	0.04	0.04	0.04	0.05
CaO	1.00	2.11	1.63	1.18	2.32	1.72	1.32
MgO	0.31	0.89	0.47	0.49	0.76	0.45	0.45
K2O	4.60	4.10	4.52	4.69	4.09	4.23	4.31
Na2O	3.29	3.64	3.58	3.57	3.86	4.06	3.95
P2O5	0.11	0.24	0.14	0.11	0.16	0.15	0.14
Trace Elements (ppm):							
Ni	10	6	7	6	8	6	7
Cr	2	6	3	5	8	3	2
Sc	0	0	0	2	4	5	0
V	13	48	34	14	36	31	28
Ba	475	1517	1467	982	1240	1621	1471
Rb	190	145	151	202	136	127	160
Sr	157	379	270	260	525	515	528
Zr	82	232	219	117	145	167	143
Y	14	18	17	18	14	18	21
Nb	14.9	21	15.1	21	17.3	17.4	22.3
Ga	17	19	19	18	20	21	18
Cu	4	3	4	2	3	37	6
Zn	20	51	48	38	50	61	39
Pb	25	19	19	25	34	41	39
La	19	73	43	35	43	45	64
Ce	52	131	99	65	81	77	89
Th	12	25	16	16	17	28	31

Major elements are normalized on a volatile-free basis.

*Total Fe is expressed as FeO

"†" denotes values >120% of our highest standard

Appendix C

Major and selected trace element X-Ray Fluorescence Data

Sample	LAD96-29A	LAD96-29C	LAD96-29E	LAD96-33	LAD96-35A	LAD96-36I
Rock Type	BtGd	BtMsGr	BtMsGr	BtMsGr	BtMsGr	BtMsGd
Normalized Results (wt. %):						
SiO2	68.02	71.88	71.58	74.50	71.82	73.27
Al2O3	16.43	15.01	15.42	14.46	15.11	13.70
TiO2	0.56	0.42	0.32	0.13	0.54	0.60
FeO*	3.11	2.33	1.89	0.93	1.95	3.43
MnO	0.06	0.03	0.03	0.02	0.02	0.03
CaO	3.35	2.16	2.39	0.82	2.05	1.73
MgO	1.42	0.55	0.67	0.08	0.56	1.46
K2O	3.01	3.81	3.92	5.40	4.54	3.34
Na2O	3.83	3.59	3.65	3.48	3.33	2.33
P2O5	0.23	0.21	0.13	0.18	0.09	0.11
Trace Elements (ppm):						
Ni	8	6	5	8	6	20
Cr	8	0	6	3	4	33
Sc	6	3	6	5	7	6
V	61	46	35	7	28	59
Ba	1129	1637	964	341	2210	735
Rb	113	105	107	223	143	131
Sr	668	599	524	114	313	221
Zr	189	189	126	60	215	176
Y	13	15	9	16	13	20
Nb	20.9	14	13.3	17.2	19.3	17.4
Ga	21	20	20	17	19	20
Cu	1	1	0	71	54	66
Zn	74	48	48	63	68	77
Pb	20	24	25	35	23	13
La	60	50	35	0	67	34
Ce	86	78	85	44	154	82
Th	19	14	15	4	42	14

Major elements are normalized on a volatile-free basis.

*Total Fe is expressed as FeO

"†" denotes values >120% of our highest standard

Appendix C

Major and selected trace element X-Ray Fluorescence Data

Sample	LAD96-37E	LAD96-37F	GA 77-99A	GA 88-43	GA 88-45	GAE 79-31	GAH 77-82C
Rock Type	BtGr	BtQS	BtQmd	BtMsGr	BtHblQmd	BtMsGr	BtGr
Normalized Results (wt. %):							
SiO2	73.76	62.53	66.56	75.70	65.69	73.22	68.38
Al2O3	14.15	18.02	16.83	14.33	16.50	14.62	15.67
TiO2	0.28	0.91	0.52	0.12	0.55	0.38	0.77
FeO*	1.03	3.97	2.90	0.82	3.83	1.76	3.42
MnO	0.02	0.11	0.06	0.02	0.09	0.03	0.03
CaO	0.67	2.58	3.37	0.89	4.14	1.54	2.36
MgO	0.34	1.78	1.61	0.22	1.72	0.63	1.06
K2O	6.63	5.59	3.09	4.55	3.44	4.52	4.00
Na2O	2.97	3.95	4.75	3.20	3.86	3.22	3.90
P2O5	0.15	0.54	0.35	0.14	0.18	0.11	0.40
Trace Elements (ppm):							
Ni	8	8	7	6	3	7	2
Cr	1	7	11	0	4	0	4
Sc	2	10	5	3	6	3	6
V	6	88	72	6	88	32	60
Ba	702	2851	1902	623	1355	977	1993
Rb	199	191	95	130	133	176	128
Sr	156	484	889	180	369	196	459
Zr	155	182	218	68	146	175	320
Y	18	44	7	15	17	18	18
Nb	21.6	33.1	10.6	14.5	12.8	16.6	12
Ga	17	22	19	20	17	20	22
Cu	41	57	0	2	0	2	0
Zn	38	101	67	25	44	26	73
Pb	43	19	20	29	9	18	17
La	69	36	84	7	40	36	77
Ce	145	92	43	0	35	66	105
Th	48	11	15	5	21	22	15

Major elements are normalized on a volatile-free basis.

*Total Fe is expressed as FeO

"†" denotes values >120% of our highest standard

Appendix C

Major and selected trace element X-Ray Fluorescence Data

Sample	GA 28/8/60-8	TO 66-78A	TO 66-138A	GAC 67-18	BU 65-67	BU 65-68
Rock Type	BtGr	BtMsGr	BtHblGd	BtMsGr	BtMsGr	BtMsGr
Normalized Results (wt. %):						
SiO2	71.58	73.64	69.63	76.30	71.57	75.66
Al2O3	15.50	14.43	15.46	14.19	15.10	14.41
TiO2	0.27	0.32	0.41	0.11	0.38	0.15
FeO*	1.58	1.60	2.70	0.93	2.10	0.59
MnO	0.05	0.02	0.05	0.01	0.04	0.02
CaO	2.01	1.35	2.87	0.53	1.65	0.78
MgO	0.74	0.56	1.41	0.26	0.64	0.16
K2O	3.93	4.87	2.96	4.69	4.47	5.43
Na2O	4.24	3.03	4.33	2.79	3.84	2.63
P2O5	0.11	0.17	0.18	0.18	0.23	0.17
Trace Elements (ppm):						
Ni	4	8	14	7	6	8
Cr	0	0	13	0	0	0
Sc	2	0	4	0	0	0
V	25	21	57	6	36	15
Ba	1758	680	1222	168	764	444
Rb	109	236	98	212	257	250
Sr	443	156	633	66	175	122
Zr	119	156	136	53	189	59
Y	12	17	14	19	23	16
Nb	14	18.8	14.2	21.7	23.1	23.8
Ga	17	19	18	21	22	22
Cu	3	9	6	4	2	11
Zn	41	44	33	16	55	18
Pb	16	24	13	23	16	19
La	0	16	8	0	31	0
Ce	1	59	20	4	57	8
Th	11	26	15	6	23	4

Major elements are normalized on a volatile-free basis.

*Total Fe is expressed as FeO

"†" denotes values >120% of our highest standard

Appendix C

Major and selected trace element X-Ray Fluorescence Data

Sample	BU 65-76	BU 65-77
Rock Type	BtMsGr	BtGd
Normalized Results (wt. %):		
SiO2	70.95	70.04
Al2O3	15.67	15.63
TiO2	0.28	0.38
FeO*	1.86	2.42
MnO	0.04	0.05
CaO	2.13	2.59
MgO	0.66	1.11
K2O	4.20	3.67
Na2O	4.07	3.96
P2O5	0.14	0.16
Trace Elements (ppm):		
Ni	2	4
Cr	2	16
Sc	7	9
V	39	65
Ba	933	1478
Rb	158	122
Sr	455	587
Zr	121	153
Y	15	13
Nb	17.4	15.1
Ga	20	21
Cu	6	2
Zn	42	51
Pb	36	31
La	3	6
Ce	30	51
Th	19	19

Major elements are normalized on a volatile-free basis.
*Total Fe is expressed as FeO
"†" denotes values >120% of our highest standard

Appendix D

Inductively Coupled Plasma-Mass Spectrometer Data

Sample	Rock Type	La	Ce	Pr	Nd	Sm	Eu	Gd	Tb	Dy
LAD96-2A	BtHblQmd	92.22	152.17	15.78	59.94	10.10	2.46	7.36	1.01	5.52
LAD96-2B	BtMsGr	19.78	34.88	3.56	12.63	2.79	0.54	2.60	0.44	2.47
LAD96-3	BtMsGr	63.06	103.32	9.86	34.39	5.50	1.11	3.90	0.56	2.98
LAD96-6	BtGr	83.93	118.92	12.56	43.82	7.32	1.46	5.35	0.78	4.44
LAD96-7	BtMsGr	35.31	61.82	6.36	23.59	4.46	0.81	3.24	0.44	2.06
LAD96-8	BtHblGd	26.27	44.20	4.65	17.53	3.18	0.95	3.05	0.47	2.72
LAD96-10	BtGr	31.03	51.27	5.10	18.37	3.20	0.87	2.91	0.45	2.59
LAD96-11	BtHblGd	61.05	89.29	9.49	32.74	5.12	1.20	3.72	0.49	2.67
LAD96-12	BtHblGd	52.00	87.62	8.90	32.40	5.49	1.30	4.27	0.60	3.29
LAD96-13	BtMsGr	47.78	85.99	8.88	32.79	6.36	1.01	4.25	0.57	2.95
LAD96-16	BtMsGr	46.11	79.78	8.13	28.82	5.77	0.83	4.31	0.67	3.88
LAD96-19A	BtMsGr	6.29	12.26	1.37	5.29	1.77	0.29	1.95	0.37	1.90
LAD96-19B	BtHblGd	72.65	120.86	12.27	43.87	6.95	1.57	4.51	0.57	2.97
LAD96-21	BtMsGr	24.25	41.26	4.23	14.97	2.98	0.57	2.32	0.36	1.97
LAD96-22	BtMsGr	70.68	118.06	11.81	42.09	7.37	1.40	5.30	0.69	3.79
LAD96-27	BtMsGr	54.10	91.86	9.40	34.21	6.77	1.43	4.97	0.67	3.45
LAD96-29C	BtMsGr	46.80	77.79	7.72	27.41	5.22	1.15	4.09	0.56	2.96
LAD96-35A	BtMsGr	92.08	163.49	16.82	61.49	10.99	1.54	6.45	0.69	2.88
LAD96-36I	BtMsGd	38.22	71.10	7.47	29.02	6.04	1.24	5.14	0.83	4.55
LAD96-37E	BtGr	69.91	132.38	14.19	50.51	9.91	0.81	6.13	0.75	3.41
LAD96-37F	BtQs	43.03	87.02	9.97	40.53	9.01	1.71	7.57	1.26	7.69
GA 77-99A	BtQmd	116.11	176.53	16.49	51.39	6.46	1.61	3.60	0.41	2.16
GA 88-43	BtMsGr	16.65	31.35	3.32	12.06	2.99	0.56	2.76	0.46	2.67
GA 88-45	BtHblQmd	36.30	61.81	6.03	21.19	4.12	0.99	3.58	0.53	3.12
GAE 79-31	BtMsGr	48.05	87.70	9.10	33.41	6.57	0.93	4.53	0.61	3.23
GAH 77-82c	BtGr	70.24	116.06	11.34	39.16	6.48	1.29	4.50	0.59	3.13
GA 28-8-60-8	BtGr	29.05	49.80	4.96	17.99	3.37	0.76	2.81	0.43	2.37
TO 66-78A	BtMsGr	47.43	91.09	9.85	36.37	7.31	0.78	4.75	0.63	3.26
TO 66-138A	BtHblGd	24.58	42.41	5.01	19.85	4.27	1.06	3.38	0.51	2.77
GAC 67-18	BtMsGr	13.98	27.64	3.04	11.21	3.22	0.40	3.31	0.65	3.72
BU 65-67	BtMsGr	53.37	97.95	10.34	37.06	7.07	1.00	4.92	0.72	3.88
BU 65-68	BtMsGr	16.04	29.06	3.10	11.37	2.48	0.59	2.02	0.32	1.86
BU 65-76	BtMsGr	36.68	63.28	6.51	23.97	4.68	1.03	3.34	0.47	2.39
BU 65-77	BtGd	40.80	71.27	6.99	24.84	4.32	1.14	2.87	0.38	1.96

Trace elements reported in (ppm)

Appendix D

Inductively Coupled Plasma-Mass Spectrometer Data

Sample	Rock Type	Ho	Er	Tm	Yb	Lu	Ba	Th	Nb	Y
LAD96-2A	BtHblQmd	1.06	2.62	0.36	2.20	0.35	1660.98	13.78	23.42	27.77
LAD96-2B	BtMsGr	0.44	1.08	0.15	0.85	0.13	678.48	8.62	6.42	12.96
LAD96-3	BtMsGr	0.57	1.50	0.22	1.35	0.22	1196.94	27.72	19.44	16.50
LAD96-6	BtGr	0.81	1.94	0.26	1.63	0.26	1490.03	18.14	23.28	22.00
LAD96-7	BtMsGr	0.34	0.76	0.11	0.64	0.10	994.79	12.45	12.42	9.73
LAD96-8	BtHblGd	0.52	1.39	0.22	1.42	0.23	1583.26	6.11	17.71	15.48
LAD96-10	BtGr	0.48	1.18	0.16	0.94	0.15	1830.09	8.18	11.24	13.22
LAD96-11	BtHblGd	0.50	1.26	0.18	1.11	0.17	1362.06	16.27	12.65	13.62
LAD96-12	BtHblGd	0.61	1.61	0.22	1.36	0.22	1715.77	13.96	13.86	16.75
LAD96-13	BtMsGr	0.53	1.36	0.20	1.20	0.18	915.68	17.65	17.17	15.00
LAD96-16	BtMsGr	0.75	2.05	0.31	1.94	0.30	779.94	18.51	18.02	22.62
LAD96-19A	BtMsGr	0.26	0.50	0.05	0.28	0.04	181.91	2.05	14.28	7.88
LAD96-19B	BtHblGd	0.51	1.26	0.18	1.03	0.17	1925.40	16.67	10.78	14.61
LAD96-21	BtMsGr	0.37	0.95	0.15	0.99	0.15	493.48	11.01	13.22	10.98
LAD96-22	BtMsGr	0.66	1.63	0.21	1.24	0.20	1473.28	20.08	19.79	18.38
LAD96-27	BtMsGr	0.59	1.41	0.18	1.01	0.17	1627.55	13.46	12.23	15.99
LAD96-29C	BtMsGr	0.55	1.48	0.22	1.37	0.23	1501.98	24.78	15.77	15.99
LAD96-35A	BtMsGr	0.44	0.97	0.13	0.79	0.14	2051.82	36.55	17.32	11.55
LAD96-36I	BtMsGd	0.74	1.53	0.18	0.97	0.16	720.15	11.03	16.20	20.16
LAD96-37E	BtGr	0.52	1.18	0.16	0.97	0.15	677.00	37.03	19.73	14.98
LAD96-37F	BtQs	1.56	4.35	0.64	3.82	0.59	2704.82	9.52	31.23	43.57
GA 77-99A	BtQmd	0.39	0.97	0.15	0.94	0.17	1737.12	23.32	12.91	11.35
GA 88-43	BtMsGr	0.46	1.06	0.15	0.84	0.12	685.12	7.12	15.66	14.03
GA 88-45	BtHblQmd	0.61	1.66	0.24	1.62	0.27	1287.20	18.57	13.11	17.42
GAE 79-31	BtMsGr	0.56	1.40	0.20	1.20	0.19	983.21	20.02	16.74	16.03
GAH 77-82c	BtGr	0.55	1.49	0.22	1.18	0.20	1968.93	10.00	10.39	16.24
GA 28-8-60-8	BtGr	0.44	1.17	0.17	1.10	0.18	1623.72	8.62	13.90	12.94
TO 66-78A	BtMsGr	0.53	1.26	0.18	1.04	0.17	694.07	24.07	18.64	15.15
TO 66-138A	BtHblGd	0.51	1.25	0.19	1.14	0.17	1211.74	10.16	12.83	14.25
GAC 67-18	BtMsGr	0.64	1.57	0.22	1.28	0.18	236.13	6.72	20.58	19.16
BU 65-67	BtMsGr	0.70	1.63	0.23	1.30	0.19	775.47	19.78	22.91	19.70
BU 65-68	BtMsGr	0.34	0.89	0.14	0.87	0.13	560.11	6.14	20.81	10.48
BU 65-76	BtMsGr	0.40	0.95	0.14	0.84	0.12	1187.11	16.97	15.49	12.04
BU 65-77	BtGd	0.34	0.87	0.13	0.78	0.12	1517.37	13.06	12.48	10.24

Trace elements reported in (ppm)

Appendix D

Inductively Coupled Plasma-Mass Spectrometer Data

Sample	Rock Type	Hf	Ta	U	Pb	Rb	Cs	Sr	Sc
LAD96-2A	BtHblQmd	5.79	2.85	2.67	11.00	99.53	4.22	1048.57	15.22
LAD96-2B	BtMsGr	2.43	2.55	2.25	29.11	126.63	2.03	260.06	1.68
LAD96-3	BtMsGr	4.23	3.40	2.41	23.13	160.68	4.27	492.41	4.61
LAD96-6	BtGr	4.12	3.09	2.04	15.78	124.11	3.58	606.07	9.37
LAD96-7	BtMsGr	3.38	3.27	2.37	24.72	162.65	5.36	331.82	3.01
LAD96-8	BtHblGd	3.58	3.83	1.70	17.10	119.35	5.06	597.84	6.05
LAD96-10	BtGr	3.88	2.55	2.80	25.22	130.42	3.15	521.11	4.22
LAD96-11	BtHblGd	3.76	2.89	2.25	19.93	86.39	1.78	623.00	5.78
LAD96-12	BtHblGd	4.84	2.49	2.58	21.83	88.73	2.49	618.59	7.76
LAD96-13	BtMsGr	4.22	2.97	2.48	22.86	201.54	3.40	281.79	4.98
LAD96-16	BtMsGr	4.04	3.68	4.41	23.19	173.40	5.19	262.55	4.69
LAD96-19A	BtMsGr	1.06	3.84	2.74	36.03	215.30	6.42	93.49	2.92
LAD96-19B	BtHblGd	4.24	2.32	2.49	21.35	127.44	10.23	903.05	10.71
LAD96-21	BtMsGr	2.41	4.08	2.49	25.49	184.52	4.46	162.63	2.78
LAD96-22	BtMsGr	5.99	2.99	3.04	21.31	146.05	4.52	396.38	6.42
LAD96-27	BtMsGr	4.89	2.39	2.04	26.75	103.34	1.77	601.52	5.33
LAD96-29C	BtMsGr	4.29	2.89	3.93	41.32	123.63	4.11	515.74	4.84
LAD96-35A	BtMsGr	5.63	2.84	2.77	25.38	139.24	2.01	308.31	4.67
LAD96-36I	BtMsGd	4.98	2.89	2.46	19.08	132.06	3.81	229.38	10.24
LAD96-37E	BtGr	4.43	3.14	5.22	43.03	185.04	3.51	152.43	3.10
LAD96-37F	BtQs	4.37	2.99	5.69	25.04	192.01	8.78	486.57	12.18
GA 77-99A	BtQmd	5.63	0.40	2.70	21.12	106.23	2.71	835.40	3.63
GA 88-43	BtMsGr	2.18	1.23	3.62	32.07	144.28	3.28	205.45	4.26
GA 88-45	BtHblQmd	4.50	1.40	3.71	13.67	130.60	2.71	372.85	10.58
GAE 79-31	BtMsGr	4.89	3.59	3.04	18.89	173.96	2.67	206.61	5.13
GAH 77-82c	BtGr	7.12	0.71	2.61	20.67	126.82	2.96	474.27	5.48
GA 28-8-60-8	BtGr	3.40	1.37	1.44	17.22	105.40	3.66	447.03	5.05
TO 66-78A	BtMsGr	4.70	1.59	2.90	24.32	238.48	5.55	163.51	3.97
TO 66-138A	BtHblGd	3.57	1.20	4.82	16.49	100.37	5.32	641.91	7.45
GAC 67-18	BtMsGr	2.03	2.78	3.44	24.53	214.65	6.67	77.02	3.41
BU 65-67	BtMsGr	5.38	4.90	5.16	19.16	250.02	18.60	183.19	5.03
BU 65-68	BtMsGr	1.75	4.23	6.71	21.51	264.95	11.66	136.91	5.14
BU 65-76	BtMsGr	3.23	1.56	2.48	33.04	163.15	7.77	484.57	4.41
BU 65-77	BtGd	3.66	0.96	2.81	34.64	114.12	3.64	626.48	5.26

Trace elements reported in (ppm)

IMAGE EVALUATION
TEST TARGET (QA-3)

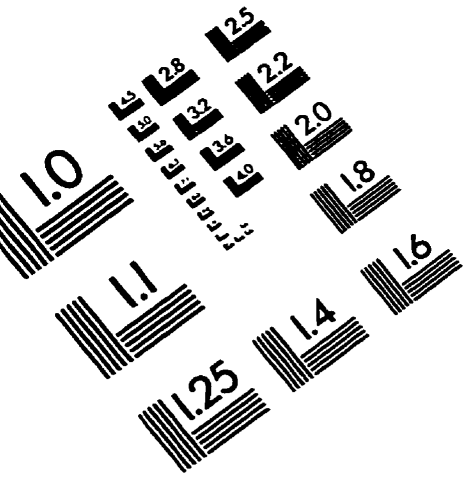

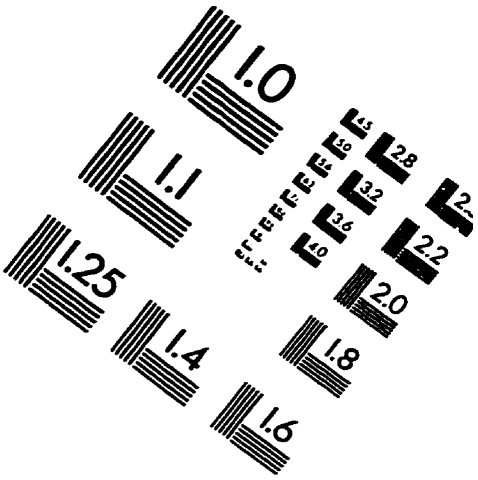

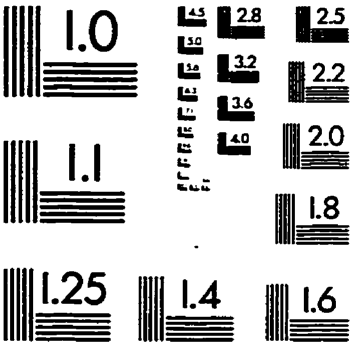

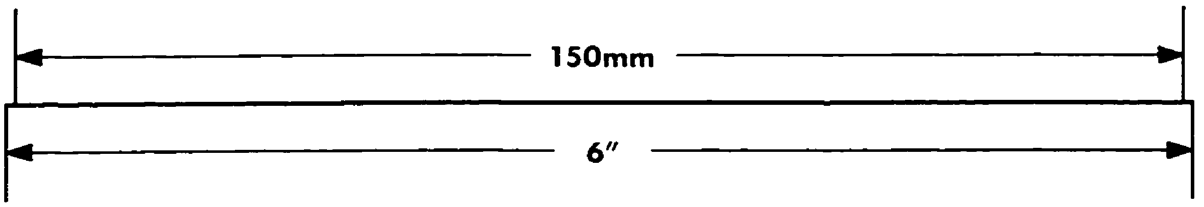

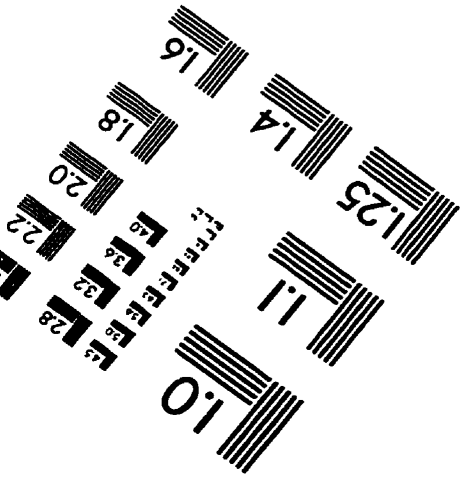

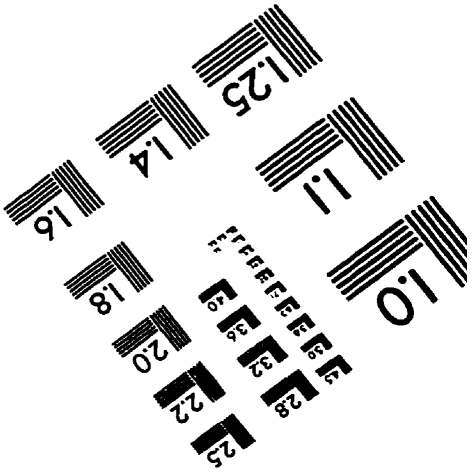

APPLIED IMAGE, Inc
1653 East Main Street
Rochester, NY 14609 USA
Phone: 716/482-0300
Fax: 716/288-5989